UNIVERSITY OF BELGRADE

SCHOOL OF ELECTRICAL ENGINEERING

Uroš Ralević

Nanoscopy and applications of two-dimensional and quasi-two-dimensional systems

doctoral dissertation

Belgrade, 2017

UNIVERZITET U BEOGRADU

ELEKTROTEHNIČKI FAKULTET

Uroš Ralević

Nanoskopija i primene dvodimenzionalnih i kvazi dvodimenzionalnih sistema

doktorska disertacija

Beograd, 2017

Thesis advisor, Committee member:
Dr. Jelena Radovanović
Professor
School of Electrical Engineering
University of Belgrade

Committee member:
Dr. Vitomir Milanović
Professor Emeritus
School of Electrical Engineering
University of Belgrade

Committee member:
Dr. Goran Isić
Assistant Research Professor
Institute of Physics
University of Belgrade

Committee member:
Dr. Milan Tadić
Professor
School of Electrical Engineering
University of Belgrade

Committee member:
Dr. Milka Potrebić
Associate Professor
School of Electrical Engineering
University of Belgrade

Acknowledgements

This thesis was done in the Center for Solid State Physics and New Materials (CSSPNM), Institute of Physics Belgrade, under the supervision of Dr Goran Isić. The completion of this thesis would not be possible without his support, guidance and help. I am grateful to Goran for teaching me a good scientific practice and for giving me a chance to participate in a number of interesting scientific projects.

I would like to thank Prof. Dr Rados Gajić for accepting me in his group and for giving me the opportunity to work within the OI 171005 project.

I am very grateful to Prof. Dr Zoran Popović for giving me the opportunity to work in the CSSPNM and for including me in the project dealing with charge density waves. I would like to thank Prof. Dr Popović for useful discussions about charge density waves physics and for invaluable help in completing the charge density waves manuscript.

I would like to express my gratitude to Dr Borislav Vasić for teaching me how to use the ambient scanning probe microscope and for general help and useful advices regarding projects related to graphene and scanning probe microscopy.

I am very grateful to Dr Nenad Lazarević for useful discussions about charge density waves physics and for invaluable help in completing the charge density waves manuscript.

I would like to thank to Prof. Dr Čedomir Petrović and Prof. Dr Ian. R. Fisher for fabricating high-quality cerium tritelluride samples.

I would like to thank to Prof. Dr Rudi Hackl, Andreas Baum and Dr Hans-Martin Eiter for performing Raman measurements of cerium tritelluride and for analysing the results. Specially, I am very grateful to Prof. Dr Rudi Hackl for useful discussions about charge density waves physics and for invaluable help in completing the charge density waves manuscript.

I would like to thank Dr Marko Radović for teaching me how to operate the UHV scanning probe microscope.

I am grateful to my CSSPNM colleagues Dr Aleksandar Matković, Dr Milka Jakovljević, Jelena Pesić, Angela Beltaos, Marijana Milićević, Milenko Musić, Dr Ivana Milošević, Dr Radmila Panajotović, Dr Marko Spasenović, Dr Igor Popov, Tijana Tomašević-Ilić, Jasna Vujin, Dr Sonja Aškarabić, Dr Novica Paunović, Bojan Stojadinović, Natasa Tomić and Marko Opačić for more than pleasant working atmosphere, help in the lab and more than useful collaborations.

I would like to thank Bojana Laban, Una Bogdanović, Dr Vesna Vodnik and Dr Vesna Vasić from the Vinca Institute Belgrade for synthesizing colloidal nanoparti-

cles and for fruitful discussions about dye-nanoparticle systems.

I would like to thank Dr Roman Gorbachev from the University of Manchester for fabrication of isolated graphene samples.

I am grateful to Vladimir Lazović for scanning electron microscopy images of colloidal nanoparticles.

In the end, I would like to thank my mother Snežana, father Miomir, brother Dušan and sister Bojana for always being there for me.

I would like to acknowledge financial support by the Serbian Ministry of Education, Science and Technological Development through Project OI 171005.

Abstract

This thesis addresses some of the fundamental and technological aspects of two- or quasi-two-dimensional systems realised within novel materials or metallic nanoparticle clusters. In particular, charge density modulations of the quasi-two-dimensional electron system in $CeTe_3$, the two-dimensional electron system in graphene, two-dimensional excitons in MoS_2, and surface plasmons in metallic nanoparticle clusters were probed by a number of scanning probe microscopy and optical spectroscopy techniques. The optical properties, spectroscopic data and some potential applications of two-dimensional systems were investigated by numerically solving the macroscopic Maxwell equations by the finite element or reflection pole methods.

The charge density waves in $CeTe_3$ were investigated at room temperature by scanning tunneling microscopy, scanning tunneling spectroscopy and Raman spectroscopy. The modulation wavevector and the induced energy gap, which are crucial for describing these excitations, were assessed. The mixing of the modulation's wavevector with the wavevectors of the underlaying lattice was also observed. The charge density modulation was found to be followed by periodic rearrangement of tellurium atoms in planar layers hosting the modulation.

The influence of the environment on the two-dimensional charge carriers in graphene was investigated by Kelvin probe force microcopy and electrostatic force microscopy. This study was done for bare and isolated electrically gated graphene samples in which the concentration of charge carriers can be tuned via the electric field effect. The results of this study, based on the analysis of the measured contact potential difference, showed that the environment induces instabilities in doping levels of graphene even upon application of the gate voltage. The stability of gate-induced changes of the doping level in graphene is crucial for graphene based devices. Therefore this result indicates that improved performance of graphene based devices can be expected if graphene is isolated from the environment.

Interaction between graphene and guided modes of optical waveguides was studied by means of exact numerical simulations and a convenient perturbation theory. The conclusion reached in this study is that graphene modifies the modal propagation constants and that this effect can be used in construction of graphene based optical modulators.

Investigation of the influence of metallic nanoparticle clusters on two- dimensional excitons in MoS_2 has showed that these nanoobjects do not alter the spectral position or width of the exciton photoluminescence but rather induce a small enhancement of the A excitonic peak. The reason for the weak interaction was found

in the misalignment of the MoS_2 plane and the dominant cluster's electric field component, as well as in the fact that the electric fields are weak near the MoS_2 plane. The electric fields were found to be the strongest within nano-gaps between the adjacent nanoparticles. This was utilized for the surface enhanced Raman spectroscopy study of the adsorption of thin aggregated dye layers on the cluster surface.

Keywords: two-dimensional system, quasi-two-dimensional system, cerium tritelluride, graphene, molybdenum disulfide, scanning probe microscopy, Raman spectroscopy, surface enhanced Raman spectroscopy

Scientific field: Electrical and Computer Engineering

Research area: Nanoelectronics and Photonics

UDC number: 621.3

Rezime

U ovoj tezi razmatrani su neki od fundamentalnih i tehnoloških aspekata dvodimenzionalnih ili kvazi dvodimenzionalnih sistema, koji su realizovani u novim materijalima ili klasterima metalnih nanočestica. Tehnikama skenirajuće mikroskopije i optičke spektroskopije proučavani su modulacija gustine naelektrisanja u kvazi dvodimenzionalnom elektronskom sistemu u $CeTe_3$, dvodimenzionalni elektronski sistem u grafenu, dvodimenzionalni ekscitoni u MoS_2 i površinski plazmoni u klasterima metalnih nanočestica. Optičke osobine, spektroskopski podaci i potencijalne primene dvodimenzionalnih sistema proučavani su numeričkim rešavanjem makroskopskih Maksvelovih jednačina pomoću metoda refleksije polova i konačnih elemenata.

Pomoću skenirajuće mikroskopije, skenirajuće spektroskopije i Ramanove spektroskopije proučavan je talas gustine naelektrisanja u $CeTe_3$ na sobnoj temperaturi. Kao rezultat ove studije određeni su talasni vektor modulacije elektronske gustine stanja i energetski procep kojima se talas gustine naelektrisanja može opisati. Uočena je i pojava mešanja talasnog vektora modulacije sa talasnim vektorima atomske rešetke u ravni u kojoj se formira talas gustine naelektrisanja. Utvrđeno je da modulacija elektronske gustine stanja postoji zajedno sa periodičnom modulacijom atomske rešetke telurovih atoma u kojima se talas gustine naelektrisanja formira.

Uticaj faktora iz spoljašnje sredine na dvodimenzionalne nosioce naelektrisanja u grafenu proučavan je pomoću skenirajuće Kelvinove mikroskopije i mikroskopije elektrostatičkih sila. Ova studija je realizovana u slučajevima kada je grafen izložen odnosno izolovan od uticaja iz okolne sredine. Proučavani su uzorci pripremljeni u takozvanoj gejt konfiguraciji koja omogućava promenu koncentarcije nosilaca u grafenu primenom napona gejta. Na osnovu analize izmerene kontaktne potencijalne razlike nađeno je da faktori iz spoljašnje sredine dovode do nestabilnosti koncentracije elektrona u grafenu, čak i kada je napon gejta primenjen. Pošto je stabilnost nivoa dopiranja neophodna za rad naprava na bazi grafena, ova studija pokazuje da se bolje performanse mogu očekivati kada je grafen izolovan od uticaja iz spoljašnje sredine.

Razmatrana je i interakcija grafena sa vođenim modovima optičkih talasovoda. Za analizu ovog problema upotrebljeni su različiti numerički alati. Zaključeno je da grafen dovodi do modifikacije propagacione konstante vođenih modova i da se ova pojava može iskoristiti u konstrukciji optičkih modulatora.

Ispitivanjem uticaja klastera metalnih nanočestica na fotoluminescenciju ekscitona u MoS_2 nađeno je da metalni nanosistemi ne utiču na poziciju i spektralnu

širinu fotoluminescencije, ali da ipak dovode do slabog pojačanja ekscitonskog A pika. Razlozi su slabo sprezanje električnog polja metalnih klastera i MoS_2 kao i slab intenzitet ovih polja u blizini MoS_2. Cinjenica da je električno polje u okviru metalnih klastera jako u šupljinama između nanočestica iskorišćena je za proučavanje mehanizma adsorpcije tankih slojeva organske boje na površinu klastera, pomoću površinom podstaknute Ramanove spektroskopije.

Ključne reči: dvodimenzionalni sistem, kvazi dvodimenzionalni sistem, cerijum tritelurid, grafen, molibden disulfid, mikroskopija skenirajućom probom, Ramanova spektroskopija, površinom podstakunta Ramanova spektroskopija

Naučna oblast: Elektrotehnika i računarstvo

Oblast istraživanja: Nanoelektronika i fotonika

UDK broj: 621.3

Contents

Chapter 1 Introduction

1.1 Introduction to low-dimensional systems

Low-dimensional systems are amongst the most interesting topics in solid state physics, or rather in physics in general. Talking about low-dimensional systems seems very abstract given that all physical objects and systems we encounter in the real world possess a full set of three spatial dimensions. The concept of a low-dimensional system is, however, different than the one in which a system simply lacks one or more spatial dimensions. In physics the dimensionality of a system is determined by the number of spatial dimensions in which the free motion of its microscopic degrees-of-freedom is allowed. For example, in one-dimensional electron system the free motion of electrons is allowed in one spatial dimension and forbidden in the other two.

What are the consequences of reduced dimensionality? In order to answer this question we shall start by considering an electron in a box, which is able to move freely within the box volume. Within the framework of quantum mechanics the electron is described by its wave function and kinetic energy. The electron is not allowed to leave the box and therefore its wave functions must be zero at the box boundaries. The kinetic energy of such a system is continuous and can be assessed form the single particle Schrodinger equation

$$E = \hbar^2 \mathbf{k}^2/(2m), \tag{1.1}$$

where $\hbar$ is the reduced Plank's constant, $\mathbf{k} = (k_x, k_y, k_z)$ and m are the wave vector and the mass of the electron, respectively. The concept of reduced dimensionality carries with it a picture in which some of the physical lengths of a system are very small. So let us start flattening out the box, say in the x direction. The reduction of the box size in x would gradually confine the movement of the electron until the size of the box in this direction becomes smaller than the de Broglie wavelength of the electron (in this case the wavelength of its thermal motion), i.e. $L_x < 2\pi/k_x$. At this point the motion of the electron in x freezes and the k_x component of the wave vector, as well as the kinetic energy of the system, becomes discrete and quantized.

The total energy of the system is now given by

$$E = \hbar/(2m) \times (n_x \pi / L_x)^2 + \hbar^2 \mathbf{k}_{||}^2/(2m), \tag{1.2}$$

where $\hbar/(2m) \times (n_x \pi / L_x)^2$ represents the quantized energy in the x direction and $\mathbf{k}_{||} = (k_y, k_z)$ represents the continuous wave vector characterising free motion of the electron in yz plane. $n_x = 1, 2, ...$ The first obvious consequence of the reduced dimensionality is therefore the quantization of energy in the direction of the confinement. The illustration in figure 1.1(a) shows decreet energies of our system within the confines of the flattened box, i.e. an infinite quantum well. If the same procedure is repeated in y the energy would become quantized in this direction as well. Now we would have a situation in which the electron is able to move only in z direction as quantified by continuous wave number k_z.

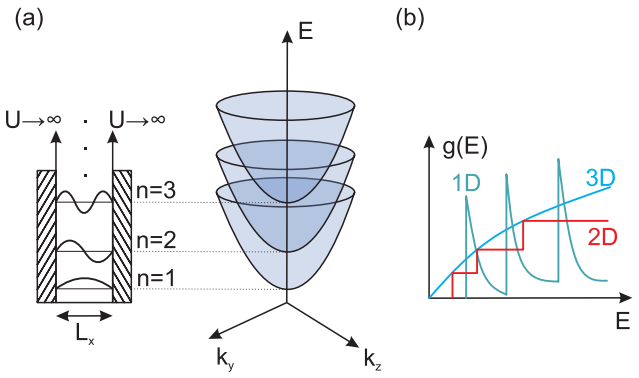

Figure 1.1: (a) Left side of this panes shows quantum well with infinite walls. First three quantized energy levels are shown by horizontal lines. Complete energy dispersion including continuous components of the wave vectors is shown. The paraboloids are also called subbands. (b) Density of states for one-, two- and three-dimensional electron gases.

Another important consequence is the modification of the density of states, $g(E)$. In case of the three dimensional ideal electron system the density of states has a square root dependance on the energy, $g(E) \sim E^{1/2}$, whereas the energy dependance is completely lost in two-dimensional system, $g(E) \sim E^0$, and strongly modified in one-dimensional system, $g(E) \sim E^{-1/2}$ [see figure 1.1(b)].

What makes low-dimensional systems so interesting? The notion of reduced dimensionality comes with a plethora of interesting effects, such as the quantum Hall effect, which are nonexisting in traditional three-dimensional systems. These effects, governed by the laws of quantum mechanics, offer an unprecedented insight in the microscopic world around us and are, as such, of fundamental interest. The extensive research of low-dimensional systems, which started in the first half of the 20th century, contributed to the birth of scientific disciplines such as nanotechnology, sur-

face science, thin film physics and plasmonics. On the other hand, throughout the history, low-dimensional systems (such as the two-dimensional electron gas realised in metal-oxide-semiconductor structures) have proven to be of the utmost importance in majority of applications including electronics and modern communications, to name a few.

A number of Nobel prises awarded for significant scientific and technological breakthroughes in the fields of physics and chemistry are related to the studies of low-dimensional systems. For instance, the Nobel prise in physics for the discovery of quantum Hall effect in two-dimensional electron systems was awarded to Klitzing in 1985. In 1996, Smalley was awarded Nobel prise in chemistry for the discovery of Fullerene, an essentially zero-dimensional system. Two years later, in 1998, Stormer, Tsui and Laughlin shared the Nobel prise in physics for the discovery of the integer quantum Hall effect. Finally, in 2010, Geim and Novoselov were awarded the Nobel prise in physics for the discovery of graphene, a monolayer of hexagonally arranged carbon atoms and a playground hosting various two-dimensional systems.

Even after decades of research, scientists still find interesting and novel phenomena in low-dimensional systems, realised nowadays in novel classes of materials, which hold promise not just for improving current state of technology but also for rising it to another level.

1.2 Two-dimensional and quasi-two-dimensional systems

Systems in which the free motion of the microscopic degrees-of-freedom is quantized in one spatial dimension and allowed in the other two are called two-dimensional systems. Two-dimensional systems are a part of the three dimensional world as they are realised within physical structures possessing three spatial dimensions. A perfect example would be a two-dimensional electron gas realised at the interface between two bulk crystals. As such, two-dimensional systems are always interconnected with their surroundings and able to interact with it. For instance, the properties of the aforementioned electron gas (such as the quantized energy and the level of confinement) are determined both by the properties of the two bulk crystals and by interactions with other systems hosted by these crystals (such as phonons). Fortunately, the properties of two-dimensional systems are often only slightly modified by interactions with other systems. Therefore, such interactions are either treated as a small perturbation to the closed two-dimensional system (having an initial set of defined properties), or completely neglected. In scanning tunneling microscopy, for example, a two-dimensional electron gas is forced to interact with a sharp probe standing in its close vicinity. Due to the quantum mechanical tunneling occurring between the two, the electrons can be added or taken from the electron gas thus

slightly perturbing its state. However, this perturbation is very small and often neglected as the density of electrons is maintained through interconnection with the physical structure hosting the electron gas.

A significant interaction between a two-dimensional system and the three-dimensional world in which it is embedded is often signaled by the quasi- prefix. The title of this thesis is thus chosen to comprise both the original and the term expanded by the quasi- prefix, reflecting the fact that it considers various two-dimensional systems exhibiting a range interaction mechanisms with the environment. However, since no strict boundary exists between what might be considered a real and a quasi-two-dimensional system, in the remainder of the thesis the prefix is left out entirely.

In what follows, we will introduce a few two-dimensional systems including two-dimensional electron systems and their two-dimensional excitations, surface states, and two-dimensional electron-hole coupled systems.

1.2.1 Two-dimensional electron systems

A textbook example of a two-dimensional electron systems is the two-dimensional electron gas. In practice, the two-dimensional electron gas is formed from the valence electrons of atoms arranged in a specific fashion. For example, due to the specific way in which atoms are arranged in a solid the energy of valence electrons, which are participating in formation of the bonds between the atoms, are rearranged into energy bands. The distribution of electrons within these bands is determined by the temperature and the Fermi level by a well known Fermi-Dirac distribution function. The highest fully occupied band is the valence band. The next energy band is the conduction band. When excited to the conduction band the electrons are able to roam around the crystal in the periodical background of the positive 'ions', thus forming the three dimensional electron gas. In solids the behaviour of the electron gas can be very complicated since it is governed by a lot of different factors. These factors are contained within the background potential provided by the crystal lattice, the nature of the chemical bonds within the crystal and various interactions, such as the electron-electron and electron-phonon interactions. Often all the important factors influencing the motion of an electron can be accounted for by replacing the electron mass m in equation 1.1 by an effective mass m_{eff} and adding an effective potential term. Now that we have a three dimensional electron gas all we need to do is confine the motion of electrons to a plane. This can be done by introducing a potential well similar to the one used for the description of the ideal two-dimensional gas. Again, by neglecting all the interactions within the effective mass approximation, the energy of such two-dimensional electron gas can be as-

sessed from equation 1.2. However, a more common case is quite the opposite since the quantum nature of various interactions becomes very strong in two-dimensions. To describe, let alone analyze these effects one needs a quite complex set of theoretical tools, far beyond the single particle Schrodinger equation in the effective mass approximation. Instead of solving complex equations we will rather introduce practical ways in which the two-dimensional electron gas can be realised.

Interfaces and surfaces The first realisation of the two-dimensional electron gas is tightly connected to metal-oxide-semiconductor (MOS) structures [1]. The main idea is to induce an 'inversion layer' at the interface between doped semiconductor and the oxide on top of it. This is achieved by applying an external electric field via the so-called gate voltage between the semiconductor and the metal, as illustrated in figure 1.2(a). If a p-type semiconductor is used, a positive gate voltage will bend the semiconductor's conduction band until it surpasses a threshold at which the conduction band close to the interface falls below the Fermi level. At that point a triangular potential well is formed for the electrons at the interface [see figure 1.2(a)]. This potential confines the electrons in the direction perpendicular to the interface and a two-dimensional gas is formed. From that point on, the gate voltage controls the concentration of the electrons within the potential well. The MOS structure is one of the most important technological breakthroughs of the 20th century. This particular structure is used for construction of the metal-oxide-semiconductor field effect transistors (MOSFET) which are the core of today's modern electronics. The Si/SiO_2 is the most studied and exploited semiconductor/oxide combination of materials.

The two-dimensional electron gas can be also formed at the interface semiconductor heterojunctions. Here the band bending, and formation of the confining potential well for the electrons at the interface is achieved when two semiconductors with different band gaps are brought in contact, as illustrated in figure 1.2(b).

The electrons can be trapped above the atoms of liquid helium residing on a substrate [2]. In this case, due to the fact that the conduction band is high above the vacuum level, the electrons can not penetrate the helium. On the other hand the image charges attract the electrons thus preventing them from leaving the surface region. This system is of a particular historical relevance since it is one of the first systems to be experimentally realised and certainly the first system in which collective oscillations of the two-dimensional electron gas, whose quanta are named two-dimensional plasmons, were observed [2].

Finally, we can conclude this part of the story by mentioning a new concept for realisation of two-dimensional electron gases which was introduced recently, in 2004. In this very counterintuitive concept, surfaces of insulators or interfaces of insulator

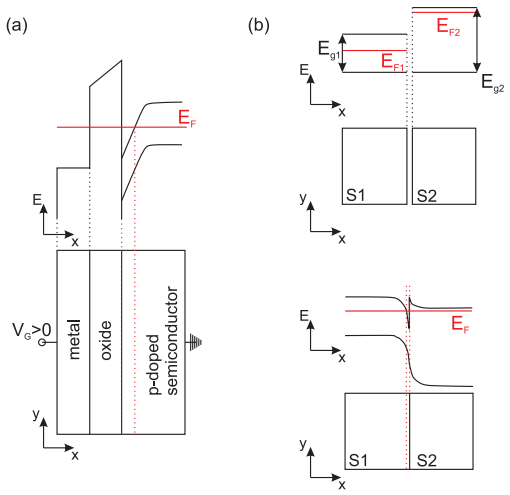

Figure 1.2: Illustration of principles in which the two-dimensional electron gas is formed in (a) MOS structure and (b) at the interface of semiconductor heterojunction. Upper part of panel (b) shows the the valence and conduction bands of the two semiconductors before contact, whereas lower panel illustrates what happens when the contact is made.

heterojunctions, such as $LaAlO_3$ and $SrTiO_3$, are the the places where the two-dimensional electron gases are formed. The exact mechanism and the underlying physical nature of the electronic structure of these peculiar systems is still an open question [3].

Thin films Unlike at surfaces and interfaces, the electron gas in thin films gains a two-dimensional character when the the Fermi wavelength of electrons becomes comparable or larger than the film's thickness. Semiconducting thin films are usually sandwiched between the other two semiconductors to form a quantum well for electrons. Materials such as InSb, PbTe and III-V compounds were extensively studied within the 1970s-1980s historical frame. Apart from semiconductors, thin films of semimetallic compounds, such as $Bi_8Te_7S_5$ which could be cleaved to the monolayer thickness (5 atoms thick), were also studied at that time [4]. The electrons in thin metallic films, on the other hand, do not usually behave two-dimensionally. In contrast to semiconductors in which electrons have a typical Fermi wavelength of the order of couple of nanometers, in metals this characteristic wavelength is of the order of the lattice constant. The thickness of a metal film cannot be reduced below a certain threshold without making the film discontinuous. However, when a thin continuous metal film is superconducting the electrons may behave two-dimensionally as long as the coherence length of the superconductivity is greater than the film's thickness [1].

Anisotropic layered materials So far we have introduced two essential ways in which one can trap electrons and make them behave two-dimensionally. There are, however, various bulk, three dimensional materials which are highly anisotropic for the electrons. In fact, due to the specific way in which the atomic orbitals are hybridized the band structure of these compounds can be virtually independent of the transverse momentum, so the electrons are confined to the layers and have a two-dimensional nature. These materials are often metallic compounds consisting of layers stacked together to form the bulk crystal. The anisotropy is seen through high values of conductivity parallel to the layers and very low values of conductivity in the perpendicular direction. Many of these particular compounds exhibit a number of interesting phenomena related to phase transitions such as superconductivity and charge density waves. The latter can, in some cases, lead to a transition from a metallic to a semiconducting state. $NbSe_2$, NbS_2, $TaSe_2$ and TaS_2 are the examples of the materials which were studied back in 1970s and 1980s, and which are still studied today. The other interesting metallic layered material is graphite. In 1980s, this material and it's intercalated variants were extensively studied, mainly within the scientific community dealing with superconductivity [1].

1.2.1.1 Two-dimensional surface states and surface excitations of the electron systems

We have seen that electrons can be confined to a surface of semiconductor by an external electric field or by discontinuities of the conduction and valence bands at the interface of two semiconductors. In contrast to these two-dimensional systems, the electrons near the surface of a solid (usually metals and semiconductors) can form to so-called surface states. Since the periodicity of the crystal is disrupted at the surface, the electrons may acquire a complex wave number in the direction normal to the surface. This implies that their wave function decays exponentially away from the surface into the crystal and the medium above it. These states, which are a legitimate solution of the Schrodinger's equation, are different from the bulk states which have periodic wave functions in the crystal and decay exponentially out of it [see figure 1.3]. Hence, surface states may be considered as two-dimensional electron systems as well. They were first introduced by Tamm in 1932, and studied by Shockley in late 1930s [5].

Even though electrons in bulk metals cannot acquire true two-dimensional nature, they can be excited to form yet another two-dimensional system. Nearly free electron gas in metals exhibits a particular kind of collective density oscillations known as plasma oscillations. The quantum of energy of these oscillations is given by $\hbar\omega_p = \hbar\sqrt{ne^2/(\epsilon_0 m)}$. ω_p, n and m represent the plasma frequency, electron density and electron mass, respectively. At the surface of a metal self-sustained collective

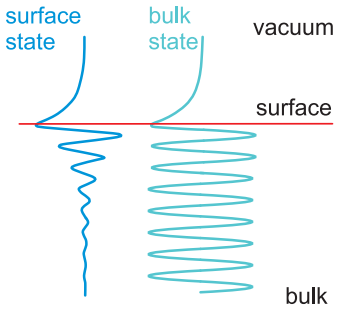

Figure 1.3: Illustration of Tamm's surface state. Bulk state is also shown for comparison.

density oscillations, i.e. surface plasma oscillations, can occur. This phenomenon was predicted in 1957 by Ritchie [6], who was studying characteristic energy losses of fast electrons passing through thin metal films. The surface plasma oscillations are accompanied by the electromagnetic filed which propagates along the surface of the metal and decays exponentially below and above the surface [see figure 1.4(a)].

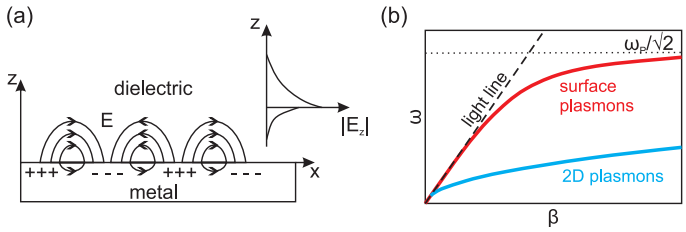

Figure 1.4: (a) Surface plasmons propagating at the metal/dielectric interface. (b) Comparison of dispersion relations belonging to surface plasmons and two-dimensional plasmons.

Similarly as in case of surface states, this means that the transversal wave vector component takes complex values. Hence, these excitations, often referred to as surface plasmons or surface plasmon polaritons, are confined to the surface of the metal. The in-plane wave vector component, often called the propagation constant, β, on the other hand, assumes real values. The frequency of the oscillations, ω, is connected to the propagation constant by the following dispersion relation

$$\beta = \frac{\omega}{c}\sqrt{\frac{\epsilon_{metal}}{1+\epsilon_{metal}}}, \tag{1.3}$$

where c is the speed of light and ϵ_{metal} is the dielectric constant of the metal. In equation 1.3 we have assumed that the media above the metal surface is vacuum with dielectric constant equal to 1. From this equation we see that surface plasmons can propagate along the surface with a broad spectrum of frequencies from 0 to $\omega_p/\sqrt{2}$, while their dispersion relation lies below the dispersion line of the light in vacuum, ω/c [see figure 1.4(b)]. Consequently, they are often labeled as nonradiative surface

plasmons describing the fluctuation of the surface charge density. In the low β limit the dispersion is very close to the light line meaning that the field of the surface plasmon is poorly confined to the metal surface, whereas it is quite the opposite in the high β limit. In fact, in the latter limit the surface plasmons resemble localized fluctuations of the electron plasma.

Surface plasmons should not be mistaken for two-dimensional plasmons. Two-dimensional plasmons are quanta of collective density oscillations of the two-dimensional electron gas, having a dispersion which obeys $\omega \sim \sqrt{\beta}$ [see figure 1.4(b)]. Plasmons in a two-dimensional electron gas were first experimentally observed by Grimes and Adams in 1976 for electrons in liquid helium [2].

Interfaces of arbitrary finite metallic objects can also support charge density oscillations similar to the described surface plasmons. These are called localized surface plasmons, or Mie plasmons. The frequencies at which localized surface plasmons occur strongly depend on the interface geometry. Localised surface plasmons excited on the surface of small metallic particles, or rather their clusters, are extremely important in various sensing applications and particulary in surface enhanced Raman spectroscopy.

1.2.1.2 Charge density modulation in two-dimensional electron systems

While most of two-dimensional electron systems represent a perfect platform for exploration of the many-body effects, some of them are simply unprecedented in the richness of various physical effects they have to offer. The examples of such systems are those exhibiting the so-called charge density waves. The first to experimentally observe charge density waves was Monceau in 1976 [7] while studying the $NbSe_3$ crystals.

According to the simplest available definition, charge density waves are periodic modulations of the electron density in real space. The basic concept of charge density waves can be explained by considering a one-dimensional electron gas realized in linear chain of atoms with a lattice constant a at $T = 0$ K [see figure 1.5(a)]. The one-dimensional model is used instead of the two-dimensional one in order to avoid unnecessary complications in an already complex concept. The two-dimensional case will be discussed after the introduction of the charge density waves basics.

We shall start by assuming that the electrons fill a portion of the conduction band, as illustrated in figure 1.5(a) and quantified by the Fermi level $E_F = \hbar^2 k_F^2 / 2m_{eff}$, where $k_F = \pi/2a$ is the Fermi wave vector.

Now let us induce a small perturbation by slightly displacing the atoms in the chain from their initial positions. From the perspective of the one-dimensional electron gas this perturbation is given in the form of a periodic potential $\phi(q) = \Delta e^{iqx}$, where q is the wave vector and Δ is displacement amplitude.

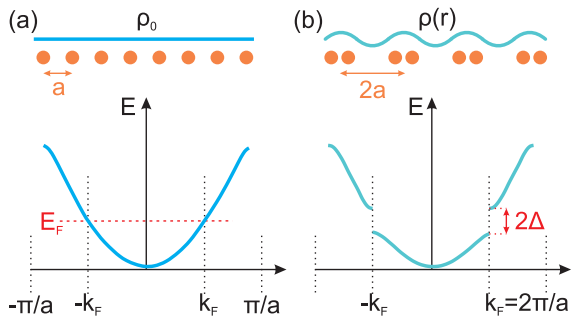

Figure 1.5: (a) Ground state in the absence of perturbation. (b) New ground state characterised formed in response to the perturbation.

The response of the ideal electron gas at $T = 0$ K to the small, static periodic perturbation is given within the linear response theory, by the Lindhard response function

$$\chi(\mathbf{q}) = \int \frac{d\mathbf{k}}{(2\pi)^d} \frac{f(E_\mathbf{k}) - f(E_{\mathbf{k}+\mathbf{q}})}{E_\mathbf{k} - E_{\mathbf{k}+\mathbf{q}}}, \tag{1.4}$$

where $f(E)$ is the Fermi-Dirac distribution function, $E(\mathbf{k})$ is the dispersion relation of the electron gas, and $d = 1, 2, 3$ depending on the dimensionality of the electron gas. The change of the electronic charge density induced by this perturbation is related to the response function as

$$\Delta\rho = -\chi(q)\phi(q). \tag{1.5}$$

The response function of the one-dimensional electron gas is shown in figure 1.6. When the wave vector of the perturbation is twice the Fermi wave vector, k_F, this function diverges.

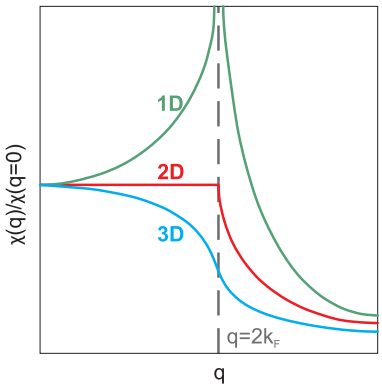

Figure 1.6: Lindhard response function versus perturbation wave vector q, at T=0 K for one-, two- and three-dimensional electron gas Adopted from Ref. [8].

From equation 1.4 it follows that the states with the same energy and with Fermi wave vectors of opposite signs are responsible for the behaviour of the Lindhard function around $q = 2k_F$. Meanwhile, all states having energy equal to E_F are represented by the Fermi surface in the reciprocal space. In case of one-dimensional electron gas the Fermi surface is represented by points $\pm k_F$ [see figure 1.7]. Obviously, in one-dimensional gas all states with $-k_F$ can be mapped into corresponding k_F states by a single wave vector $Q = 2k_F$, thus leading to the divergent behaviour of the Lindhard function. The mapping of $-k_F$ and k_F states onto each other by Q is often called the nesting of the Fermi surface and Q is consequently labeled as the nesting vector. In the case of two- and three-dimensional electron gases the number of such states is significantly reduced due to the topology of their Fermi surfaces [see figure 1.7]. Consequently, their Lindhard functions have finite values at $q = 2k_F$ [see figure 1.6].

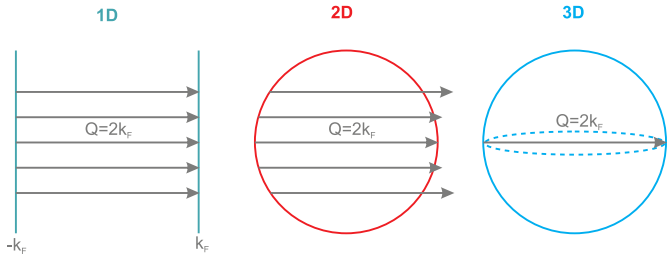

Figure 1.7: Fermi surfaces of one-, two- and three-dimensional electron gas. Nesting vector Q is shown by arrows. In one-dimensional case the nesting is perfect.

The divergence of the Lindhard's response at $q = 2k_F$ means that the one-dimensional electron system gains a huge amount of energy by modifying its charge density in attempt to respond to the perturbation. The excess in the electronic energy is reduced at the expense of the elastic energy of the chain, which increases as the atoms rearrange into a new lattice. The new lattice constant is $2a$ [see figure 1.5(b)]. Consequently, an energy gap of 2Δ opens exactly at E_F. In other words, the system stabilizes its state by undergoing a phase transition from a conducting to either semiconducting or insulating state. This phase transition is know as Peierls transition, since it was first proposed by Peierls in 1955 [9]. The density of the electron gas becomes modulated accordingly by waves with the wavelength $\lambda = \pi/k_F$, i.e.

$$\rho(x) = \rho_0[1 + \rho_{cdw}\cos(2k_F x + \theta)]. \tag{1.6}$$

These are called the charge density waves. Here ρ_0 represents the unperturbed charge density, v_F represents the Fermi velocity, ρ_{cdw} and θ are the amplitude the phase of the modulation. In this case, the wavelength of the modulation is the

same as the new lattice constant of the chain, hence the charge density waves are commensurate with the lattice. Otherwise, for arbitrary levels of filling, i.e. for arbitrary k_F values, charge density waves can be incommensurate with the lattice.

Let us now briefly discuss the behaviour of the system in figure 1.5(a) for $T > 0$ K. At any $T > 0$ K the chain atoms may oscillate around their equilibrium positions. The quanta of these oscillations are known as phonons. Similarly to electrons, the phonons are characterised by their dispersion relations $\omega_q(q)$, where ω_q represents the oscillation frequency and q represents the corresponding wave vector. Linear chain of atoms in figure 1.5(a) has only one phonon mode which now represents the perturbation to the system. At non-zero temperatures, the Lindhard function does not diverge but exhibits a peak at $q = 2k_F$. However, even in this case the charge density waves are possible. By decreasing the temperature the peak in the response function will become stronger until a critical temperature, called the Peierls transition temperature, T_{cdw} is reached. Then the system experiences the above described transition. The excess in the electronic energy, now, displaces the atoms thereby reducing the phonon frequency at $q = 2k_F$ as described by [8]

$$\omega^2_{reduced}(2k_F) = \omega^2(2k_F) - \frac{2g^2 n(E_F)\omega(2k_F)}{\hbar} \ln\left(\frac{1.14E_F}{k_B T}\right), \tag{1.7}$$

where g represents the electron-phonon coupling constant, and $n(E_F)$ represents the carrier concentration at the Fermi level.

At the Peierls transition temperature, for $q = 2k_F$, the atoms are locked in a new lattice [see figure 1.5(b)], the phonon mode completely vanishes, 2Δ gap opens at the Fermi level and the charge density waves are formed. Vanishing of the phonon mode is known as the Kohn anomaly, a phenomenon named after the physicist who described it in 1959 [10]. If we introduce $\gamma = g^2 n(E_F)/\hbar\omega(2k_F)$ as the dimensionless electron-phonon coupling constant then the amplitude of the charge density modulation in equation 1.6 becomes $\rho_{cdw} = \Delta/(\hbar v_F k_F \gamma)$. The size of the gap can be assessed from equation 1.7 for $\omega_{reduced}(2k_F) = 0$ as $2\Delta = 3.52 k_B T_{cdw}$ [8].

Finally, both the Peierls and the Kohn models do not predict the existence of charge density modulation in the two-dimensional electron gas having a circular Fermi surface. The reason is the lack of necessary energy gains, as corroborated by the corresponding Lindhard response function [see figure 1.6]. However, charge density waves are possible in two-dimensions in highly anisotropic materials if the necessary requirements in terms of the Fermi surface topology and the appropriate electron-phonon coupling are met [11]. Typically, for two-dimensional electron systems realised in such materials there is a number of possible nesting vectors which do not nest the Fermi surface perfectly, i.e. they connect only small parts of the Fermi surface. The nesting vectors are determined by the peaks in the response

function and only some of them lead to charge density waves. The choice of the right nesting vector(s) is usually not determined from the argument of better nesting since there are other physical mechanisms involved in the formation of these ground states, as pointed out by Johannes and Mazin in 2008 [12]. For instance, in rare-earth tellurides, the momentum-dependent electron-phonon coupling, which is in Peierles and Kohn models assumed to be independent on the momentum, is the main mechanism responsible for the choice of correct nesting vectors [13].

1.2.2 Two-dimensional electron-hole Coulomb coupled systems - excitons

When an electron is excited to the conduction band it leaves behind a positively charged particle, called hole. Under special circumstances the Coulomb interaction between the two particles can be strong enough to prevent the electron reaching the conduction band. In this case a Coulomb bound electron-hole pair called exciton is formed. Excitons exist in metals, semimetals, semiconductors and insulators. However, here we will focus on the direct band gap semiconductors. A direct gap semiconductor has the maximum of its valence band aligned with the minimum of its conduction band in the reciprocal space.

In semiconductors, the excitons are very similar to the hydrogen atom and are consequently modeled in similar fashion, by means of the Wannier equation. This equation is constructed in the exciton center-of-mass system by including electron and hole effective masses, the Coulomb interaction potential between the two and the dielectric constant of the semiconductor. Consequently, the excitons are characterised by their binding energies and Bohr radii. The former defines the energy necessary to decouple the electron-hole pair and in three-dimensional case is given by

$$E_{b,3D} = \frac{E_{R,3D}}{n^2}, \tag{1.8}$$

where $E_{R,3D}$ represents the exciton Rydberg energy and $n = 1, 2, 3...$ represents the excitonic state. The Rydberg energy, $E_R = \hbar^2/(2\mu a_{b,3D}^2)$, is usually given in the terms of the corresponding Bohr radius, $a_{b,3D} = \epsilon\hbar^2/(\mu e^2)$, which represents the mean distance between the electron and the hole. ϵ is the dielectric constant of the semiconductor and $\mu = m_e m_h/(m_e + m_h)$ is the reduced mass of the electron-hole pair. The total energy of the exciton is given by

$$E_{3D} = E_g - E_{b,3D} + \frac{\hbar^2 \mathbf{K}^2}{2\mu^*}, \tag{1.9}$$

where E_g is the energy gap, $\mathbf{K}$ is the continuous three dimensional wave vector of

the exciton and $\mu^* = m_e + m_h$ is the exciton's effective mass. These excitons are often referred to as Wannier excitons. In semiconductors, the dielectric screening of the Coulomb interactions is strong as quantified by the high values of their dielectric constants. Therefore, Wannier excitons have small binding energies, of the order of few meV, Bohr radii 10-100 times larger than the crystal's unit cell and are able to move through the crystal. Unlike Wannier excitons, Frenkel excitons, representing the other type of these quasi-particles, have higher binding energies (of the order of hundreds of meV) and Bohr radii comparable to the crystal's lattice constant. Frenkel excitons are named by the scientist who proposed the concept of exciton in 1931 and are found in materials with small dielectric constants, such as organic molecular crystals.

In two dimensions, when the semiconductor is thin enough to form a quantum well for both electrons and holes, excitons behave differently [14]. Here we will assume that the thin semiconductor and the surrounding media have approximately equal dielectric constants. The total energy of the exciton is then given by

$$E_{2D} = E_g + E_{quantized} - E_{b,2D} + \frac{\hbar^2 \mathbf{K}_{||}^2}{2\mu^*}, \tag{1.10}$$

Apart from the quantization of the exciton energy and restriction of the exciton motion in the direction perpendicular to the well's plane as indicated by $E_{quantized}$ and by the continuous in-plane exciton wave vector $\mathbf{K}_{||}$, the binding energy changes to

$$E_{b,2D} = \frac{E_{R,2D}}{(n - 1/2)^2}. \tag{1.11}$$

Comparison of equations 1.8 and 1.11 for $n = 1$ shows that the binding energy of an exciton in a quantum well is four times the energy of its three dimensional counterpart. This further implies that the Bohr radius of a confined exciton is reduced two times. In other words, when an exciton is created in a semiconductor quantum well, which is thinner than its Bohr radii, it will become smaller both in the direction perpendicular to well and in the well's plane, thus acquiring higher binding energy. Significantly reduced Coulomb screening in two-dimensions also contributes to the augmentation of the exciton's binding energy.

When the dielectric constants of the thin semiconductor layer and the surrounding media are significantly different, i.e. when the former is much larger than the latter, the exciton binding energy may be farther augmented through the local field effects. Such is the case with thin semiconductor layers deposited on a substrate.

Due to higher binding energies, confined excitons can be observed at room temperature in the absorption or photoluminescence spectra, in contrast to the bulk exctions. They are usually observed as strong, sharp spectral resonances in con-

junction with the corresponding subband transitions, just bellow the subband edges [see figure 1.8].

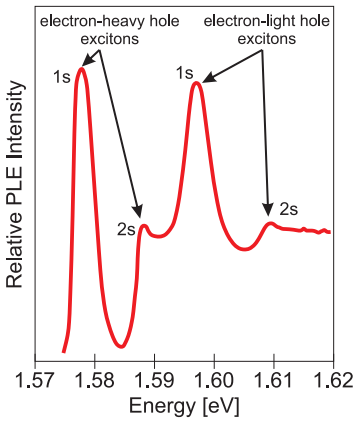

Figure 1.8: Photoluminescence spectra of GaAs/$Al_{0.33}GaAs_{0.67}$ multi quantum well. The peaks observed in this spectra originate from 1s and 2s excitons for the first electron-heavy hole and electron light hole transitions, respectively. Adopted from Ref. [15].

1.3 Two-dimensional materials - a novel perspective to two-dimensional systems

In the last decade two-dimensional materials have become one of the most popular topics in various fields of physics and chemistry. The recent rise of attention toward these materials is fueled by their newly discovered properties, such as high electron mobilities [16], topologically protected states [16], tunable band structures [17] and strong light-mater interactions [18; 19]. Two-dimensional materials are atomically thin crystal layers, which are building blocks of bulk layered crystals. A perfect example is graphene, a mono-layer of hexagonally arranged carbon atoms, which is a building unit of graphite [20]. Despite their recently gained popularity, atomically thin crystal layers were isolated and studied decades ago. In particular, mono-layers of molybdenum disulfide [21] and mono-layers of $Bi_8Te_7S_5$ were investigated in 1960s and 1970s, respectively [4]. However, the experiments performed in those days only scratched the surface of the unique properties these materials possess, and it was not until the (re)discovery of graphene that their potential became apparent. Nowadays, the family of two-dimensional materials has grown to include a large number of materials with very diverse properties, ranging from insulators to semiconductors to metals.

The specific band structures of two-dimensional materials along with the effects of the reduced dimensionality lead to appearance of phenomena that are different

not only from those observed in their bulk counterparts but also from those observed in their well known quantum well cousins [16; 22]. A perfect example is graphene in which the linear dispersion relation in the vicinity of K and K' points dictates the unusual behaviour of its charge carriers and determines its unique electronic and optical properties [22]. The charge carriers in graphene move without a mass at the velocity of $c/300$, where c is the speed of light. The concentration of charge carriers in graphene can be tuned between electrons and holes, via the electric field effect, up to extremely high values 10^{13} cm^{-2} with mobilities as high as 15000 cm^{-2}V^{-}1s^{-}1 at room temperature. These mobility values are much larger than those of commonly doped Si but smaller than those of GaAs/AlGaAs heterostructures [22]. In the limit of vanishing carrier concentration, graphene exibits a non-zero conductivity of $\sim 4e^2/h$ [22]. Graphene can absorb 2.3% of the incident visible light despite being one atom thick and its absorbance can be expressed in terms of fine structure constant [23]. The optical conductivity of graphene can be tuned in a broad range of frequencies by means of the electric field effect [24]. Another interesting example are the group-VI transition metal dichalcogenides. In the mono-layer limit group-VI transition metal dichalcogenides are direct-gap semiconductors as opposed to their bulk counterparts [17; 25]. Their optical response is dominated by excitonic effects due to reduced dielectric screening and enhanced Coulomb interactions [17]. In fact, the exciton binding energies are an order of magnitude higher that those observed in quantum wells, and reach hundreds of meV. Additionally, exciton complexes such as biexcitons and trions can be observed for high enough carrier concentrations at room temperature [17]. The selection rules for optical transitions at K(K') point, where the bandgap is, are valley-dependent, implying that the K(K) valley couples only to right (left) circularly polarized light [17; 25].

The properties of two-dimensional materials are also dependent on the presence of the substrate, adsorbates and structural defects, even though most of them are naturally passivated. The enhanced sensitivity to their surroundings implies that two-dimensional materials can be intentionally coupled to almost any other system [16; 26; 27]. For instance, coupling between plasmonic nano-objects and these materials is possible provided that these nano-objects lie on top or below the two-dimensional layer [26]. In addition, these materials can be combined in either vertical (without the lattice mismatch issue) or in-plane heterostructures, thus opening a possibility for engineering new materials with the desired properties [16; 28].

The diversity in electrical and optical properties, together with the ability to combine two-dimensional materials with other systems, points out to a plethora of possible device applications, making these systems even more relevant and interesting [18; 23; 26; 29; 30; 31; 32; 33]. For instance, figures 1.9 and 1.10, which are borrowed from Refs. [29; 32], should provide a general idea about the possibilities

and current level of technological implementation of two-dimensional systems.

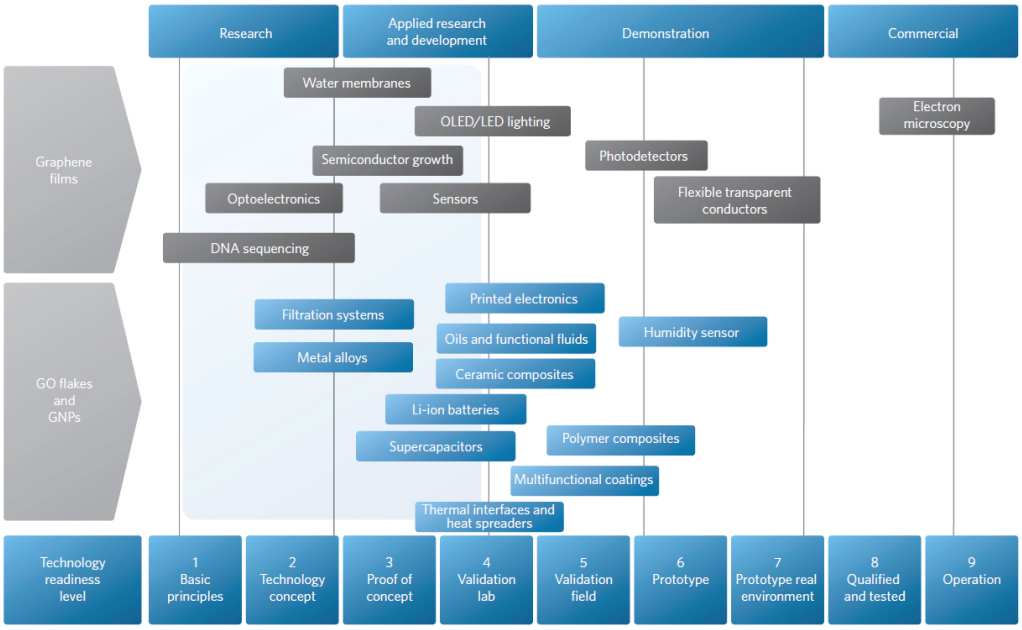

Figure 1.9: (a) List of possible applications of two-dimensional materials, formed with respect to the frequency spectrum range which the utilize. Below are the crystal structure of insulating hexagonal boron-nitride, semiconducting molybdenum disulfide and black phosphorus, and semimetallic graphene. Their respective band structures are shown below in panels (b), (c), (d), and (e). Adopted from Ref. [32].

Figure 1.9 shows some of the possible application of the two-dimensional materials. The applications are classified with respect to the spectral range they utilize. From this figure we see that a vide range of applications can be covered only by four representatives of this family of materials. Being a semimetal graphene interacts with electromagnetic radiation from the ultraviolet to radiowave wavelengths and thus covers the widest range of applications, including various photo-detectors, light modulators and RF circuits. On the other hand, the absence of an energy gap prevents graphene from being incorporated in light-emitting devices. Unlike graphene, molybdenum disulfide is a direct-gap semiconductor which exhibits superior optical properties than graphene in the visible region. However the applications of this material, such as photo-detectors and light emitting devices, are constrained only to this region.

Figure 1.10 illustrates the perspective and the current state of graphene, graphene oxide and graphene nano-platelet based devices. The applications of these materials range from optoelectronics, over sensors all the way to composite materials. However, only a small number of devices constructed from these materials have reached the prototype stage of development, whereas a few of them have reached the final commercial stage. Having in mind that graphene was introduced to the

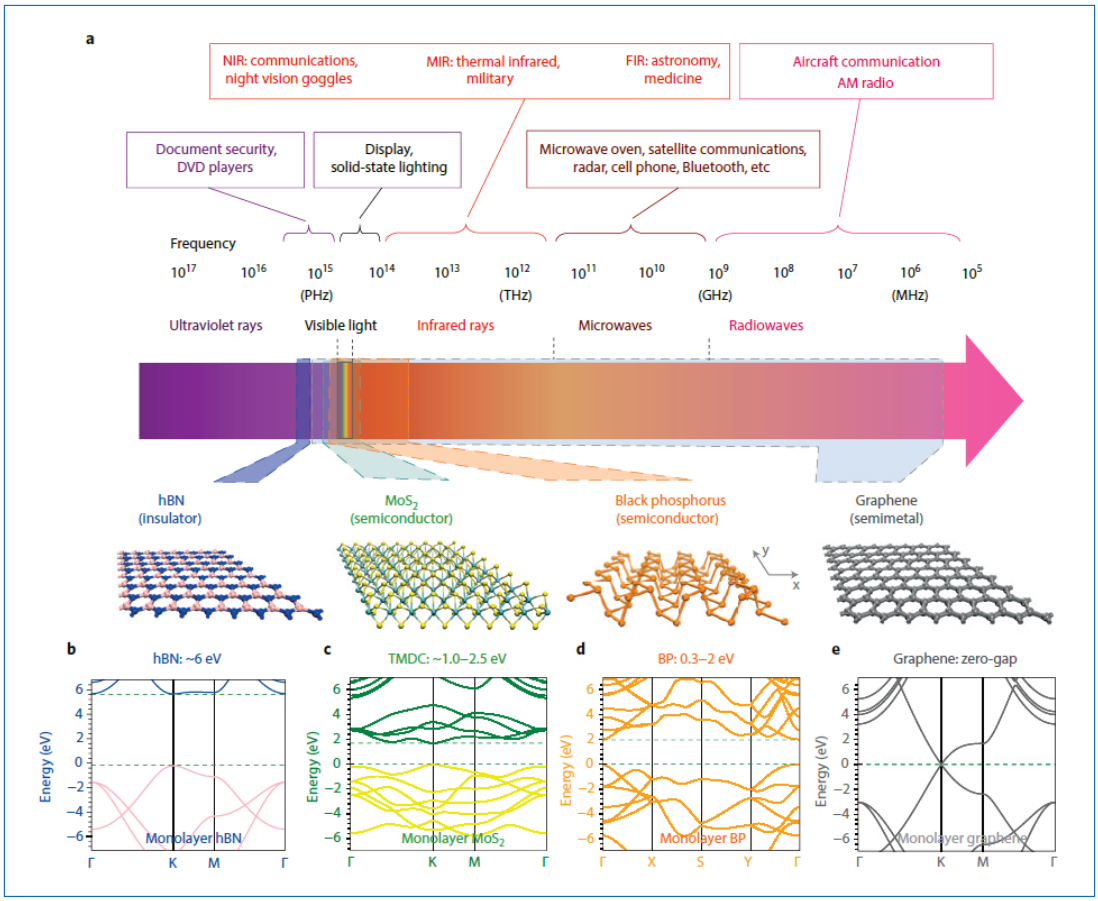

Figure 1.10: Perspectives and current state of graphene, graphene oxide and graphene nano-platelets based devices. Adopted from Ref. [29].

scientific community in 2004, this chart, which was made only ten years later, illustrates an enormous progress in graphene, graphene oxide, and graphene nano-platelet based technology even though the filed of two-dimensional materials is still young.

A part of this thesis is dedicated to two-dimensional systems realized within some of these 'newly emerged' family of materials. More specifically, two-dimensional charge carriers in garphene and two-dimensional excitons in mono-and few-layer molybdenum disulfide will be investigated. The reminder of the thesis deals with two-dimensional electron systems realized in highly anisotropic layered cerium tritelluride crystals and the surface plasmons realized in clusters of metallic nanoparticles.

1.4 Thesis Outline

The thesis is organized as follows. In the Second Chapter a brief overview of the experimental and numerical methods used for the investigation of named the two-dimensional systems is given. The Third Chapter is dedicated to charge density

waves in rare-earth tellurides. This study is done by means of scanning tunneling microscopy, and cerium tritelluride is used as the representative of this family of compounds. In the Fourth Chapter the gate modulation of charge carriers in graphene is studied by means of Kelvin probe force microscopy. In particular, operation of bare and isolated graphene samples in back-gate configuration is investigated, and the performance of these devices is compared. Additionally, in this chapter a potential application of graphene in electro-optical modulators is discussed. In the Fifth Chapter exctions of mono- and few-layer molybdenum disulfide in the presence of metallic nanoparticles are investigated by means of Raman spectroscopy. The Sixth Chapter is focused on application of surface plasmons and strongly localized electric fields in surface enhanced Raman spectroscopy.

Chapter 2 Methods

2.1 Nanoscopy methods

For the research presented in this thesis we have used a number of optical spectroscopy and scanning probe microscopy techniques capable of probing nanoscale systems. These techniques are labeled as nanoscopy methods in the title of this thesis. In this part we will give a brief introduction to each of those methods.

2.1.1 Scanning Probe Microscopy

Scanning probe microscopy (SPM) represent a family of techniques in which a sharp probe, also called the tip, is scanned over the sample's surface. The interaction strength between the sample and the tip, quantified by a measurable physical quantity, is used for extracting the topography of the surface. In particular, the value of the quantity which is measured is fixed by the operator. The changes in the measured quantity are registered by the instrument's electronics. Via the feedback loop the instrument modifies the tip-sample distance so that the signal value set by the operator is maintained. The corresponding change in the tip-sample distance represents the sample height. The scanning is done in a set of discrete points which form a matrix, and the height is evaluated in each of these points.

Interestingly, the original idea to use a sharp probe in order to obtain the surface topography can be traced back to 1929 when Schmaltz introduced his stylus profilometer. However, unlike the profilometer, SPMs are very sensitive instruments with high spatial resolution typically of the order of few nanometers. Under special conditions, these instruments are capable of resolving the atoms of the surface under investigation. High spatial resolution is enabled by: (i) extremely sharp tips (usually with apexes as small as few tens of nanometers), (ii) sophisticated piezo scanners capable of moving the tip and/or the sample by fractions of a nanometer, (iii) sophisticated systems which isolate the instrument from vibrations and (iv) sophisticated sensors which detect the tip-sample interaction.

There are two basic SPM subgroups classified depending on the quantity which is measured: the scanning tunneling microscopy (where the tunneling current between the tip and the sample is measured) and the atomic force microscopy (where the

forces between the tip and the sample or their gradients are measured).

2.1.1.1 Scanning Tunneling Microscopy

Scanning tunneling microscope (STM) was developed by Binnig and Rohrer in 1981. This device has earned them the Nobel prise in physics, a few years later. Moreover, the STM was the first fully developed microscope form the SPM family.

In scanning tunneling microscopy the tunneling current between the tip and the sample is measured. The tunneling process happens when a bias voltage, V_b, is applied between tip and the sample which are almost in contact (typical tip-sample separation is of the order of few tens of angstroms). The topography of the sample is acquired via the feedback loop which changes the tip-sample distance in order to maintain the predefined tunneling current setpoint, I_0, as it is illustrated in figure 2.1(a).

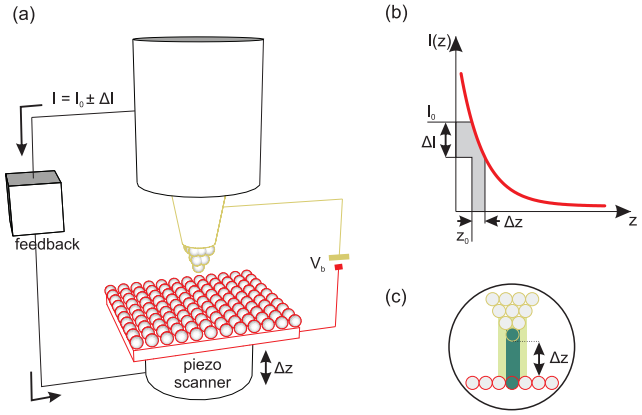

Figure 2.1: (a) Schematics of the scanning tunneling microscope. (b) The exponential dependance of the tunneling current on the tip-sample separation. (c) Magnification of the tip apex near the surface. The 90% of the tunneling signal comes from the outermost atom of the tip apex.

The tunneling current between the tip and the sample is approximately [34]

$$I \sim \int_0^{eV_B} \rho_{tip}(\pm E \mp eV_B)\rho_{sample}(E)T(E, eV_b, \Delta z)dE, \tag{2.1}$$

where ρ_{tip}, ρ_{sample} and T represent the local density of states (LDOS) at the tip apex, local density of states at the sample surface and transmission coefficient, respectively. In the WBK (Wentzel, Brillouin, and Kramers) approximation the transmission coefficient depends on the energy, bias voltage, V_b, and the tip sample distance, Δz and is given by [34]

$$T(E, eV_b, \Delta z) = T_0(E, eV_b)e^{-2\Delta z\sqrt{\eta(E,eV_b)}} \tag{2.2}$$

where $T_0(E, eV_b)$ and $\eta(E, eV_b)$ contain the work functions of the tip and the sample. Equations 2.2 and 2.1 show that the tunneling current has an exponential dependance on the tip-sample distance, making this kind of microscopy very sensitive to below angstrom changes in the tip-sample distance [see figure 2.1(b)]. This exponential dependance further renders a few atoms at the very end of the tip as the main contributors to the tunneling current, see figure 2.1(c). As such, STM is a technique able to achieve the atomic resolution. Due the very essence of the tunneling process one needs to recognize that the STM probes the quantum mechanical states of both the tip and the sample surface which are involved in the tunneling process [see equation 2.1 and figure 2.2]. Therefore, an additional power of this this technique is reflected in the fact that by simple change of the bias voltage one can study the spatial distribution of different states which are involved in the tunneling process.

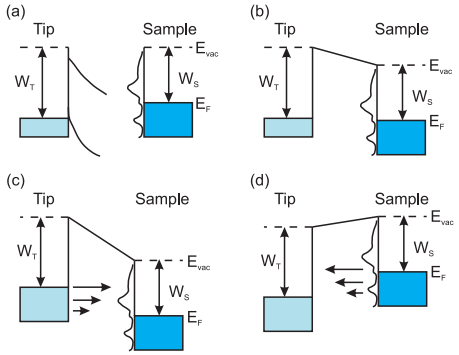

Figure 2.2: States involved in the tunneling process. Adopted from Ref. [34]. (a) The tip and the sample are far away and the tunneling does not exist. (b) The tip and the sample are very close to each other but the tunneling does not occur because the bias voltage is not applied. (c) Tunneling of electrons from the tip to the sample for positively biased sample. (d) Tunneling of electrons from the sample to the tip for negatively biased sample.

Furthermore, given the fact that the tunneling current is proportional to the integral of the samples's LDOS over the range of energies provided by the available range of V_b [see equation 2.1], one can, in principle, infer the sample's local density of states by differentiating equation 2.1 with respect to V_b. Under the assumption that the ρ_{tip} is constant, the differential conductance, dI/dV_b, becomes, to the first order approximation, directly proportional to ρ_{sample}.

In practice, dI/dV_b can be derived from point measurements of the tunneling current with respect to the bias voltage. During the measurements the feedback loop is broken in order to prevent modification of Δz. The resulting $I(V_b)$ curves are then differentiated with respect to V_b. The analysis of dI/dV_b is always a complex task due to the fact that both ρ_{tip} and T contribute to the tunnelling current. Nevertheless, this technique is particularly useful for assessing the gaps of semiconductors and,

in special cases, the gaps which are opened by occurrence of charge density waves or superconductivity. The existence of a gap is typically seen as a drop in the differential conductance within a certain energy range.

2.1.1.2 Atomic Force Microscopy

Atomic force microscope was developed by Binnig, Quate and Gerber in 1986. In AFM the force between the tip and the sample is measured. The tip is mounted on the cantilever which bends under the influence of the force between the tip and the sample. The bending of the cantilever is measured by means of sophisticated optical system which involves a laser diode and a four-segment photo-detector, as it is shown in figures 2.3 (b) and 2.3 (c). The light from the laser diode is focused on to the cantilever and reflected from it on the photo-diodes. Whenever the cantilever bends or twists the current on each photo-diode changes. The level of bending or twisting is proportional to the photo-current determined by adding or subtracting photo-currents from individual segments, as it is illustrated in figure 2.3 (d).

The AFM subgroup comprises many different techniques which are also called modes. The most relevant modes used for the research presented in this thesis are: (i) AFM contact mode in which repulsive short-distance forces are exploited [see figure 2.3 (a)], (ii) AFM tapping mode in which the tip is oscillated and passes through both the repulsive and attractive force regimes [see figure 2.3 (a)], (iii) Electrostatic AFM mode in which long-range electrostatic forces are exploited [see figure 2.3 (a)].

AFM contact mode. In contact mode, the displacement of the tip Δz, which bends the cantilever, is directly proportional to the force between the tip and the sample via the Hooke's law, i.e. $F = -k\Delta z$. k represents the spring constant of the cantilever. The topography is obtained via the feedback loop which adjusts the tip-sample distance, i.e. tip displacement, in order to maintain the predefined force setpoint. The measurement is done in a set of discreet points, which at the end form a matrix of the sample height. Additionally, due to the fact that the tip is practically dragged over the sample's surface, the twisting of the cantilever can be registered as well, thus, providing a spatially resolved map of the friction force between the tip and the sample [see figure 2.3 (b)].

AFM tapping mode. In tapping mode, the cantilever is oscillated near its resonant frequency. The name tapping comes from the fact that the tip is periodically 'touching' the sample surface. In its full motion the tip is therefore going through both the repulsive and attractive force regimes [see figure 2.3 (a)]. Hence, in tapping AFM the force gradient is probed, rather than the force itself. The topography

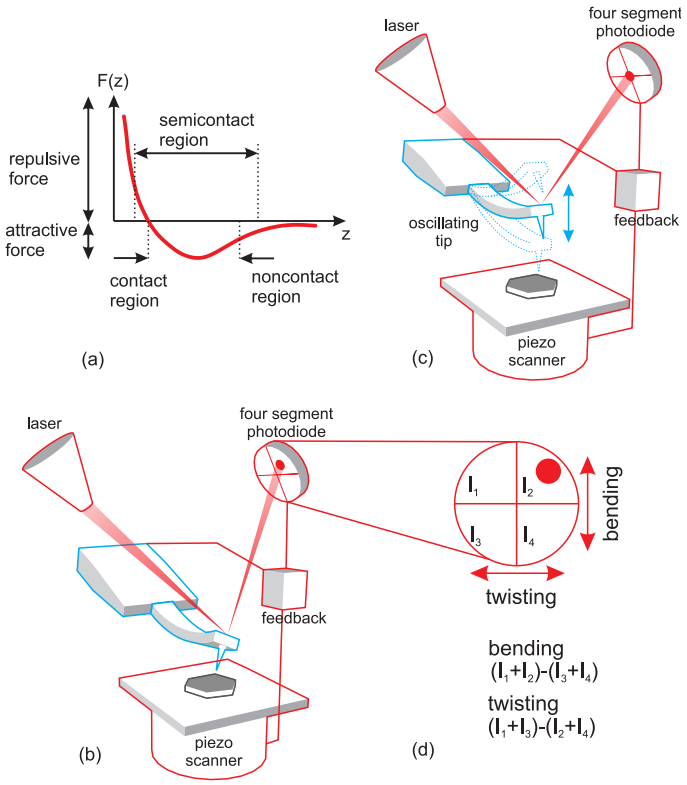

Figure 2.3: (a) The Lenard-Jones force curve. Schematics of the atomic force microscope in (b) contact mode, (c) tapping mode. (d) Operational principle of the four segment photo-detector.

is obtained by maintaining the predefined setpoint of the amplitude of cantilever oscillations which is sensitive to the tip-sample distance [see figure 2.3 (c)]. This mode is particularly well suited for soft samples since the friction force between the tip and the sample is minimized.

The tip-sample interaction also affects the frequency and the phase of the oscillations. The shift in the frequency is small and therefore harder to detect than the phase shift. The phase shift is directly related to the energy spent to compensate the losses during the dissipative interaction between the tip and the sample and therefore can be used for imaging the difference in material properties of the sample's surface, if any exist.

Electrostatic force modes. In electrostatic force modes one exploits the long range electrostatic forces between the tip and the sample. There are two available techniques which are commonly used: Kelvin probe force microscopy (KPFM) and electrostatic force microscopy (EFM). The two techniques are very similar in terms of the requirements needed for their implementation. The main difference arises from the quantities which are measured.

Both KPFM and EFM are two pass techniques, since during one measurement

cycle the tip passes over the surface twice. In the first pass the topography of the sample is acquired utilizing the tapping mode [see figure 2.4]. Then the tip is lifted above the sample surface at height Δh (ranging between 10 nm and 100 nm) at which the long-range electrostatic forces have the dominant contribution in the interaction between the two. The second pass is therefore performed when the tip is lifted. In order to further minimize the influence of the sample topography, the topography profile acquired in the first pass is followed during the second pass [see figure 2.4]. Switching between first and the second pass is done for every line during the scanning.

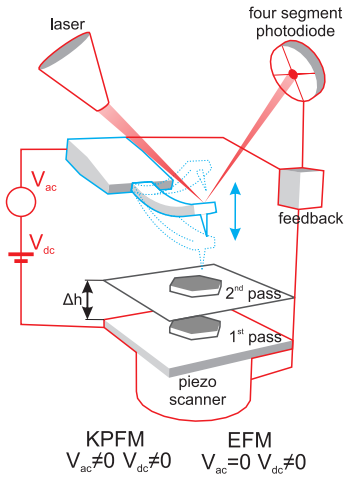

Figure 2.4: Schematics of the atomic force microscope in the electrostatic mode.

The key factor in KPFM and EFM is the electrostatic interaction between the tip and the sample which is achieved by creating a potential difference between the two during the second pass. By considering the tip-sample system as a capacitor, the electrical force existing between them can be written as

$$F_e = \frac{1}{2}\frac{dC}{dz}V^2, \tag{2.3}$$

where C and V represent the capacitance of the tip-sample capacitor and the potential difference between the tip and the sample, respectively. From this point on the two methods differ and we shall consider one at a time.

- In KPFM an oscillating voltage, $V_{tip} = V_{dc} + V_a c\sin(\omega t)$, is applied to the tip, as it is illustrated in figure 2.4. The frequency of the applied voltage, ω, is chosen to be very close to the frequency of the mechanical resonance of the cantilever. The cantilever oscillations during the second pass are not driven by mechanical excitation but by the oscillating electrical force F_e. The potential difference is defined as, i.e. $V = V_{dc} + V_{ac}sin(\omega t) - V_{CPD}$, where $V_{CPD} = 1/e(W_{tip} - W_s)$ represents the tip-sample contact potential difference.

W_{tip} and W_s are the work functions of the tip and the sample, respectively. Plugging the expression for V in the into equation 2.3 results in three force components contributing to the tip-sample interaction, i.e.

$$F_{dc} = \frac{\partial C}{\partial z}\left\{\frac{1}{2}(V_{dc} - V_{CPD})^2 + \frac{V_a c^2}{4}\right\}$$
$$F_{\omega} = \frac{\partial C}{\partial z}\left\{\frac{1}{2}(V_{dc} - V_{CPD})\right\}\sin(\omega t)$$
$$F_{\omega t} = -\frac{1}{4}\frac{\partial C}{\partial z}V_a c^2 \cos(2\omega t)$$

By means of a lock-in amplifier one is able to extract the amplitude of the force induced cantilever oscillations at the resonant frequency ω and read out the V_{dc} for which the relevant component of the electric force becomes zero. This voltage is equal to the contact potential difference between the tip and the sample. Ultimately, if the work function of the tip is known one can assess both the surface potential, $1/eW_s$, and the work function of the sample's surface.

- In EFM a constant voltage, $V_{tip} = V_{dc}$, is applied to the tip as it is illustrated in figure 2.4. Here, however, the tip is mechanically excited to oscillate at its resonant frequency ω, similarly as in the tapping mode. The potential difference is defined as $V = V_{dc} - V_{CPD}$. By contrast, in EFM the force gradient between the tip and the sample is probed instead the force itself. The phase shift of the cantilever oscillations induced by the force gradient is measured. In case of small force gradients, the phase shift can be obtained from [35]

$$\Delta\phi = -\arcsin\left\{\frac{Q}{2k}\frac{d^2C}{dz^2}(V_{dc} - V_{CPD})2\right\}, \tag{2.4}$$

where k and Q represent the spring constant and the quality factor of the cantilever.

From equation 2.4 we see that the tip-sample contact potential difference can be also measured by EFM.

2.1.2 Optical Spectroscopy

Optical spectroscopy refers to all methods in which a light source, spectrally broad or narrow, is shined on the sample and the transmitted, reflected and/or scattered light is then used for the assessment of the optical properties of the sample. In this

thesis we have used spectrophotometry, Raman spectroscopy and surface enhanced Raman spectroscopy.

2.1.2.1 Spectrophotometry

Spectrophotometry is a method used for determination of the absorbance of a sample. It is based on measuring the intensity of the light, transmitted through the sample under investigation. The working principe of the so-called double beam configuration, which is the widely used one, is show in figure 2.5. By means of a diffraction grating, a specific wavelength of the incident white light is passed through the sample and the reference. The difference of the two measured intensities corresponds to the light which is effectively transmitted through the sample, I_t. The absorbance is obtained as $A = \log I_t/I_0$ where I_0 represents the incident light intensity at a given wavelength.

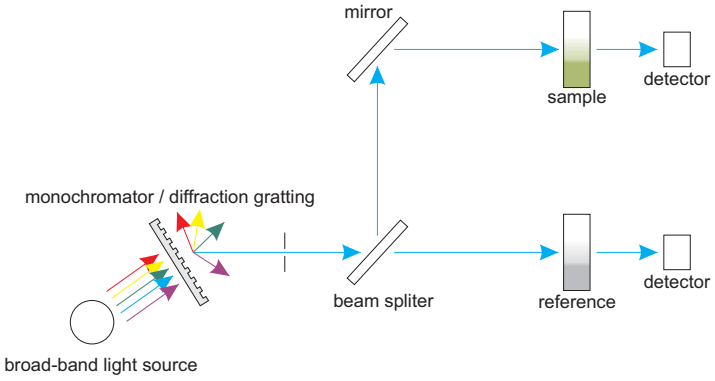

Figure 2.5: Schematics of a double beam spectrophotometer.

2.1.2.2 Raman Spectroscopy

Raman spectroscopy is a method used for characterisation of the vibrational / rotational transitions in matter. It is based on the light scattering effect predicted by Smekal in 1923 [36] and observed in many experiments on light scattering by vapours, liquids and solids which Raman conducted systematically over several years [37] and eventually published in 1928 [38]. Two Russian physicists, Landsberg and Mandelstam, have almost simultaneously and independently discovered the effect in quartz crystal. However, only Raman received the Nobel Prize in Physics for 1930, which generated some controversy over the years [39]. Even today, Raman scattering is referred to as combination scattering in the Russian literature.

In a Raman scattering experiment a light source is shined on a sample (e.g. a crystal) under the investigation. The incoming electric field induces a net dipole moment which is subsequently modulated by the vibrations of the crystal lattice

(phonons). The resulting net dipole moment consequently oscillates at the frequency ω of the electric field and at the phonon frequencies $\pm\omega_R$. The irradiated light will, therefore, have three components corresponding to the following scattering events: (i) an elastic scattering event in which the the emitted photon has the same energy ,$\hbar\omega$, as the incident one (Rayleigh scattering), and (ii) an inelastic scattering event in which the emitted photon has either higher or lower energy by amount equal to the phonon energy, $\hbar(\omega \pm \omega_R)$. The latter are the photons originating from the Raman scattering process. Photons with lower energy $\hbar(\omega - \omega_R)$ represent the Stokes component of scattered light, whereas photons with higher energy $\hbar(\omega + \omega_R)$ represent the anti-Stokes component of scattered light [see figure 2.6(a)].

The Raman scattering process is extremely weak, compared to Rayleigh scattering. Only a small fraction of the incident photons (typically 1 in 10 million) are Raman scattered. The Stokes scattering is more probable event than the Anti-Stokes scattering. Consequently the Stokes component of the scattered light is stronger than the Anti-Stokes component, and therefore the one which is usually measured in a Raman experiment.

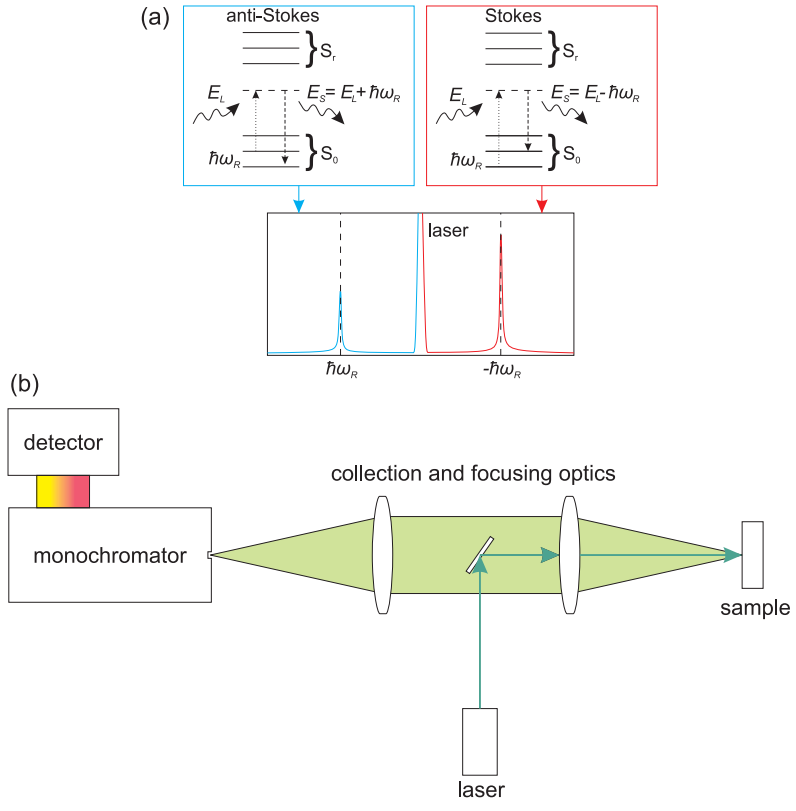

Figure 2.6: (a) Diagrams illustrating the energy transition for inelastically scattered Raman signal. $E_L = \hbar\omega$ and $E_s = \hbar(\omega \pm \omega_R)$ represent the energy of the incident and scattered photon. (b) Single monochromator Raman setup.

Lasers are commonly used as light sources in Raman spectroscopy. The basic, single-monohromator Confocal Raman instrument in reflection configuration

is shown in figure 2.6(b). The light is focused on the sample's surface by a systems of lenses, i.e. the objective. Then, the light is reflected from the sample and travels back through the objective and collection optics to the monochromator. In most cases, the strong Rayleigh component is removed before the light enters the monochromator by means of either an edge pass filter or a band pass filter. This is done in order to protect the very sensitive photo-detector. In the monochromator the light is collimated by a system of mirrors and spatially dispersed by a diffraction grating onto the sophisticated CCD photo-detector. The CCD photo-detector is typically cooled below the room temperature in order to reduce the background noise which further improves its sensitivity. At the output one gets the wavelength resolved Raman spectra expressed in counts which represent the number of photons detected at each pixel of the CCD.

The Raman scattered signal is measured relative to the wavelength of the incident laser light. The corresponding spectra is expressed as a function of the relative energy shift, called the Raman shift, which is usually expressed in wavenumbers.

Surface Enhanced Raman Spectroscopy. In order to overcome the problem of small intensity of Raman signals, surface enhanced Raman spectroscopy (SERS) is often used. SERS was observed for the first time in 1974 [40] by Fleischmann and explained a few years later [41; 42]. This techique mainly utilizes rough metallic surfaces and small metallic nanoobjects as enhancers of the Raman signal of the nearby analyte. There are two mechanisms responsible for the enhancement. The first is the chemical enhancement, resulting from the charge transfer between the analyte and rough metallic surfaces or metallic nanoobject. The other, dominant, mechanism is the electromagnetic enhancement. This mechanism was considered by many scientists during the 1980s, but was elaborately described by Kerker whose model is still used today [43].

The electromagnetic enhancement mechanism is based on the strong electromagnetic fields localised at and in the close vicinity of small metallic objects. In fact, these strong felds can transfer electromagnetic energy to the analyte which is either adsorbed or very close to the surface of these objects, thus increasing the magnitude of the analyte's phonon-modulated dipole moment. This leads to the enhancement of the inelastically scattered light intensity and therefore to the enhancement of the Raman scattering efficiency. The fields are a consequence of either excited localised surface plasmons or simply of the fact that the electric fields are strong and localised at and in the vicinity of the surface of small metallic objects. The enhancement factor is often estimated as $F = |E/E_0|^4$, where E represents the amplitude of the scattered electric field and E_0 represents the amplitude of the incident electric field. SERS enhancements can be as high as $F \sim 10^{11}$, allowing one to conduct very

sensitive studies on single molecules.

2.2 Numerical Methods

In this part we will briefly discuss the numerical methods, namely the reflection pole and finite element methods, used for the investigation of the optical properties, spectroscopic data and some potential applications of two-dimensional systems.

2.2.1 Reflection Pole Method

The reflection pole method (RPM) is used for numerical calculation of the eigenmodes in lossless and lossy stratified (planar) waveguides [44]. It is easily implemented and it is based on the analysis of the complex reflection coefficient of the system under investigation. The eigenvalues (complex propagation constants of eigenmodes) are seen as poles in the systems response to a plane wave excitation. In other words, the reflection (and transmission) coefficient diverges whenever a guided mode is supported by the waveguide.

The complex reflection and transmission coefficients of stratified planar waveguides can be obtained using the transfer matrix formalism. In this formalism the wave in each layer is described by a vector whose two components are the complex amplitudes of the forward and backward waves in the considered layer. The transfer matrix between adjacent layers, establishing the connection between the two vectors, is determined from the interface boundary conditions. For instance, matching of the tangential field components at every layer interface of the waveguide in figure 2.7 gives

$$\begin{pmatrix} t_{s,p}E_0 \\ 0 \end{pmatrix} = M \begin{pmatrix} E_0 \\ r_{s,p}E_0 \end{pmatrix} \tag{2.5}$$

where $M = \begin{pmatrix} a & b \\ c & d \end{pmatrix}$ represents the transfer matrix, $r_{s,p}$ and $t_{s,p}$ represent the reflection and transmission coefficients for both s- and p- polarized fields, respectively. The transmission and reflections coefficients can be straightforwardly obtained from equation 2.5 as $r_{s,p} = -c/d$ and $t_{s,p} = (ad - bc)/d$. Therefore, in case of a guided mode $d \to 0$.

The ω, β pair corresponding to the frequency and the complex propagation constant of a guided modes are then found using the Nelder-Mead algorithm implemented within the *fminsearch* function in Matlab software package.

A major advantage of RPM over other methods is reflected in the fact that this method can determine the exact number of the allowed modes in a waveguide structure.

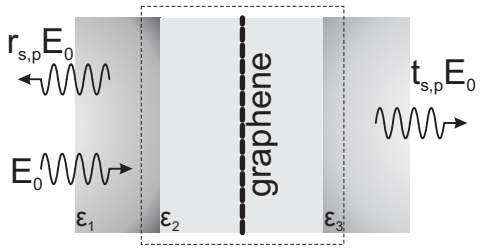

Figure 2.7: Schematics of a planar dielectric waveguide with graphene embedded into its center.

2.2.2 Finite Element Method

Finite element method (FEM) is a numerical technique utilized for solving problems described by partial differential equations which cannot be solved analytically. The name finite elements originates form the elements used to represent the domain of interest. The basic procedure of solving a continuous physical problem using FEM is as follows.

The first step is discretization of the domain of interest by diving it into finite elements. A group of connected finite elements is called the mesh. Examples, of the finite element meshes in two and three dimensions related to the problems addressed in this thesis are shown in figure 2.8 and figure 2.9. In the two dimensional case we use triangular elements, whereas in three dimensional case we see combination of tetrahedral and hexahedral elements. The choice of mesh and its size is very important since it determines the accuracy of the solution. If the mesh is not fine enough the solution might not be well resolved and erroneous. The mesh resolution depends on the problem which is solved and therefore on the solution which is sought.

The next step consist of selection of the interpolation functions, which are used to interpolate the solution over the element. These function are defined within the element using its nodal values. Polynomials are a typical choice for interpolation functions. The degree of the polynomial is determined with respect to the number of nodes of the element.

After this, a matrix equation for each of the finite elements is established. The matrix equation relates the nodal values of the solution which is sought to other parameters. The most commonly used approach for finalizing this step is the Galerkin method. This is followed by connecting the local element equations in to the global equation system, including the appropriate boundary conditions.

The final step is solving the imposed global equation system by either direct or iterative methods. As a result one gets the nodal values of the solution function.

In this thesis, FEM realised in COMSOL software [45] is used for solving Maxwell's equations describing: (i) electromagnetic fields in waveguides such as

the one in figure 2.8 and (ii) scattering of a plane wave incident to nanoparticle clusters residing on a substrate. The former is an eigenvalue problem, whereas the latter is a stationary frequency problem. The two are very different and require special FEM setups and analysis.

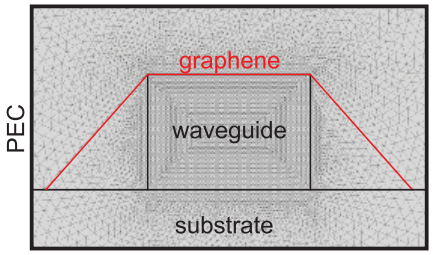

Figure 2.8: Finite element mesh in case of a two dimensional problem.

The eigenvalue problem is solved for the electric field and complex propagation constant. The computational domain is terminated by boundaries at which the tangential component of the electric field is zero (the perfect electric conductor boundary condition, PEC). The waveguide is located within the domain. In eigenvalue mode, FEM gives all possible solutions of the considered system, including those which do not represent the guided modes. The right solutions are characterised by the fields which are confined to the waveguide region while decreasing toward the boundaries of the domain. Therefore, a special attention should be paid to the size of the computational domain. Namely, the domain should be large enough that the field amplitudes fall to zero before the domain boundary is reached. Otherwise, the calculated propagation constants would be incorrect. Obviously, large domains imply large number of mesh elements which come at the expense of high computational cost. This problem can be addressed, to a certain degree, by adjusting the size of the finite elements within the domain. In this case field variations determine the minimal number of the mesh elements. For example, in figure 2.8 we see a very fine mesh in the waveguide region and near the waveguide borders where the field is expected to vary significantly. The mesh becomes coarser toward the domain boundaries since smaller variations of fields are expected.

The stationary frequency problem is solved for the scattered electric fields at a given frequency. This requires separation of the total field into the incident (background) and scattered fields. The background field is known and defined as if the object which scatters it does not exist. Then solving Maxwell's equations for the total field reduces to solving Maxwell's equations for the unknown scattered field in the presence of a known background field. The total computational domain is separated into physical domain and the domain of perfectly matched layers (PML), as illustrated in figure 2.9.

The background field is defined only in the physical domain and the PMLs exclu-

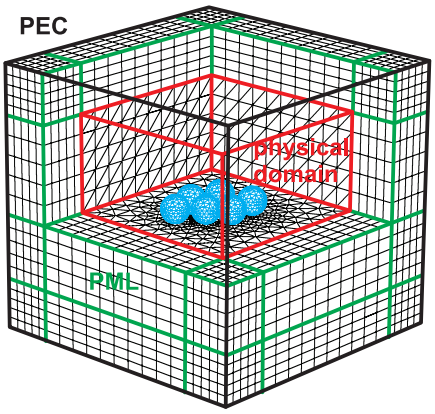

Figure 2.9: Finite element mesh in case of a three dimensional problem.

sively serve to absorb the scattered field. As in the previous case the computational domain is truncated by PEC. When dealing with this kind of numerical simulations one needs to carefully address two important things. The first is the mesh. In this case the minimal number of mesh elements is determined by both field variations and its wavelength. To resolve the background electric field ten mesh elements per wavelength should be enough [see figure 2.9]. For the scattered fields in the vicinity of the nanoparticles, the number of mesh elements should be much larger [see figure 2.9]. The second is the PML which needs to be adjusted to effectively absorb the scattered fields and prevent their reflection from the domain boundaries. The best way to choose the right PML parameters is through trial and error, by monitoring how the filed behaves inside them. In a good PML the field should decay from the inner to the outer side of PML reaching zero values at PEC boundaries, at a given frequency.

Chapter 3 Charge density modulations of the two-dimensional electron gas in cerium tritelluride

Charge density waves (CDW) have been a subject of considerable interest in condensed matter physics for many decades [8]. Originally predicted and observed in one-dimensional systems, CDW formation was found also in many two-dimensional materials where the ordered state remains metallic in most of the cases. Occasionally, the CDW phase is in close proximity to other phases such as superconductivity [46; 47].

The rare-earth tritellurides [48] $R\mathrm{Te}_3$ are excellent model systems for systematic studies of the underlying physics for the wide range of tunable parameters such as transition temperature T_{CDW}, Fermi surface shape, c-axis coupling, anisotropic or weak versus strong electron-phonon coupling [13; 49; 50; 51; 52; 53; 54; 55].

In this chapter, we study the CDW modulation in CeTe_3 at room temperature by means of STM, scanning tunneling spectroscopy (STS) and Raman scattering measurements.

3.1 Materials and Methods

Single crystals of CeTe_3 were grown by slow cooling of a binary melt. The details are published elsewhere [50]. The samples for STM measurements were prepared at Brookhaven National Laboratory, whereas those for Raman scattering at Stanford University. Because the compound oxidizes in ambient air, the crystals were cleaved with adhesive tape in order to remove the oxidized layer.

The STM measurements were done in ultra-high vacuum at room temperature, using a commercial OMICRON UHV STM system. Topography imaging was done in constant current mode with the bias voltages in range of 0.1-0.9 V applied to the tip. Tilting error compensation, Fourier noise filtering, and scanner distortions removal were done using Gwyydion image processing program [56]. Every STM topograph and its corresponding current image are displayed with their raw Fourier transform, used for the filtering procedure. It should be noted that the displayed raw Fourier images have vertical bands of intensities which originate from a large

number of noise induced periodic components in the real space images along the fast scanning axis (x axis). These bands are, therefore, measurement artifacts rather than physical features of the sample. STS measurements were done in point probe mode at different locations on the sample surface, also at room temperature. The I-V curves were made for bias voltages ranging from -0.5 V to 0.5 V, with a resolution of 0.02 V, which is comparable to the thermal noise of about 0.026 eV. Consequently, the CDW gap is evaluated with accuracy of $\sim \pm 2 \times 0.026$ eV.

For the Raman scattering experiments we have used the line at 458 nm of an Ar ion laser as an excitation source. The absorbed laser power ranged from 1 to 2 mW to keep the local heating below 5 K in the $50 \times 100\,\mu\text{m}^2$-sized focus, as estimated from comparing energy gain and loss spectra [57]. Since there is no phase transition in close proximity a temperature gradient in the spot can be neglected here. The spectra were measured with a resolution of 2.5 cm^{-1} at low energy and 20 cm^{-1} at high energy. The Raman response $R\chi''(\Omega)$ is then obtained by dividing the measured spectra by the thermal Bose factor. We present symmetry-resolved spectra, obtained from linear combinations of spectra measured at the main polarization configurations [58], in order to separate out the A_{2g} contribution which, in the non-resonant case, is insensitive to the carrier (particle-hole) excitations we are interested in.

3.2 Results and discussions

3.2.1 STM topography measurements

$CeTe_3$ crystals are layered two-dimensional materials with orthorhombic crystal structure that adopts the $Cmcm$ space group symmetry [59]. The layers are composed of a corrugated CeTe slab sandwiched between two planar Te sheets and connected together via weak van der Waals forces. Figure 3.1 (a) shows the crystal structure of $CeTe_3$ with the unit cell indicated by dashed lines. For the $Cmcm$ space group the a and c are the in-plane crystal axes and b is the long crystal axis.

An isolated planar Te sheet with a nearly perfect square lattice has one Te atom in the corresponding unit cell, as opposed to the full crystal which has two distinct Te sites in the planar Te sheets (see the lower part of figure 3.1 (a)), and twelve Te atoms per unit cell (see the upper part of figure 3.1 (a)). As an example, in figure 3.1 (b) the Te square lattice of $CeTe_3$ obtained by setting the bias voltage, V_b, to 0.8 V and the set-point current, I_s, to 0.6 nA, is shown. The corresponding raw Fourier transform is given in the inset. Four distinct peaks, labeled as A, form the reciprocal lattice of the atoms in the Te sheets, and are approximately $2\pi/a_0$=20.43 nm^{-1} from the origin, denoted as O. The average distance between the neighbouring Te atoms can be straightforwardly assessed from the position of

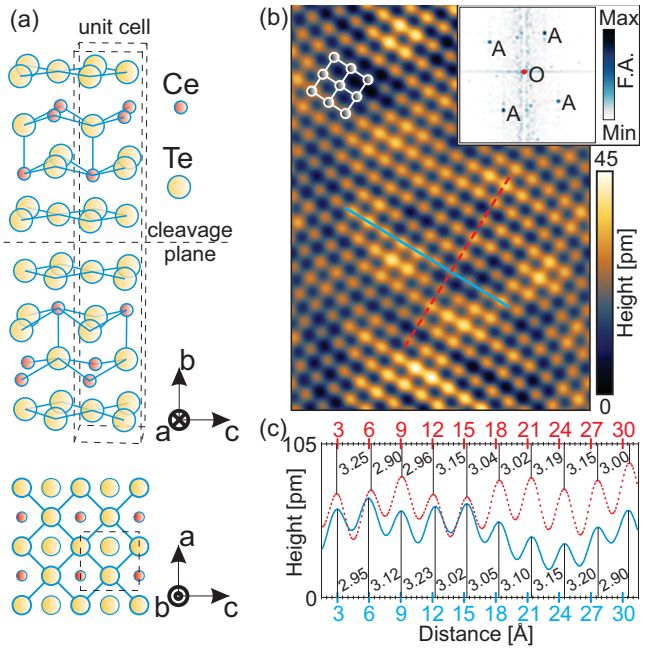

Figure 3.1: (a) Crystal structure of $CeTe_3$. The lower part shows a view on the top Te layer connected by blue lines oriented at 45° with respect to the a and c axes. The atoms of the Ce-Te layer are not connected. (b) Filtered STM topograph obtained for V_b =0.8 V and I_s =0.6 nA. The inset shows corresponding Fourier transform (F.A. stands for Fourier Amplitude); (c) Profiles along the solid (blue) and dashed (red) lines in panel (b) showing variation of the Te-Te distances in the Te sheets. The assessed distances between the adjacent Te atoms are written in-between the black vertical lines which show the position of the profiles maxima.

the A peaks, i.e. $a_0 = 2\pi/20.43\,\mathrm{nm}^{-1}$=0.3075 nm. However, profiles taken along the solid (blue) and dashed (red) lines in figure 3.1 (b) reveal that the distances between the maxima, representing the Te atoms, vary around a constant separation of $2\pi/20.43\,\mathrm{nm}^{-1}$=0.3075 nm. We find that all of the images, obtained with the same set of tunneling parameters as the one in figure 3.1 (b), show similar variation of the Te-Te distances. The variation of the Te-Te distances is very subtle and can not be assessed from the full width at half maximum of the A peaks (see the inset in figure 3.1 (b)). Therefore, the Fourier transform provides the average interatomic distances indicating an ideal Te square lattice, whereas the analysis of the real space images yields irregular Te-Te distances.

Given the weak hybridization between the CeTe slab and the Te sheets [49; 60], the electronic properties of $R\mathrm{Te}_3$ are predominantly determined by the planar Te sheets. Having a weak interaction along the b axis, these compounds are often considered two-dimensional systems. The main contribution to the CDW comes from the states close to the Fermi level. These states mainly derive from in-plane p_x and p_z orbitals with 5/8 filling due to the underlying CeTe layer, which donates an electron shared between two atoms in the upper and lower Te sheet. The out-of-

plane p_y orbital is lower in energy than the in-plane p_x and p_z orbitals and is pushed below the Fermi level. Now, assuming an isolated Te sheet with an ideal square lattice, while neglecting the hopping between p_x and p_z orbitals, one could calculate the Fermi surface [13; 49; 61] within the corresponding Brillouin zone similar to the one sketched in the inset of figure 3.2 (a) with solid and dashed (red) lines. In the scope of this approximation, there are two possibilities for the nesting vectors, $\mathbf{q}$ and $\mathbf{q}^*$ [12; 49] (see the inset of figure 3.2 (a)) which are not related by the C_4 symmetry of the assumed host lattice. The rest of the nesting vectors which are symmetry related to the $\mathbf{q}$ and $\mathbf{q}^*$ are described in Ref. [49]. The $\mathbf{q}$ vector nests both the p_x (dashed red lines) and the p_z (solid red lines) portions of the Fermi surface, whereas the $\mathbf{q}^*$ nests only the p_x portion of the Fermi surface [49]. Assumption of a purely nesting-driven instability allows the system to choose between the two nesting vectors depending on the strength of the electron-phonon coupling: $\mathbf{q}$ and the stripe symmetry of the CDW state are favored when the coupling is strong [49]. It was recently shown [13], however, that the inclusion of the interaction between p_x and p_z modifies the Fermi surface, thus, enabling large electron-phonon coupling near the band degeneracy points and renormalization of the phonon frequency only at the $\mathbf{q}$, rather than at $\mathbf{q}^*$. In fact, renormalization at $\mathbf{q}^*$ and the related checkerboard symmetry of the CDW state were not observed experimentally.

Figure 3.2 (a) shows the topography of $CeTe_3$ with clearly visible CDW modulation. This image is obtained for V_b=0.2 V and I_s=0.6 nA. The corresponding Fourier image is given in figure 3.2 (b). As before, there are four peaks representing the Te sheet atoms. They are labeled by A. Peaks labeled by A′ correspond to the additional periodicity arising from the inequality of $\mathbf{a}$ and $\mathbf{c}$ lattice vectors which is a consequence of the orthorhombic crystal structure. In other words, these peaks should exist for any set of tunneling parameters for which the tunneling between the tip and the Te planes is possible. In fact, the A′ peaks exist in figure 3.1 (b) as well, but are barely visible since the inequality between $\mathbf{a}$ and $\mathbf{c}$ is very subtle. The intensity of the A′ peaks in figure 3.2 (b) is enhanced by the additional periodicity of the underlaying Ce atoms, whose f states have significant contribution to the tunneling current [62] when the tip is close to the surface, i.e. for lower bias voltages. Accordingly, we assign $\mathbf{c}^*$ and $\mathbf{a}^*$ wavevectors to the A′ peaks, where $|\mathbf{c}^*| = 2\pi/|\mathbf{c}|$ and $|\mathbf{a}^*| = 2\pi/|\mathbf{a}|$. The $\mathbf{c}^*$ connects the origin O and the A′ peak on the main diagonal, and the $\mathbf{a}^*$ is perpendicular to $\mathbf{c}^*$. We assess the magnitude of the two wavevectors to be around 14.4 nm^{-1}.

Apart from A and A′ peaks, the Fourier amplitude image in figure 3.2 (b) exhibits new features in comparison to the one shown in figure 3.1 (b). The peak located below the A′ peak on the main diagonal, Q, corresponds to the $\mathbf{q}$ nesting vector, while the Q′ peak corresponds to the $\mathbf{q}'$ vector. Following the work in Ref. [13] we

set the $\mathbf{q}$ as the dominant CDW ordering vector, which further gives $\mathbf{q}' = \mathbf{c}^* - \mathbf{q}$. The magnitudes of $\mathbf{q}$ and $\mathbf{c}^* - \mathbf{q}$ vectors are $10.26\,\mathrm{nm}^{-1}$ and $4.19\,\mathrm{nm}^{-1}$, respectively. The related wavelengths are $\sim$0.61 nm (distance between (black) circles in figures 3.2 (c) and (d)) and $\sim$1.5 nm (distance between (red) squares in figures 3.2(c) and (d)), respectively. Displayed in figures 3.2 (e) are the profiles along main and side diagonal of the Fourier image, showing the exact position of the mentioned peaks. The Q peak is more intensive than the Q$'$ peak which is barely visible on the main diagonal, but clearly visible on the side diagonal. The absence of the Q or Q$'$ peaks on the main diagonal in figures 3.1 (b), is due to the small, practically negligible, overlapping of the CDW wavefunction, which decays exponentially out of Te sheet, and the tip wavefunction. In fact, significantly reduced overlapping between the two wavefunctions for $V_b = 0.8\,\mathrm{V}$ results in a reduced CDW current signal comparable to the noise level.

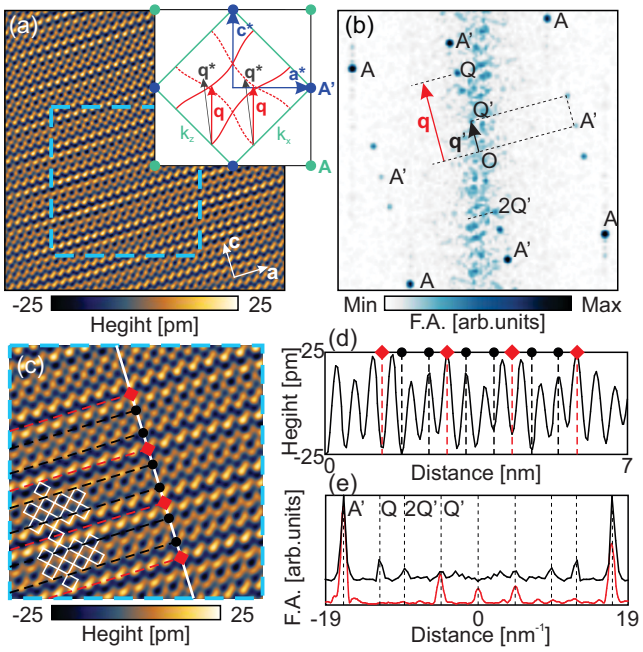

Figure 3.2: (a) Flittered STM topography obtained for $V_b = 0.2\,\mathrm{V}$ and $I_s = 0.6\,\mathrm{nA}$. The inset shows a sketch of the Fermi surface within the first Brillouin zone (green square whose nodes are A$'$ points) corresponding to an isolated Te sheet. The dashed (red) lines correspond to the p_x portion of the Fermi surface, whilst the solid (red) lines correspond to the p_z portion of the Fermi surface. The $\mathbf{q}^*$ connects one set of p_x bands. The $\mathbf{q}$ connects both the sets of p_x bands and p_z bands, and is parallel to $\mathbf{c}^*$ vector; (b) The corresponding Fourier transform. A and A$'$ peaks in the Fourier image correspond to the A and A$'$ peaks in the inset; (c) Magnified part of image in (a) showing the CDW modulation; (d) Profile along the white line in panel (c); (e) Profile along the main and side diagonals of the Fourier image in panel (b). F.A. stands for Fourier Amplitude.

In addition to Q and Q$'$, another peak, which we label as 2Q$'$, exists on the main diagonal of the Fourier image in figure 3.2 (b). It is located at $8.38\,\mathrm{nm}^{-1}$ from

the origin, which is exactly twice the distance between the origin and the Q′ peak. The wave vector connected to this peak is, thus, exactly two times larger than the $\mathbf{c}^* - \mathbf{q}$. Both Q′ and 2Q′ are, in fact, due to the wavevector mixing effect which occurs between the $\mathbf{q}$ and $\mathbf{c}^*$ [63]. However, the full mixing effect is not entirely visible in figure 3.2 (b) because the exerted noise masks the rest of the prominent mixing peaks. In figure 3.3 (a), which has been obtained by averaging 34 consecutive Fourier images, this effect becomes more clear. As it can be seen, additional peaks arise by improving the signal-to-noise ratio, both on the main and the side diagonal. Numbers 2 and 6 in figure 3.3 (a) denote two new peaks on the main diagonal specified by $2\mathbf{q} - \mathbf{c}^*$ and $2\mathbf{c}^* - \mathbf{q}$ vectors, respectively. The side diagonal has four peaks corroborating the afore mentioned effect. Their wavevectors, $\mathbf{a}^* + \mathbf{c}^* - \mathbf{q}$, $\mathbf{a}^* + 2\mathbf{q} - \mathbf{c}^*$, $\mathbf{a}^* + 2\mathbf{c}^* - 2\mathbf{q}$ and $\mathbf{a}^* + \mathbf{q}$ are shown by arrows in figure 3.3 (a). Finally, figure 3.3 (b) displays line cuts along the main and side diagonals in order to illustrate that every peak on the main diagonal, except A′+Q′ and 2A′, has its "copy" on the side diagonal.

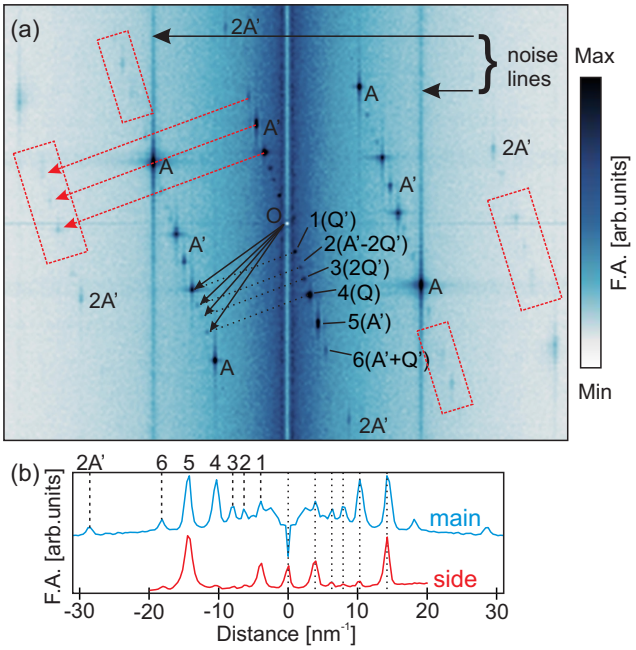

Figure 3.3: (a) Averaged Fourier transform obtained by summing 34 Fourier transforms which are similar to the one shown in figure 3.1 (b); (b) Profile along the main and side diagonals. Red rectangles mark the areas within which are the Fourier peaks representing copies of the lattice and modulation peaks in higher Brillouin zones. F.A. stands for Fourier Amplitude.

As noted before, Te sheets are unstable and prone to the CDW. The superspace crystallographic analysis done in Ref. [53] indicated that the distances between neighboring Te atoms in the planar sheets vary around the average of 0.3035 nm in a systematic manner. The total ordering can be viewed as alternate sequences of V and N groups of Te sheet atoms in the direction of the crystallographic c axis

(along the CDW modulation). By analyzing figures 3.1 (b) and 3.1 (c) we have already noted that the interatomic distances between neighboring Te atoms vary around the average of 0.3075 nm, which is slightly higher that the one given in Ref. [53]. However, since the distance variations are rather subtle we were not able to confirm the proposed ordering by examining images similar to those in figure 3.1 (b). Therefore, we have chosen the tunneling parameters, $V_b = 0.1\,\mathrm{V}$ and $I_s = 0.7\,\mathrm{nA}$, for which the tip is even closer to the surface than in the case shown in figure 3.2 (a). In this way, the close proximity of a sharp tip to the surface atoms would result in a convolution image such that the atoms being further away from each other would be resolved better than the atoms which are closer to each other (see the sketch in the inset of figure 3.4 (a)).

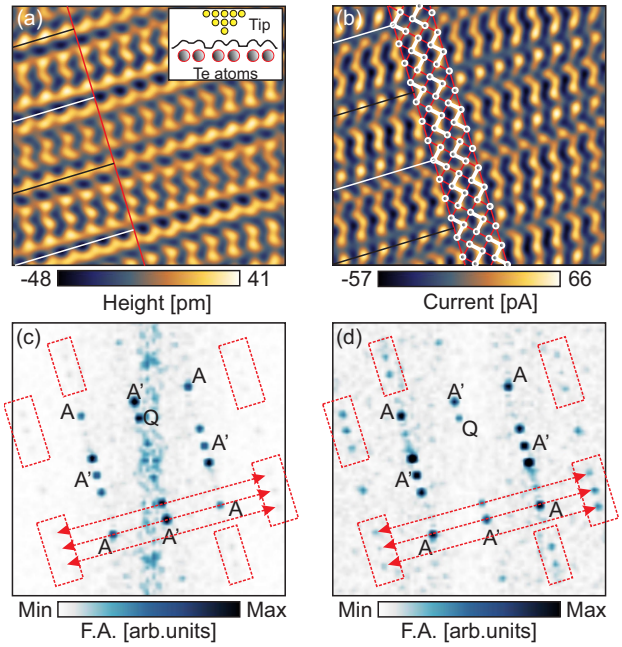

Figure 3.4: (a) Topography and (b) current images obtained for V_b=0.1 V and I_s=0.7 nA and (c), (d)their corresponding Fourier images. Red rectangles mark the areas within which are the Fourier peaks representing copies of the lattice and modulation peaks in higher Brillouin zones. F.A. stands for Fourier Amplitude.

The corresponding topography image is shown in figure 3.4 (a). Next to it (figure 3.4 (b)) is an image formed by measuring the changes of the tunneling current (with respect to I_s) before the feedback moves the piezo scanner in order to maintain the predefined current setpoint. Below them, in figures 3.4 (c) and 3.4 (d), shown are the corresponding Fourier images.

The topography image in figures 3.4 (a) clearly displays the CDW modulation stripes, as expected, with strange looking shapes in between the stripes. On the other hand, the current image in figures 3.4 (b) displays N and V groups of Te sheet atoms, indicated by higher current values, which have a repeating pattern matching

the CDW modulation stripes in figures 3.4 (a). The observed patterns in both topography and current images may originate from the convolution of a damaged (not very sharp) tip and the surface or they may represent a local modification of the surface. That being the case, one would expect to observe new peaks in the Fourier images at the positions defined by wavevectors which are not represented as linear combinations of the lattice and the modulation wavevectors. However, the corresponding Fourier images in figures 3.4 (c) and 3.4 (d) have almost all of the characteristic peaks seen in figure 3.2 (b), i.e. A, A′, Q and the copy of Q′ on the side diagonals, without any new features. The absence of the Q′ and 2Q′ peaks from the main diagonals in figures 3.4 (c) and 3.4 (d) is a consequence of applying Fourier transform to the images scanned over a small area and, of course, a consequence of low signal-to-noise ratio, rather than a consequence of the modification of the carrier density modulation. It is, therefore, natural to assume that only carrier density modulation, lattice features and, as explained, their interplay have an impact on the formation of the image in figures 3.4 (a) and 3.4 (b), and that the effect of the convolution of the surface with a "bad" tip can be ruled out.

Having in mind that the Fourier images in figures 3.4 (c) and 3.4 (d) have the same periodic components, one can conjecture that different motifs observed in the topography and current images originate from the different intensities of the Fourier peaks. In fact, the strong CDW stripe motif in the topography image is due to the fact that the Q peaks in figure 3.4 (c) have higher intensity than the A peaks. Oppositely, the current image does not have strong CDW stripe motif because the Q peaks have significantly lower intensity than the rest of the peaks in figure 3.4 (d). On the other hand, the irregular shapes in figure 3.4 (a) and the N and V shapes in figure 3.4 (b) are mainly determined by the intensity of the copies of the Q′ peak on the side diagonals, A and A′ peaks.

The "modulation" features on the side diagonals of the Fourier images may exist due to both carrier density modulation and structural modulation (rearrangement) of the Te sheet atoms. If we were to assume that there is no structural modulation, than the intensity of the aforementioned peaks would be determined by the strength of the tunneling signal from the carrier density modulation components with the corresponding periodicity. If the structural modulation is considered without the carrier density modulation, than the intensity of the related peaks would be determined by the magnitude of the atom displacements. Larger displacements would yield Fourier peaks with high intensity, but would also introduce asymmetry in the intensity of the "modulation" peaks across the side diagonal. Such asymmetry is seen as unequal intensity of the Q′ copies on the side diagonals in figures 3.4 (c) and 3.4 (d). Similar asymmetry of the intensities of the Q′ copies on the side diagonals can be observed in figure 3.2 (b). The Q′ peak copies in figure 3.2 (b) are,

however, weaker in comparison to A and Q peaks, which is why the corresponding topography looks like a square Te lattice to which the carrier density modulation and its components are added. Therefore, the structural modulation seen in figure 3.4 (b) most probably exists also in figures 3.2 (b) and 3.4 (a) but it is masked by contribution of the other periodic components included in the formation on these images.

Finally, further examination of Fourier images in figures 3.3 (a), 3.4 (c) and 3.4 (d) indicates the existence of additional peaks (marked by red rectangles in the mentioned figures) which are located at the positions corresponding to the linear combinations of the lattice and the modulation wavevectors. These peaks are, therefore, copies of the lattice and modulation peaks in higher Brillouin zones, and are expected in systems exhibiting charge density and structural modulations. However, their intensity is very low, especially in figures 3.3 (a) and 3.4 (c), and comparable to the noise level. Unfortunately, we find that taking larger scans than those shown in figures 3.4 (a) and 3.4 (b) does not improve signal-to-noise ratio for the additional peaks at room temperature, but rather leads to an unstable operation in which the topography and the current images change their appearance after a certain time of scanning.

3.2.2 CDW gap measurement

3.2.2.1 STS measurements

The formation of energy gaps is a general characteristic of the CDW systems. In these systems a broken symmetry ground state (CDW state) is stabilized via electron-electron or electron-phonon interactions or both, by creating electron-hole pairs with the ordering vector selected as explained in Section 3.2.1. This, in turn, leads to the energy gap formation in the regions of the Fermi surface connected by the preselected ordering vector, thus, lowering the energy of the system. For $R\mathrm{Te}_3$ family the Fermi surface is only partially gapped. Here we use STS in order to assess the CDW gap of CeTe_3 at room temperature.

Figure 3.5 shows an averaged dI/dV versus V(red curve) and its first derivative, d^2I/dV^2 (blue curve). In the upper inset shown are the $I-V$ curves collected at different locations on the sample by performing ten consecutive measurements at each location. The averaging procedure was done due to the variation of the $I-V$ curves which are acquired at random points, including ones above and in between the Te sheet atoms. Location dependent variations of the $I-V$ were previously noted in TbTe_3 [63]. The spatial variation of the $I-V$ curves is consequently reflected on the corresponding dI/dV curves in terms of occasional appearance of different peak-like features and variations of the conductance near the edges of the

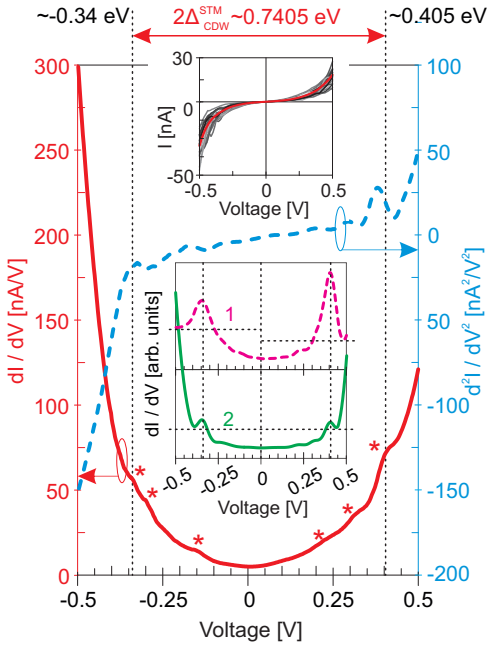

Figure 3.5: Averaged dI/dV curve obtained by repeated measurements at different positions on the sample and its first derivative. The red asterisks indicate the kinks. The upper inset shows all $I-V$ curves taken into account. The lower inset shows two dI/dV curves obtained by averaging selected dI/dV curves.

measuring range.

The asymmetry of the averaged dI/dV curve, is an inherent property of most of the individual dI/dV curves, despite their location dependent variations. It originates from the fact that, apart from the in-plane p_x and p_z orbitals, the p_y orbitals are probed as well [63]. Removal of electrons from p_y, which occurs at negative voltages, is more favorable than the adding of electrons at positive voltages since the p_y orbitals are below the Fermi level. Therefore, the conductance, i.e. dI/dV, will be higher for negative than for positive voltages and, consequently, the dI/dV curves would be asymmetric. This type of dI/dV asymmetry is common among systems exhibiting CDW [62; 63; 64; 65; 66].

The averaged dI/dV exhibits subtle kinks marked by (red) stars in figure 3.5. For each kink in the dI/dV curve one can observe a change in slope of the corresponding d^2I/dV^2 curve which, indeed, corroborates that the kinks exist. In fact, most of the kinks are a consequence of the location dependent variations of the individual dI/dV curves included in the averaging procedure. They are, therefore, likely due to involvement of the tip states, due some other effect such as zero bias anomaly [67], or even maybe due to the existence of the shadow gaps in $CeTe_3$ [68]. Similar structures can be observed in Ref. [62]. Unfortunately, we cannot claim with certainty what they represent nor determine their origin. Exceptions are the two features at $\sim -0.34\,\mathrm{eV}$ and $\sim 0.405\,\mathrm{eV}$, additionally marked by dashed lines, which exist in the

most of the measurements. Majority of the individual dI/dV curves exhibit weak features at $\sim -0.34\,\mathrm{eV}$ and $\sim 0.405\,\mathrm{eV}$, whereas a notably smaller number of curves has slightly stronger features at the same energies (the reason why the intensity of these peaks vary is unknown). Hence, the average dI/dV in figure 3.5 also has weak structures at $\sim -0.34\,\mathrm{eV}$ and $\sim 0.405\,\mathrm{eV}$. A sharp rise of the conductance occurring immediately below $\sim -0.34\,\mathrm{eV}$ and above $\sim 0.405\,\mathrm{eV}$ in the average dI/dV indicates that these features may be interpreted as the edges of the CDW gap [67]. However, the density of states within the suggested gap does not appear to be suppressed. This is somewhat expected considering that a large number of curves, having a significant location dependent variation, are averaged. On the other hand, averaging a smaller number of selected curves yields dI/dV spectra with clear features at $\sim -0.34\,\mathrm{eV}$ and $\sim 0.405\,\mathrm{eV}$ and a suppressed density of states between them, as shown in the lower inset of figure 3.5. dI/dV labeled by 1 is obtained by averaging curves with stronger features, whereas dI/dV labeled by 2 is obtained by averaging curves with weaker features at $\sim -0.34\,\mathrm{eV}$ and $\sim 0.405\,\mathrm{eV}$. We, therefore, speculate that the relevant features might be the band edges rising above and below the Fermi level, which correspond to the CDW gap originating from hybridization between the original and shadow bands. We assess the distance between the two features to be $2\Delta_{\mathrm{CDW}} \sim 0.74\,\mathrm{eV}$, yielding a CDW gap of $\sim 0.37\,\mathrm{eV}$. Finally, suppressed density of states, seen in the two curves, along with the fact that both of them have a finite conductance at zero bias suggests a partially gapped Fermi surface, as expected.

3.2.2.2 Raman scattering measurements

Polarized Raman spectra of $CeTe_3$ were measured on a cleaved (010) $(a-c)$ plane in the temperature range between 348 and 32 K. Figure 3.6 shows the symmetry-resolved spectra for 348 and 32 K which are linear combinations of the raw data. For unknown reasons, the spectra taken at 348 K are generally higher by a factor close to 2 and are therefore multiplied by 0.55 to make them match those at 32 K at high and low energies. The electronic continua of the multiplied spectra match now also in the range up to $1000\,\mathrm{cm}^{-1}$. Phonons and amplitude modes appear at energies Below $400\,\mathrm{cm}^{-1}$ [69]. In addition, there are also features from crystal-field excitations which appear not only in the Raman active A_{1g}, B_{1g} and B_{2g} symmetries but also in A_{2g} symmetry, clearly ruling out a phononic origin. They originate in the energy splitting of the $2F_{7/2}$ state of $CeTe_3$ ($4f$ orbitals) in the spectral region below 400 cm^{-1} and between 2000 and 2500 cm^{-1}.

Although T_{CDW} is considerably above room temperature (and is not determined yet but believed to be in the 500 to 600 K range) one observes clear changes in the electronic spectra upon cooling. Below 4000-5000 cm^{-1} the opening of a gap manifests itself by a relative reduction of the scattering intensity in the A_{1g}, B_{1g},

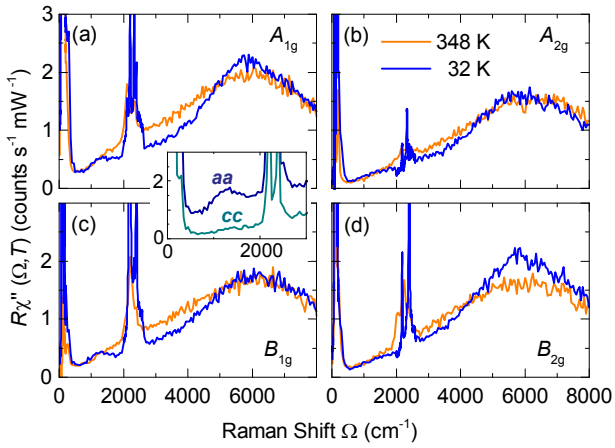

Figure 3.6: Symmetry-resolved Raman spectra of $CeTe_3$ at temperatures as indicated. The excitations in the range 2000 to 2500 cm^{-1} originate in transitions in the $F_{7/2}$ manifold. They are expected and appear also in A_{2g} symmetry. In all cases there are stronger at low temperature. Gap-like features are predominantly seen in A_{1g}, B_{1g}, and B_{2g} symmetry. The inset in (a) compares the raw data in aa and cc polarization indicating an $a-c$ anisotropy.

and B_{2g} spectra. Around 6000 cm^{-1} the intensity piles up due to emerging coherence effects in the ordered state (figure 3.6 (a), (c), (d)). As expected for electronic excitations these temperature-dependent changes are very weak or absent in A_{2g} symmetry (figure 3.6 (b)). According to the semi-quantitative analysis of the results in $ErTe_3$ [13] we interpret the changes described above in terms of an anisotropic CDW gap. The signatures of the gap are weaker than in $ErTe_3$ for two reasons: (i) Even at 348 K $\approx 0.5\,T_{\mathrm{CDW}}$ $CeTe_3$ is already deep in the ordered state, and the gap is almost constant. (ii) $CeTe_3$ has an impurity concentration comparable to that of $LaTe_3$ or $DyTe_3$ well above that of $ErTe_3$, and sharp structures are washed out [70]. Hence the A_{1g}, B_{1g}, and B_{2g} spectra reflect the CDW gap in the electronic excitation spectrum and the maximum at 5880 cm^{-1} = 0.73 eV is close to the maximal gap $2\Delta_{\mathrm{CDW}}$. This energy is excellent agreement with the gap in ARPES experiments [71] and the weak anomalies in the dI/dV curves (see figure 3.5) allowing us to associate them with the gap. Since the gap depends strongly on momentum [71] no pronounced features can be expected in angle integrated experiments such as STS at temperatures on the order of $0.5\,T_{\mathrm{CDW}}$.

Unexpectedly, we observe also an additional maximum in the range in the range 800-1700 cm^{-1} peaking around 1200 cm^{-1} $\sim$ 0.15 eV in A_{1g} and B_{1g} which appears only below approximately 200 K. The appearance in A_{1g} and B_{1g} indicates that the maximum belongs to the lower symmetry of the ordered CDW phase. The comparison of the spectra measured with parallel polarizations along the crystallographic a and c axes (see inset of figure 3.6 (a)) shows that the crystal is mono-domain in the region of the laser spot. The selection rules are exactly those observed before in

$ErTe_3$ [13]. However there is no indication of a second CDW in other experiments (see, e.g., Ref. [71]). In addition, there is no direct correspondence to features in the STS results (see asterisks in figure 3.5) in that the energy observed by light scattering is approximately a factor of two smaller than expected from tunneling. This energy mismatch argues against an relation between the STM feature at -0.15 eV and the Raman peak at the same energy. Speculatively one may associate the second maximum found in the *aa*-polarized Raman spectra with a hidden transition having a marginally different ordering wave vector and a slightly lower minimum of the free energy as suggested in Refs. [72; 73]. However, the selection rules are more indicative of an ordering wave vector orthogonal to the first one (see gapped *cc* spectrum *versus* peaked *aa* spectrum in the inset of figure 3.6 (a)) and argue otherwise. Hence, the maximum at 1200 cm^{-1} cannot finally be explained.

3.3 Conclusion

Scanning tunneling microscopy and spectroscopy were used for an investigation of the CDW state in $CeTe_3$. The data was acquired at room temperature. Using Raman spectroscopy we confirmed that $CeTe_3$ is in the CDW state at room temperature. The STM topography images clearly show the presence of the CDW modulation. This fact is supported by spectroscopy curves, which indicate that CDW band gap has a value of ~ 0.37 eV and are in good agrement with gap value of ~ 0.365 eV obtained from Raman measurements. The analysis of the Fourier transform images showed two main peaks along the direction of the CDW. One representing the dominant CDW modulation wavevector, located at $|\mathbf{q}| = 10.26\,nm^{-1}$, and the other one, $|\mathbf{c}^* - \mathbf{q}| = 4.19\,nm^{-1}$, interpreted as a consequence of the wavevector mixing effect. The other peaks, which are not related to the Te sheet atoms and Ce subsurface atoms are related both to the mixing effect and possible structural modulations of the Te sheet atoms. The current images indicate periodic patterns of Te sheet atoms grouped in N and V shapes, which were not previously observed by STM.

Chapter 4 Kelvin probe force microscopy and applications of two-dimensional charge carriers in graphene

Graphene has already found its way into a number of applications ranging from composite materials to optoelectronics due to its remarkable properties [20; 22; 30; 31]. For example, the tunability of graphene's optical conductance is the key property utilized in optoelectronics [24]. However, these applications are each at different levels of maturity and the scientific community is still struggling to overcome various technological challenges impeding further improvement of graphene based devices [29].

In this chapter we study the electrical gating of graphene in the so-called back-gate configuration by means of which optical conductance of graphene can be tuned. In particular, we analyze the influence of a thin protective oxide layer on the performance of a back-gate graphene device, by combination of atomic force microscopy (AFM), electrostatic force microscopy (EFM) and Kelvin probe force microscopy (KPFM). Then we focus on the investigation of graphene-waveguide coupled system, a platform used for various optoelectronic devices, and discuss its application in electro-optical modulators.

4.1 Materials and Methods

4.1.1 Sample Fabrication and Experimental Methods

Thin layers of graphite (i.e. few-layer graphene) and graphene were prepared by micromechanical exfoliation of the natural graphite. Briefly, thick graphite crystals are exfoliated by a sticky tape until very thin graphitic layers are produced. These layers are then transferred on the clean surface of either 90 nm or 290 nm thick SiO_2 which is supported by a thick (bulk) Si crystal. The transfer procedure includes the following steps: (i) applying the tape carrying thin graphitic layers over the clean substrate and (ii) removal of the tape's adhesive using methyl-isobutyl ketone. After the transfer is done, the thin graphitic layers are thinned further by means of a few additional exfoliation steps. A clean sticky tape is applied directly over the

substrate supporting the thin graphitic layers and then removed. This is done until the monolayer is reached. Figure 4.1 shows a few samples exfoliated on SiO_2/Si substrates.

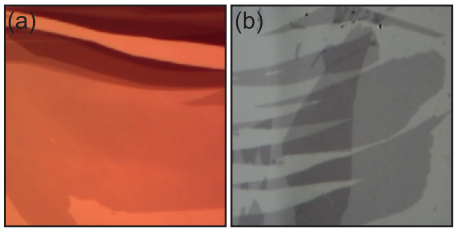

Figure 4.1: Optical microscopy images of graphene and few-layer graphene flakes made by micromechanical exfoliation on SiO_2/Si substrate having (a) 290 nm and (b) 90 nm thick SiO_2.

Graphene absorbs 2.3% of the incident (visible) light, which is a quite remarkable feature given its mono-atomic thickness [74]. This, however, is not enough for graphene to be observed under an optical microscope on an arbitrary substrate. An effective way of enhancing the visibility of graphene is to improve its contrast with respect to the substrate. For that purpose one needs a substrate which acts as a kind of a Fabri-Perot resonator for the incident (visible) light, such as the mentioned SiO_2/Si substrates. The thin SiO_2 layer provides for constructive/destructive interference of the light, and its thickness determines which of the wavelengths would interfere constructively/destructively. The best contrast is attainable when the SiO_2 layer is either $\sim$90 nm or $\sim$290 nm thick[75].

Thin Au electrodes ($\sim$20-30 nm) were fabricated on top of the exfoliated graphene samples by a standard UV lithography method. In short, this method includes the following steps: (i) deposition of the photo-resist on top of the entire sample usually by means of spin-coating, (ii) selective exposition of deposited photo-resist to ultraviolet light, via lithography mask held in between the resist and the UV source, (iii) removal of the exposed (in case of positive photo-resist) or concealed (in case of the negative photo-resist) parts of the photo-resist in a developing solution, also called the developer (iv) deposition of the Au, by any of the available deposition techniques, such as chemical vapor deposition (CVD) and (v) removal of the reminder of the photo-resist, also called the lift-off. Additionally, some of the samples were isolated by 1 nm thin Al_2O_3, which was applied over the entire surface by the atomic layer deposition.

Upon fabrication, the samples were studied by the AFM and Raman techniques. The AFM measurements were performed using standard Si_3N_4 tips in ambient condition at room temperature. Typical curvature radius of the tip was about 10 nm. The so-called tapping mode is used. In this AC AFM mode the lateral force between the tip and the sample is minimized in order to protect both sample and the

tip. The cantilever-tip system is oscillated at the characteristic first order resonance which is usually in the 90-230 kHz range. Additionally, precise HOPG inter-layer distance measurements were performed in ultra-high vacuum conditions (UHV, the pressure in the chamber is below 10^9 mbar) by operating the AFM in contact mode. The typical normal force set points ranged between a couple of hundreds of pN to a few nN, depending on the sample height and the required resolution. The ambient AFM measurements were done using the NTMDT NTegra instrument, while the UHV measurements were done using the Omicron VT-SPM system. Raman spectroscopy was performed using the NTMDT NTegra spectra, also at room temperature in ambient conditions. A linearly polarized semiconductor laser operating at a wavelength of 532 nm was used as the excitation source. The absorbed laser power was varied from 2 to 0.2 mW within the 1 x 1 μm sized focus, depending on the sensitivity of the sample.

The KPFM (EFM) studies techniques were done in the ambient conditions at room temperature. The TiN coated Si_3N_4 tips, having a typical curvature radius of about 35 nm, were used for both the topography and KPFM measurements. The DC voltages, (applied between the tip and the sample) used for the EFM measurements ranged between -8 and 8 V. Both KPFM and EFM measurements were performed for lift-heights of 30 nm.

4.1.2 Numerical Methods

For calculating the eigenmode propagation constants and fields, through which the graphene-waveguide coupling strength is defined, two numerical methods are used: (i) the reflection pole method utilized for 1D waveguide geometries and implemented within Matlab software package and (ii) the finite element method utilized for 2D waveguide geometries and implemented within Comsol software package.

Graphene is represented by an infinitely thin layer having a frequency dependent surface conductivity $\sigma(\omega)$. The simplest and most widely used model [76] for $\sigma(\omega)$ follows from the Kubo formalism in the non-interacting picture [77] in which $\sigma(\omega)$ is written as the sum of the interband and intraband conductivity. They are given by

$$\sigma(\omega)_{\text{inter}} \approx \frac{\mathrm{iq}^2}{4\pi\hbar}\ln\left(\frac{2E_{\mathrm{F}} - \hbar(\omega + \mathrm{i}/\tau)}{2E_{\mathrm{F}} + \hbar(\omega + \mathrm{i}/\tau)}\right), \tag{4.1}$$

$$\sigma(\omega)_{\text{intra}} = \frac{\mathrm{iq}^2\mathrm{k_B}T}{\pi\hbar^2(\omega + \mathrm{i}/\tau)} \times \left[\frac{E_{\mathrm{F}}}{\mathrm{k_B}T} + 2\ln\left(\exp\left(\frac{-E_{\mathrm{F}}}{\mathrm{k_B}T}\right) + 1\right)\right]. \tag{4.2}$$

Here τ and T denote the electron relaxation rate and the temperature, while q is the elementary charge. The above model accounts for the main properties of

graphene's linear optical response and its dependence on E_{F}, including the Drude-like behavior at frequencies below $\hbar\omega = 2E_{\mathrm{F}}$ (intraband transitions) and the flat absorption spectrum at frequencies above $\hbar\omega = 2E_{\mathrm{F}}$ (interband transitions).

We note here that the conducting sheet model of graphene employed in our calculations is equivalent to an anisotropic thin film model [78] in which graphene is represented as a thin film of thickness $d_{\mathrm{g}} \approx 0.34\,\mathrm{nm}$ and relative permittivity components

$$\varepsilon_{\parallel}(\omega) = 1 + \frac{i\sigma(\omega)}{d_{\mathrm{g}}\omega\varepsilon_0}, \quad \varepsilon_{\perp} = \varepsilon_{\mathrm{b}}, \tag{4.3}$$

that differ for dielectric response parallel ($\varepsilon_{\parallel}(\omega)$) and perpendicular ($\varepsilon_{\perp}$) to the graphene layer. Here ε_{b} denotes the background permittivity (in our case equal to unity for air) indicating that graphene carriers cannot respond to the electric field component $\mathbf{E}_{\perp}$ perpendicular to the sheet. The equivalence between the conducting sheet and thin film model is a simple consequence of the fact that all involved wavelengths are several orders of magnitude longer than d_{g}. Modeling graphene by the use of isotropic values for its permittivity $\varepsilon(\omega) = \varepsilon_{\parallel}(\omega)$ can lead to erroneous results in cases where $\mathbf{E}_{\perp}$ is not negligible. This is particularly important at frequencies such that $\varepsilon(\omega) \approx 0$ (the bulk plasma frequency of the hypothetical medium), for which the isotropic model predicts a spurious enhancement of $\mathbf{E}_{\perp}$ within the fictitious thin film, by means of a mechanism akin to the one used in reducing the mode volume in dielectric optical microcavities [79]. This can further lead to large spurious graphene absorption rates, as evidenced by some of the unrealistically high values reported in the literature.

The graphene-wave guide coupling strength G is evaluated numerically using

$$G(\omega) \approx \frac{|\mathbf{E}_{\parallel}|^2}{4v_g U}, \tag{4.4}$$

in 1D case and,

$$G(\omega) \approx \frac{1}{4v_{\mathrm{g}}(\omega)U(\omega)} \int_{\mathrm{graph}} |\mathbf{E}_{\parallel}|^2 \mathrm{d}l, \tag{4.5}$$

in 2D case. Here, $U(\omega)$ and $v_{\mathrm{g}}(\omega)$ denote the bare modal energy and group velocity, respectively. $\mathbf{E}_{\parallel}$ represents the electric field component parallel to the graphene sheet. It should be noted that evaluation of equation 4.4 is done at the spatial coordinate where graphene is positioned. For example, if the geometry in figure 4.20 is considered than the evaluation is done at $x = h$.

4.2 Results and Discussion

4.2.1 Atomic Force Microscopy Study of Graphene and Its Thickness

To prepare the ground for the upcoming discussion, focused on graphene devices in the so-called back gate configuration, in this section we examine the quality and evaluate the thickness of the exfoliated graphene (few layer graphene) samples by the AFM. In particular, false identification of graphene flakes on the SiO_2/Si substrate could lead to erroneous results in the latter EFM and KPFM measurements.

Prior to the thickness evaluation of the exfoliated graphene (few layer) samples, the thickness of graphene was evaluated by measuring the inter-layer distance between adjacent graphene sheets within the highly oriented pyrolytic graphite (HOPG) in UHV conditions. Meanwhile, AFM operated in contact mode is used in this case due to its high sensitivity and superb resolution, as evidenced by measurements shown in figure 4.2. In particular, figure 4.2 shows atomically resolved raw images of the topography, normal and lateral force (existing between the tip and the sample). From panels (b) and (c) one can clearly see that the actual values of the normal and lateral force are of the order of tens of pN. Furthermore, the atomic resolution image in panel (a) demonstrates that the height measurements can be done with an accuracy below an angstrom.

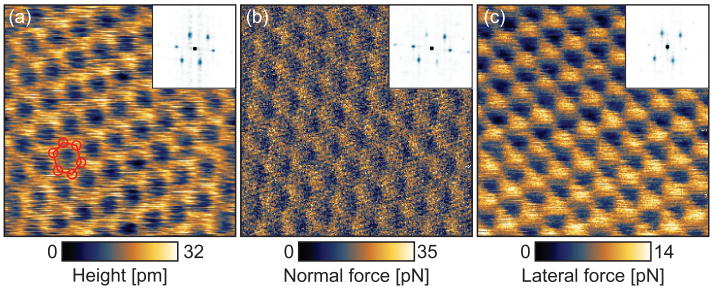

Figure 4.2: Demonstration of the atomic resolution acquired by the atomic force microscope in ultra-high vacuum conditions at room temperature. (a) Topography, (b) normal force and (c) lateral force images obtained on one of the HOPG terraces. Shown are raw images, without any kind of filtering. The honeycomb lattice is distorted due to the thermal drift of the system. The Fourier maps, shown in the insets, corroborate the fact that the periodic patterns seen in the corresponding raw images do indeed originate from the periodical arrangement of the carbon atoms in the honeycomb lattice.

That being said, we proceed further with the evaluation of the height difference between the HOPG inter-layer steps which are visible in the wider area topographs such as the one shown in figure 4.3 (a). The steps of different height are easily distinguished by a well defined gray (blue color) scale contrast levels in the topo-

graph. The height difference between the two adjacent steps was evaluated from histograms of an area containing both of the steps, as a peak-to-peak distance. This is illustrated in figure 4.3 (b). By analysing various AFM topographs, we find the step-height between two atomically thin layers within the HOPG to be 0.354 ($\pm$0.07) nm. A slightly lower value of about 0.34 nm is commonly accepted as the thickness of graphene, d_g, in the literature [20]. In addition, we find that the larger step-heights correspond quite well to the $N \times 0.354$ nm [see the profiles drawn in figure 4.3], where $N = 1, 2...$ and $N \times d_g$ is the thickness of N-layer graphene.

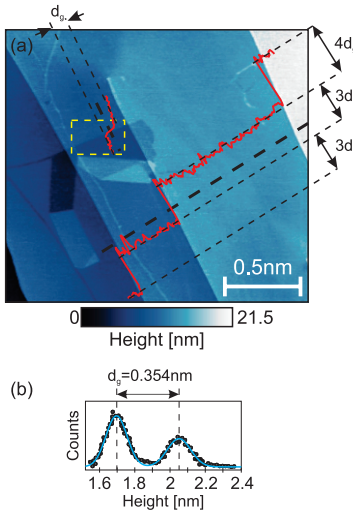

Figure 4.3: (a) Atomic force microscopy topograph of HOPG. The profiles shown within the topograph are taken along the dashed lines. (b) Histogram of an area marked by the dotted square in panel (a).

In contrast to the highly accurate UHV measurements, the ambient measurements performed in the tapping mode reveal that the thickness of thin graphite and graphene samples cannot be determined unambiguously. For example, the topography in figure 4.4(a) shows a graphene sample with an overestimated thickness of $\sim$1.2 nm (as corroborated by the corresponding Raman measurements which will be shown and discussed later).

The difference between the substrate and graphene levels seen in topography profile in figure 4.4(c) indicates that the thickness of this sample is almost 4 times the afore measured value of 0.354 nm. Similarly, the thickness of the other few-layer graphene (up to N =6 layers) samples deviates from the expected $N \times d_g$ values, as it can be seen in figure 4.5. The deviations observed when the thickness of the sample is measured with respect to the SiO_2 substrate (the largest being about $\sim$ 1.1 nm) are larger than the deviations observed when the thickness is assessed from the overlapping regions of the sample (the largest being about $\sim$ 0.3 nm), similarly as in case of the HOPG in figure 4.3(a). In fact, our results are in agreement with the more elaborate analysis provided in Ref. [80], where the authors argue that

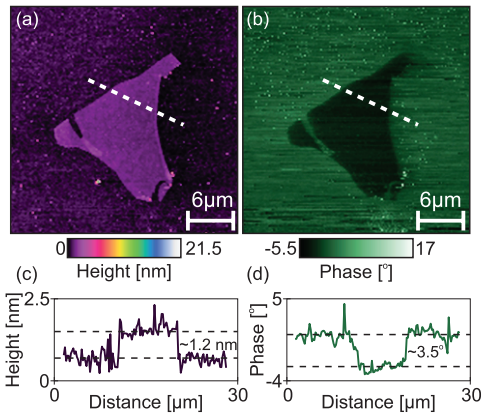

Figure 4.4: (a) Atomic force microscopy (tapping mode) topograph and (b) phase image of the selected graphene sample. (c) Topography and (d) phase profiles taken along the white dotted lines in panels (a) and (b).

the uncertainty in the thickness measurements depends on the regime in which the tapping mode is operated.

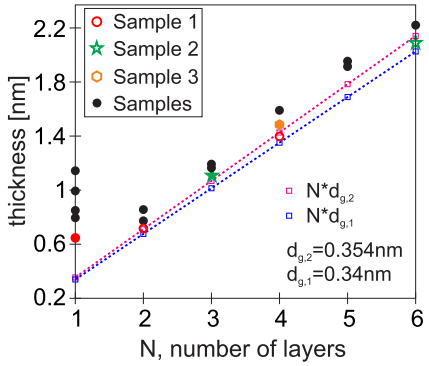

Figure 4.5: Thickness versus number of layers. Blue square markers represent $N \times d_g = N \times 0.34$ nm, whereas pink square markers represent $N \times d_g = N \times 0.354$ nm measured by the AFM in UHV conditions. The reminder of the markers represent thickness values obtained from exfoliated samples in ambient conditions. Full markers represent thickness values estimated at the sample/substrate edges, whereas hollow markers represent thickness values estimated from the overlapping regions of the sample. Specially labeled are three samples used in the latter KPFM study.

For a reliable estimation of how many layers a particular sample has, the tapping AFM measurements have to be complemented by an additional measurement technique capable of assessing the sample's number of layers, such as the Raman spectroscopy. There are many different ways in which one can assess the number of layers of a thin graphite sample by using Raman spectroscopy [81; 82]. However, these methods are reliable for samples having up to N =5-6 layers. Nevertheless, distinguishing graphene from the thicker samples is relatively simple. Namely, the 2D band of graphene has a simple spectral shape which can be fitted by a single Lorentzian line, whereas the thicker samples have a more complicated 2D band pro-

files usually fitted by two or more Lorentzians [83]. As an example, figure 4.6 shows the Raman spectra of graphene (acquired at the sample in figure 4.4(a)) and of three-layer graphene (acquired at another sample).

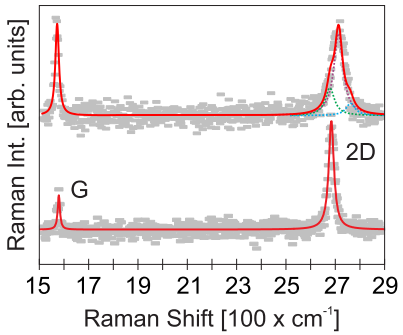

Figure 4.6: Raman spectra of graphene (lower curve) and three-layer graphene (upper curve). The measured data is shown by gray markers whereas the fit is plotted with red lines. Also shown are, in different colors, three Lorentzians used for fitting the 2D peak of the upper spectrum.

Having established the way in which one can reliably distinguish graphene from few-layer graphene, we proceed further by examining the topography of samples produced by micromechanical exfoliation of graphite. Despite being unreliable for counting the number of layers, the tapping AFM turns out to be ideal for investigating topography of the potentially contaminated surfaces [84]. In fact, superb performance of AFM topography imaging was demonstrated in case of laser induced damage and periodic structures in graphene [85; 86]. Going back to figure 4.4 (a), we observe a number of relatively small topographic features distributed mainly around the flake, but also within the flake itself. These features represent fabrication residues and other contaminants gained during or after the fabrication process, as corroborated by the obvious phase contrast with respect to the substrate and graphene flake. The tapping mode phase contrast is well known for being sensitive to material properties of the investigated samples. In order to prove that the phase contrast originates for the difference in material properties and not from the sudden changes of the sample's height we plot height and phase shift profiles in figures 4.4(c) and 4.4(d). The obvious difference between the two profiles corroborates the afore conclusion. Unfortunately, like the sample from figure 4.4 (a), majority of the exfoliated samples have residues across their surface, as it can be seen from tapping AFM topographs of various graphene/few layer graphene samples in figure 4.7.

Beside the apparent fabrication residues, in panels (b), (c) and (f) of figure 4.7, irregular height changes reminiscent of scratches are also noticeable. Such changes might occur due to inability of the feedback mechanism to appropriately regulate the height of the piezo-scanner when the tip stumbles upon pronounced topographic features. However, here this is not the case as these changes are seen within areas

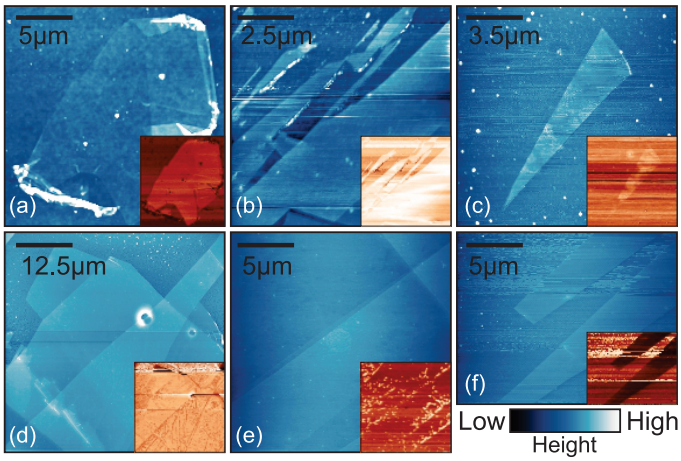

Figure 4.7: Atomic force microscopy (tapping mode) topographs of graphene/few-layer graphene samples, with the corresponding phase images shown in the insets.

without pronounced features. Similarly, phase jumps can be observed in the corresponding phase images, which are displayed in the insets. Since both the amplitude (from which the height is obtained) and the phase of the tip-cantilever oscillations depend on the dissipative tip-sample interactions [87], we suspect that these sudden changes are, in fact, due to the water or other similar adsorbates from the environment which are covering the sample's surface. In some cases, such as those shown in panels (d) and (e), the amplitude is not disturbed by the adsorbates, whereas the phase variations are so random that the whole phase image becomes corrupt. The presence of the water layer below and on top graphene was independently confirmed by the means of spectroscopic imaging ellipsometry [88]. Hence, in contrast to the clean HOPG surface [see figure 4.3], thin graphite flakes produced by exfoliation usually have their surfaces contaminated by various adsorbates and fabrication residues, well known for the ability to modify electronic and optical properties of graphene [89].

Finally, the majority of the exfoliated samples consist of segments with different thicknesses, which are occasionally mechanically deformed/wrinkled at the edges, as witnessed by figures 4.1 and 4.7.

4.2.2 Kelvin Probe Force Microscopy Study of Graphene

4.2.2.1 Introduction to Measurements of Graphene's Surface Potential by KPFM

As explained in Chapter 2, KPFM is used for accessing the potential of surfaces and it is, hence, an ideal technique for studying materials such as graphene [90]. In this introductory part we will define the necessary quantities and discuss the basic problems encountered by applying KPFM to study graphene. Therefore, let us start

with a pristine graphene sample on the SiO_2/Si substrate. If we recall, in KPFM one needs to apply an electric field between the tip and the sample in order to assess the surface potential of the sample. In the considered case, the electric field is applied between the tip and the heavily p-doped Si support, as it is illustrated in figure 4.8.

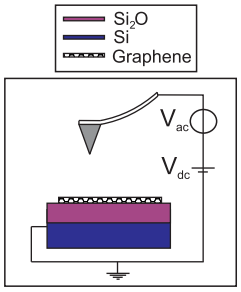

Figure 4.8: Kelvin probe microscopy scheme in case of graphene/SiO_2/Si sample.

Figure 4.9(a) shows an AFM topograph of the considered system. The triangle shaped object in the middle of the image represent graphene, whereas the surrounding area represents the SiO_2/Si substrate. The small objects residing on both graphene and the substrate are, as explained, fabrication residues. The thickness of this particular flake is overestimated, having a value of about ∼1.15 nm. Histogram in panel (c) is used for estimating the thickness of the flake. Following the conclusions reached in the previous discussion, we have performed Raman spectroscopy measurements which confirmed that the investigated flake indeed is graphene.

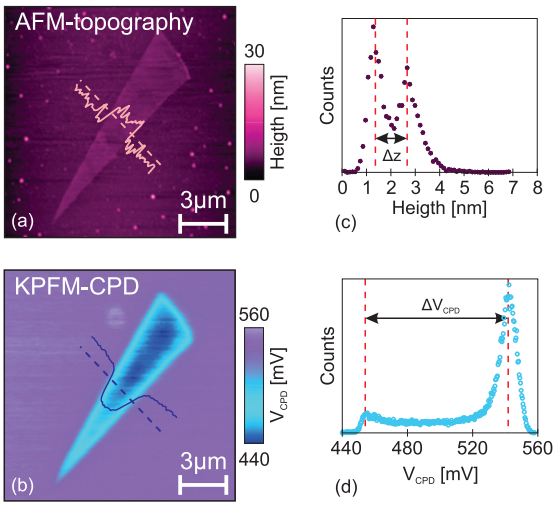

Figure 4.9: (a) Atomic force microscopy (tapping mode) topograph of graphene on SiO_2 surface. (b) The corresponding contact potential difference map. (c) Height histogram obtained from the map in panel (a). (d) Contact potential histogram obtained from the map in pane (b).

The corresponding KPFM map is shown in panel (b). Each pixel of this map represents the contact potential difference (CPD) measured between the tip and the

sample. Measured are: (i) the CPD between the tip and substrate's surface, and (ii) the CPD between the tip and graphene. In case of an insulator (dielectric), such as SiO_2, one cannot define the CPD in the manner in which it is done for metals. The reasons are the ambiguous definition of the work function in an insulator and the dominant contribution of the 'surface charges' to the CPD [91]. On the other hand, the CPD measured between the tip and graphene can be well defined, as illustrated in figure 4.10(a). Positive CPD values observed within graphene in figure 4.9(b) imply that the work function of the tip is higher than graphene's work function. However, we are unable to provide an appropriate explanation why the CPD within the substrate takes positive values, higher than those observed within graphene, due to the ambiguous origin of the substrate's CPD.

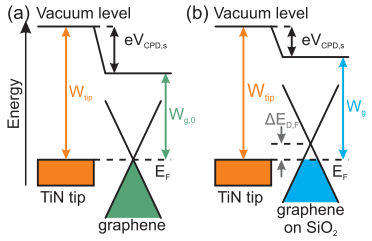

Figure 4.10: Energy diagrams showing the work functions of TiN tip, (a) intrinsic and (b) p-doped graphene. The contact potential difference is drawn for both cases from panels (a) and (b).

Graphene samples are, in most of the cases, initially doped by surface charges coming from the underlying substrate [92], various adsorbates [88] and fabrication residues [89]. The initial level of doping also depends on the type of supporting substrate [93]. Here, we do observe spatial variations of the CPD within graphene [see figure 4.9(b)] which may be caused by spatial variations of graphene's work function, thus implying unequal doping levels. Similar observations were reported by the other researchers [92]. Further examination of figure 4.9(b), reveals a bright halo originating from additional CPD variations at the flake edges. The CPD within the substrate area seems quite stable, exhibiting small spatial variations. Such behaviour is certainly unexpected given that the state of the substrate's surface can be affected by the tip during the measurements. Here, we will neglect the CPD distribution within the samples and consider only average values extracted from histograms, such as the one shown in figure 4.9(c).

The exact information about the type and level of doping of graphene is, in fact, unnecessary for completing this study. It is important, however, to recognize that initial doping exists. Henceforth, we assume the sample is initially p-doped. Consequently, the corresponding CPD should be modified to $eV_{\mathrm{CPD,g}} = W_{\mathrm{tip}} - W_{\mathrm{g}} = W_{\mathrm{tip}} - (W_{\mathrm{g,0}} + \Delta E_{\mathrm{D,F}})$, where $W_{\mathrm{g,0}}$ represents the work function of intrinsic graphene and $E_{\mathrm{D,F}} = E_{\mathrm{D}} - E_{\mathrm{F}}$. The $E_{\mathrm{D,F}}$, therefore, accounts for the initial doping originat-

ing from the SiO_2 substrate below and adsorbates(residues) above the graphene [see figure 4.10(b)]. Given the fact that spatially averaged values of CPD will be investigated throughout this work, the spatially averaged $E_{D,F}$ is deemed to have a constant value within the same sample.

The average CPD values acquired at graphene and substrate areas in figure 4.9(b) are ∼455 and ∼534 mV, respectively. This yields a CPD difference between the two areas, or the relative CPD, calculated as $\Delta V_{CPD} = V_{CPD,sub} - V_{CPD,g}$, of about ∼79 mV. Given the fact that graphene is a semimetal (with a lot of free charge carriers), such a small relative CPD indicates that graphene is unable to completely screen the electric field between the tip, representing one electrode, and the heavily p-doped Si, representing the other electrode. By conducting the same sets of experiments on other graphene samples, comprising two or more segments with different number of layers, we find that the ΔV_{CPD} increases with increasing the number of layers. The results are shown in figure 4.11.

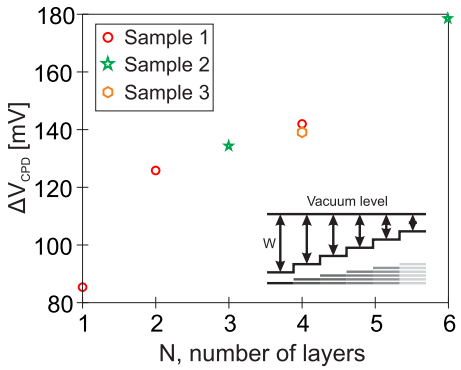

Figure 4.11: Relative contact potential difference of graphene and few-layer graphene assessed with respect to the substrate. The inset illustrates the work functions dependance on the number of graphene layers within thin graphite samples.

Comparison of ΔV_{CPD} assessed within sample segments having different thicknesses reveals that thicker samples are better at screening the applied electric field. The reason is that thicker samples simply have more charge carriers than the thinner samples. This further implies that the work function of thin graphite decreases with increasing the sample's thickness, as it is illustrated in the inset of figure 4.11.

4.2.2.2 KPFM of Graphene in Back-Gate Configuration

Now, after a brief introduction into topographical and electronic properties of the exfoliated samples, we apply the KPFM technique to explore graphene back-gate devices which are widely used for tuning the Fermi level in graphene. Figure 4.12 illustrates the experimental setup. The gate voltage, V_g, is applied between the highly p-doped Si and the gold (Au) electrode which is covering a part of graphene sample.

The Au electrode used for controlling the electric field across the graphene/SiO_2/Si capacitor is also used for defining the potential difference between the tip and the sample. For the reasons explained in the introductory part of this section, concerning the ambiguous origin of the substrate's CPD, we choose the Au electrode as a reference for assessing the ΔV_{CPD}. In addition, by using a referent material whose work function cannot be altered by the biased tip, one eliminates the omnipresent constant background signal, arising from the long-range electrostatic interactions between the cantilever and the Si electrode. The shift of the Fermi level in graphene is achieved by changing V_{G}.

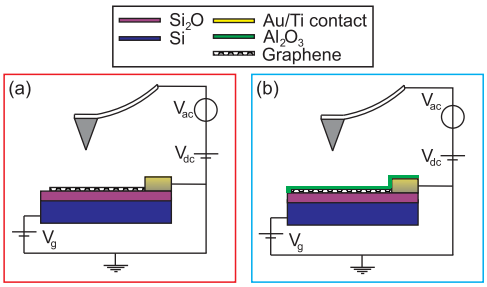

Figure 4.12: Kelvin probe microscopy schemes for (a) bare graphene/SiO_2/Si back-gate device and (b) isloated graphene/SiO_2/Si back-gate device.

Two types of samples are investigated, bare and isolated, as sketched in panels (a) and (b) of figure 4.12, respectively. The term 'bare' reflects the fact that graphene is exposed to ambient conditions, whereas the term 'isolated' means that graphene is protected by a 1 nm thin layer of Al_2O_3. In comparison to the samples investigated in Section 4.2.2.1, here, introduced are the Au electrode and the Al_2O_3 layer. Hence we shall start the analysis by examining their influence on graphene in the V_{G}=0 V case.

Zero Gate Voltage Analysis. First, the sensitivity of the tip to the graphene/electorde structure under the protective oxide layer is investigated. This is done by the EFM technique. In principle, the EFM and KPFM are quite similar, as they both exploit the electrostatic forces between the tip and the sample. However, the quantity measured in EFM is the phase shift of the cantilever-tip oscillations induced by electrostatic fores, or rather their gradient. The phase shift, ϕ, related to the square of the difference of the DC voltage, applied to the tip, and the sample's surface potential via equation 2.4. The phase shift, therefore, can simply be regulated by changing the V_{tip}. Thence, if the long range electrostatic forces are able to reach the electrode and graphene below the protective layer one should be able to observe different contrast between the two when the sign of V_{tip} is changed. This is exactly what we observe. An example is shown in figure 4.13(a). The profiles in figure 4.13(b), taken along the dashed and dotted lines in the corresponding maps,

corroborate that the phase shift contrast changes. An additional set of complementary EFM measurement which are performed on the bare and isolated samples is given in Appendix A.1.

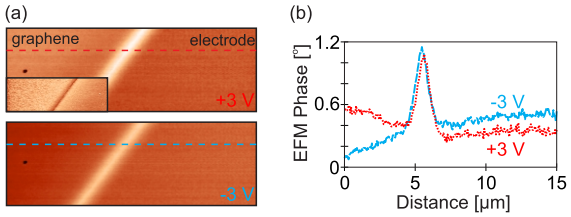

Figure 4.13: (a) Electrostatic force microscopy phase shift maps acquired by biasing the tip at +3 V (upper map) and at −3 V (lower map). The inset shows atomic force microscopy phase shift map in which there is no contrast between the Au electrode and graphene since they are both covered by the same material, Al_2O_3. (b) Profiles taken along the dotted and dashed lines in the corresponding maps.

Having proved the sample structure beneath the protective oxide layer can be probed by the EFM technique, we proceed further by analysing the KPFM results. Figure 4.14 shows two KPFM maps, one corresponding to the bare graphene [see panel (a)] and the other corresponding to the isolated graphene [see panel (b)]. The two maps are quite similar, having two easily distinguishable levels. The higher level represents the Au electrode, whereas the lower level represent graphene. The average CPD values acquired at these two samples are positive which is, as we have already noted, an indication that the tip has the highest work function. In fact, comparison of the previously reported values of the work functions of thin TiN layers (the tip is coated by thin layer of TiN), Au electrode and intrinsic graphene, which read ∼5.3 eV [94], ∼4.8 eV [95], ∼5.1 [96], are corroborative of our findings.

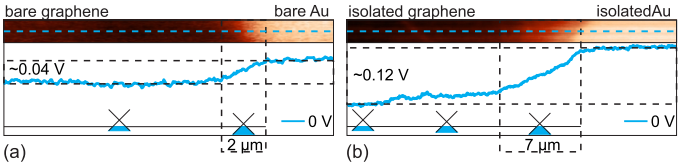

Figure 4.14: Contact potential difference maps, at V_G =0 V, for (a) bare and (b) isolated samples. The profiles below the corresponding maps are taken along the dotted lines.

Unlike the undefinable CPD in the case of SiO_2, the CPD at the Au electrode of the bare and isolated sample can be defined as $eV_{CPD,Au} = W_{tip}-(W_{Au}+\Delta W')$, where $\Delta W'$ presumably describes the contribution of the electric dipoles at Au/adsorbate interface in case of the bare sample, and the electric dipoles existing at the Au/Al_2O_3 interface in case of the isolated sample [see figure 4.15]. As a matter of fact, previous studies show that the charge state at the metal/dielectric interface has a significant role in determination of the effective work function of the metal/dielectric thin stacks

[97]. Again, one must take care of the fact that these definitions are applicable only for the spatially averaged CPD values. Graphene's CPD is expressed in the same manner as in Section 4.2.2.1 [see figure 4.10(b)], where, in case of the isolated sample, $E_{D,F}$, a representative of the initial state, accounts for additional doping due to the charges at the graphene/Al_2O_3 interface.

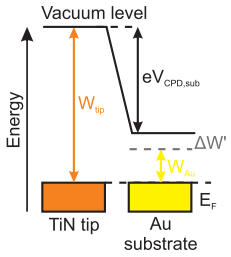

Figure 4.15: Energy diagrams showing the work functions of the Au electrode. The contact potential difference is illustrated as well.

Deposition of the Au electrode clearly leads to the modification of the CPD acquired in the vicinity of graphene/electrode area. Namely, by examining profiles, which are plotted below the corresponding KPFM maps in figure 4.14, we notice that the CPD gradually drops when crossing from the electrode area to graphene area. The crossing regions are multiple times larger than the resolution of the KPFM. Given the fact that the W_{tip}, W_{Au} and $\Delta W'$ have constant values, we conjecture that the level of doping in graphene is altered within these regions. In other words, the Au electrode modifies the position of graphene's Fermi level in its (electrode's) vicinity by providing an additional amount of charge carriers. The reason for which the isolated sample has longer crossing region than the bare sample remains unclear to us.

Non Zero Gate Voltage Analysis. We have heretofore demonstrated the ability of the KPFM technique to 'sense' the changes of the Fermi level in graphene. Therefore, in light of previous results, the changes of the Fermi level induced, now, by the gate voltage should be assessable as well. Figure 4.16 displays KPFM maps obtained for gate voltages ranging from V_G=0 V to 20 V, in steps of 4 V. Left side of the figure corresponds to the bare sample, whereas the right side of the figure corresponds to the isolated sample.

At first impression, the non-zero V_G maps appear to be similar to the map obtained for V_G=0 V. The CPD profiles shown below the maps in figure 4.16, however, provide a better insight into what happens when the V_G is tuned. Meanwhile, the profiles are intentionally displaced (the electrode CPD levels are equalized) in order to omit the background signal and present the data in a more lucid way. By analysing the profiles in figure 4.16, we find that the separation between graphene's

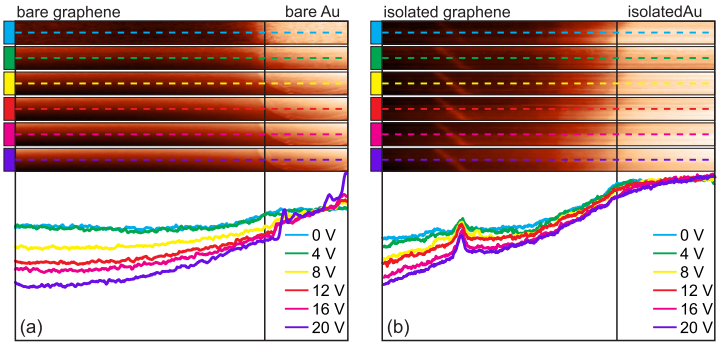

Figure 4.16: Contact potential difference maps acquired at different gate voltages. The profiles are color coded, taken along the dotted lines in the corresponding maps, and offset for clarity.

and electrode's CPD levels becomes larger when V_G is increased. Since V_G should not tamper with the electrode's surface potential (W_{Au} is constant), the apparent augmentation of the distance between the two CPD levels originates dominantly from V_G induced modification of graphene's CPD. This further implies that the work function, and, consequently, the Fermi level are changing as well. Figure 4.17 illustrates the way in which the CPD might change with V_G if an initially p-doped graphene is assumed.

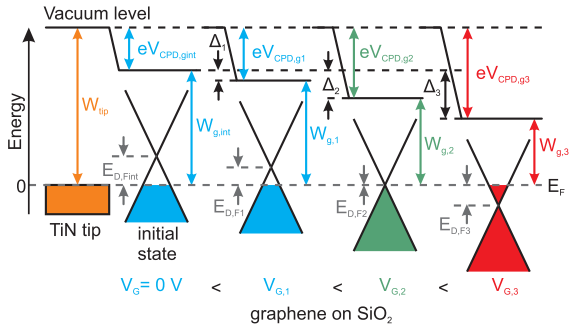

Figure 4.17: Energy diagrams depicting changes of the contact potential difference and, consequently, changes of graphene's work functions, induced by the non-zero gate voltage.

Apart from modifying the relative CPD difference, the non-zero V_G also affects the graphene-electrode crossing region [this region is defined in the previous paragraph and marked in figure 4.14] by making it slightly larger than in V_G=0 V case, as seen from profiles in figure 4.16.

In order to compare the performance of the devices from figures 4.12(a) and 4.12(b), we shall focus on the dependance of the relative CPD difference, ΔV_{CPD} on V_G. Figure 4.18 shows the ΔV_{CPD} versus V_G for both bare and isolated samples. Plotted are two curves for each of the samples, one representing forward and the other representing backward V_G sweep. We have already noted that ΔV_{CPD} increases with increasing V_G, a fact now clearly observed for both forward and backward

sweeps of the gate voltage. For example, in case of the bare sample, during the forward V_G sweep ΔV_{CPD} increases from ∼35 mV (at V_G=0 V) to ∼130 mV (at V_G=20 V), whereas, in case of the isolated sample, ΔV_{CPD} increases from ∼110 mV (at V_G=0 V) to ∼150 mV (at V_G=20 V).

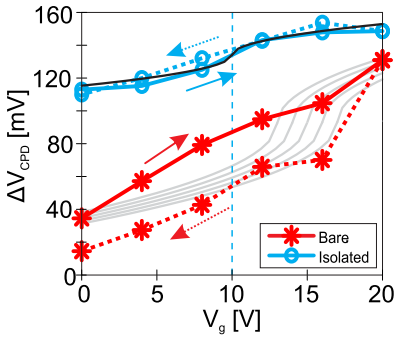

Figure 4.18: $\Delta V_{CPD}(V_G)$ versus V_G for bare and isolated samples. Solid and dotted lines with markers (circles denote isolated, stars denote bare samples) correspond to forward and backward gate sweeps, as indicated by the arrows. The solid black line represents the best fit to both forward and backward curves of the isolated sample, whereas the solid gray lines show some of the fitting attempts related to the forward and backward curves of the bare samples. The vertical dashed line indicates the V_D =10 V, a value extracted from the fit of the 'isolated' curves. Positive values of V_D = mean that the sample is initially p-doped, as it is assumed at the beginning of this chapter.

The isolated samples experience smaller change of ΔV_{CPD} within the given V_G range. For example the 'isolated' curve obtained in the forward gate sweep seems narrower that the corresponding 'bare' curve, as its ΔV_{CPD} values vary within ∼40 mV, whereas the 'bare' ΔV_{CPD} values vary within ∼ $95mV$. On the other hand, the ΔV_{CPD} curves belonging to the isolated sample are located above their 'bare' counterparts. The reasons for the outlined behaviour of the ΔV_{CPD} are found within the $\Delta V_{CPD} = V_{CPD,Au} - V_{CPD,g}$ equality. Namely, inserting the afore defined equations for the CPD of Au and graphene into ΔV_{CPD} leads to $\Delta V_{CPD} = 1/e[W_g(V_G) - W_{Au} - \Delta W']$. From figure 4.17 it follows that the work function of (initially p-doped) graphene, at $V_G \neq 0$ V, can be written as $W_g(V_G) = W_{g,int} - \Delta(V_G) = W_{g,int} - E_{D,F,int} + E_{D,F}(V_G)$, where where $E_{D,F}(V_G)$ represents the absolute shift of the Fermi level achieved for V_G, whereas $\Delta(V_G)$ represents the relative shift of the Fermi level measured with respect to $E_{D,F,int}$. Consequently, $\Delta V_{CPD} = 1/e[W_{g,int} - E_{D,F,int} + E_{D,F}(V_G) - W_{au} - \Delta W']$. Since W_{Au}, $\Delta W'$, $E_{D,F,int}$ and $W_{g,int}$ are treated as positive constants, we obtain

$$\Delta V_{CPD} = 1/e[E_{D,F}(V_G) + C], \tag{4.6}$$

where $C = W_{g,int} - E_{D,F,int} - W_{au} - \Delta W'$. From $W_{g,int} = W_{g,0} + E_{D,F,int}$ it follows

$C = W_{g,0} - W_{au} - \Delta W'$. By acknowledging that the Dirac point (charge neutrality point, CNP) of doped graphene and its Fermi level can be matched by applying $V_G = V_D$, we may rewrite the gate-voltage dependent term in equation 4.6 as [20]

$$E_{D,F}(V_G) = E_D - E_F = \pm\hbar v_F \sqrt{\pi}\sqrt{\alpha}\sqrt{|V_G - V_D|}, \tag{4.7}$$

where $\hbar$ represents the reduced Plank's constant, v_F represents the Fermi velocity in graphene and α represents a gate oxide capacitance per elementary charge (expressed in the units of $[m^{-2}V^{-1}]$) which depends on the device (Si/SiO_2/graphene capacitor) geometry. The plus(minus) sign applies when graphene is p-doped(n-doped). Inserting equation 4.7 into equation 4.6 yields

$$\Delta V_{CPD} = \pm C_2\sqrt{\alpha}\sqrt{|V_G - V_D|} + C_1, \tag{4.8}$$

with C_2 being equal to $\hbar v_F\sqrt{\pi}/e$. Evidently, $C_1 = C/e$ in equation 4.8 determines the relative position of the curves in figure 4.18 with respect to one another. In particular, $V_G = V_D$ yields the vertical $\Delta V_{CPD} = C_1$ offset value for the curves in question. Therefore, the 'isolated' curves have higher C_1 constant. In principle, the bare and isolated samples should have the same W_{Au} and $W_{g,0}$, thus, leaving the $\Delta W'$ as the main source of the difference in C_1 constant between the two samples. However, the W_{Au} is expected to depend on the thickness of Au, similarly as in other thin metal layers [98]. The thickness of the Au electrode is not equal for the bare and isolated samples and consequently W_{Au} contributes to the observed C_1 difference as much as $\Delta W'$. The geometrical factor, α, on the other hand, defines the range in which the ΔV_{CPD} will vary. Moreover, according to equation 4.7, this parameter quantifies the efficiency with which the applied gate voltage changes the Fermi level. In case of an ideal parallel plate gate-capacitor from figure 4.12 $\alpha = \epsilon_0\epsilon_{SiO_2}/d_{SiO_2}/e = 7.43 \times 10^{14}$ $m^{-2}V^{-1}$. Here, $\epsilon_{SiO_2} = 3.9$ and $d_{SiO_2} = 290$ nm represent the dielectric constant and the thickness of the SiO_2. However, the ideal value of this parameter is often degraded by parasitic capacitances across the device [99]. Hence the difference in the ΔV_{CPD} variation range between the 'bare' and 'isolated' curves. In order to determine the exact values of the afore mentioned parameters the curves in figure 4.18 are fitted using equation 4.8. Both the bare and isolated samples exhibit the same behaviour, apparently characterised by hysteresis loops. In case of isolated sample the forward and backward curves are almost identical, hence, the black solid line in figure 4.18 represents a fit for both curves. While the fitting of the 'isolated' curves was relatively easy, yielding C_1 =134 mV, $\alpha = 2.64 \times 10^{13}$ $m^{-2}V^{-1}$ and V_D = 10 V, the fitting of the 'bare' curves was practically impossible. Namely, assuming the hysteresis like behaviour, one would expect that the forward and backward curves of the bare sample could be fitted for the same set of C_1 and α parameters

and different values of V_G. However this is not the case with which we are confronted. For example, in figure 4.18 by gray lines show are curves representing some of the fitting attempts. The fitting parameters are C_1 =93 mV, $\alpha = 1.65 \times 10^{14}$ m^{-2}V^{-1} and $V_D = 13 - 17$ V. As none of the calculated curves, including the displayed ones, fit the measured data well, one cannot be certain of neither the CNP whereabouts nor about the validity of rest of the parameters. Since the C_1 and α should be constant within the same device, it seems as if the V_D slightly changes its value at each V_G, thus, yielding a corrupted hysteresis loop. Unlike the isolated sample, the bare sample is exposed to the ambient conditions and therefore able to interact with the environment. The reason for this might be that the applied gate voltage is being compensated by 'chemically' induced shift of the Fermi level in graphene through the adsorbate (water) dipoles from the environment, which are attracted to the surface by the applied electric field. Such a scenario certainly corroborates the progressive modification of V_D during the gate voltage sweeps. As a matter of fact studies similar to ours predict similar behaviour of graphene which is exposed to ambient conditions [100].

In any event, the difference between the forward and backward curves implies that the device is not working properly, as the same V_G values should not induce unequal shifts of the Fermi level. Hence, the measured ΔV_{CPD} offset, or alternatively the $\delta(E_{D,F}(V_G))$, represents a quantitative measure of the quality of considered devices. Now, let us briefly discuss the influence of $\delta(E_{D,F}(V_G))$ on a hypothetical graphene-based optical device. We will consider V_G=8 V case of the bare sample from figure 4.18. At V_G=8 V we assess ΔV_{CPD} ~80 mV and ΔV_{CPD} ~40 mV for the forward and backward swipes, respectively. By subtracting these values we get $\Delta V_{CPD,forward} - \Delta V_{CPD,backward} = 1/e[E_{D,F,forward}(V_G) - E_{D,F,backward}(V_G)] = 1/e[\delta(E_{D,F}(V_G))] = 40$ mV, which further yields $\delta(E_{D,F}(V_G)) = 0.04$ eV. Let the considered device be a waveguide in which the absorption of a guided mode, at $\hbar\omega$, is controlled by the V_G (i.e. E_F) mediated change of the real part of graphene's optical conductivity (σ_R), as shown in figure 4.19.

By applying V_G=8 V during the forward swipe we read one value of σ_R (marked by the red circle), whereas upon returning to the same gate voltage in the backward swipe we read another value of σ_R (marked by blue circle) at $\hbar\omega$. The offset between the two curves, measured with respect to $2E_F$, is in fact given by $2\delta(E_{D,F}(V_G))$, and in the considered case reads 0.08 eV. Having in mind that the absorption of a guided mode in graphene-waveguide coupled optical devices is proportional to the real part of the optical conductivity (a fact discussed in the subsequent section), one can clearly deduce that the $\delta(E_{D,F}(V_G))$ induced inequality of the σ_R at chosen $\hbar\omega$ and V_g transposes to absorption, thus, ultimately preventing stable operation of the considered device.

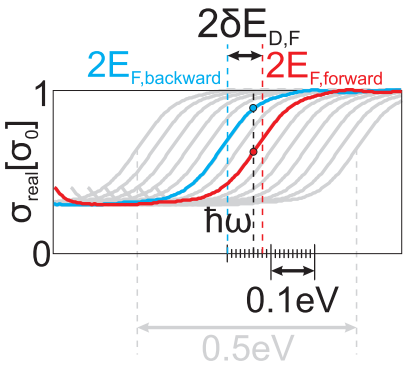

Figure 4.19: An example showing how the offset of the Fermi level which occurs in the forward and backward gate swipes affects the performance of an hypothetical graphene based optical device operated at $\hbar\omega$. The optical conductivity of graphene, represented by gray, blue and red curves is taken from Ref. [24] and displaced along the $\hbar\omega$ axis in order to simulate device's behaviour when the V_G is changed.

4.2.3 Graphene-Optical Waveguide System

The gate-controlled absorption and compatibility with standard CMOS and SOI technologies indicate that graphene has a high potential as a building block of various optoelectronic devices [22; 23; 30] including photodetectors [32], optical modulators [101; 102], polarizers [103], sensors [104] and mode-locked lasers [105]. Any of these devices can be achieved by coupling an optical waveguide with graphene. Therefore, we shall start by investigating the effect that graphene has on guided modes of an optical waveguide [106; 107].

4.2.3.1 Interaction of Graphene and Guided Modes

The interaction between the graphene and a guided mode can be described via graphene's conductivity and a quantity, which we would henceforth call the waveguide-graphene coupling strength. For the derivation of this quantity we consider a simple slab waveguide geometry as a toy model, while it will be evident that the reasoning is straightforwardly extended onto waveguide geometries used in practice, such as the strip waveguide [101; 102] or an optical fiber [103]. A planar dielectric waveguide extending infinitely along the y and z directions is illustrated in the inset of figure 4.20. The thickness of the waveguide (layer 2) is d while the superstrate (layer 1) and substrate (layer 3) are semi-infinite in the x direction. Light waves are assumed to propagate in the y direction, their propagation constant being denoted by k_y.

We shall consider the typical case of $\varepsilon_2 > \varepsilon_3 > \varepsilon_1$, corresponding to a waveguiding slab of permittivity ε_2 grown on a substrate with permittivity ε_3 and surrounded by air with $\varepsilon_1 = 1$. In particular, we shall consider the technologically most relevant case of a silicon-on-insulator (SOI) system where the waveguide is made of silicon

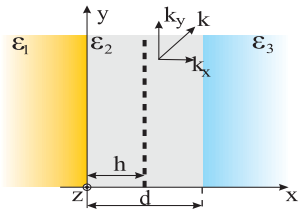

Figure 4.20: Illustration of the planar waveguide geometry with graphene (the vertical dashed line) positioned at distance h from the waveguide-superstrate interface.

with a silicon-dioxide substrate. Around the telecommunication frequencies ($\lambda \approx 1.5\mu$m), the silicon and silicon-dioxide permittivities are $\varepsilon_2 = 12.25$ $\varepsilon_3 = 2.25$.

A waveguide mode of the figure 4.20 geometry with frequency ω and propagation constant k_y comprises plane-wave components in the three layers, each satisfying the following dispersion relation

$$k_n^2 = \varepsilon_{\mathrm{n}}\varepsilon_0\mu_0\omega^2 - k_y^2, \tag{4.9}$$

where k_n is the x-component of the wave vector $\mathbf{k}$, and n=1,2,3 denotes layers of the structure. In case of a lossless waveguide, guided modes have a real propagation constant k_y, with k_n being purely imaginary in layers 1 and 3 and purely real in the slab. The inclusion of graphene induces losses and the propagation constant becomes complex i.e. $k_y = k_y^{\mathrm{R}} + \mathrm{i}k_y^{\mathrm{I}}$. Accordingly, the value of k_n becomes complex in all three layers. As an example, figure 4.21 shows the dispersion curves of the two lowest TE and TM (fundamental and first order) modes calculated by the outlined numerical procedure. The thickness of the silicon ($\varepsilon_2 = 12.25$) slab was set to $d = 220$ nm while silicon-dioxide ($\varepsilon_3 = 2.25$) is assumed as the substrate. The graphene layer is placed in the center of the slab. The field distributions of a graphene-coupled waveguide are practically the same as those of the bare waveguide. The modes of the bare waveguide are not depicted: the dispersion of k_y^{R} would practically overlap the graphene-coupled dispersions, while the k_y^{I} components are identically equal to zero in the bare waveguide. Therefore, the effect of graphene is to introduce nonzero values of k_y^{I} and to slightly shift k_y^{R} (not visible in the current scale).

Graphene-Waveguide Coupling Strength. We now introduce a quantitative measure for the graphene-waveguide coupling strength. Starting from the graphene-coupled waveguide but replacing $\sigma(\omega)$ by an infinitesimally small conductance $\Delta\sigma$, the bare waveguide dispersion $k_y(\omega)$ of a given mode is retrieved as $\Delta\sigma \to 0$. A nonzero but very small $\Delta\sigma$, will modify the propagation constant by $\Delta k_y(\omega)$, which, to the first order, is proportional to $\Delta\sigma$. We thus define the graphene-waveguide

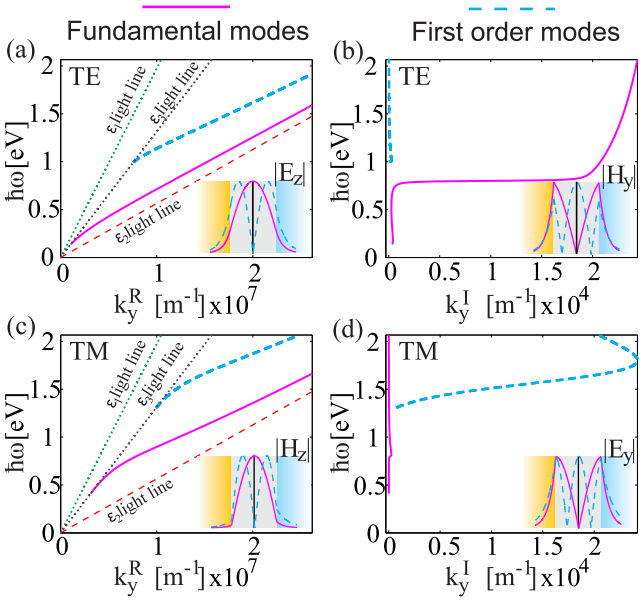

Figure 4.21: Calculated real $k_y^{\mathrm{R}}(\omega)$ and imaginary $k_y^{\mathrm{I}}(\omega)$ dispersion curves for a $d = 220$ nm thick SOI waveguide, $\varepsilon_1 = 1$, $\varepsilon_2 = 12.25$, $\varepsilon_3 = 2.25$ and assuming the theoretical $\sigma(\omega)$ calculated for $E_{\mathrm{F}} = 0.4$ eV. Panels (a) and (b) show the real and imaginary parts of k_y for the fundamental and the first order TE modes, while (c) and (d) depict the two lowest TM modes. The insets depict the modal field distributions at $\hbar\omega = 1.45$ eV.

coupling strength $G(\omega)$ as the derivative:

$$G(\omega) = -i\frac{\mathrm{d}k_{\mathrm{y}}(\omega)}{\mathrm{d}\sigma}, \tag{4.10}$$

with the $-i$ multiplier introduced for convenience (it makes $G(\omega)$ almost entirely real, as shown below) and where $\mathrm{d}\sigma$ can have an arbitrary phase. In case $|\sigma|$ becomes sufficiently larger than zero, so that $\mathrm{d}k_y(\omega)/\mathrm{d}\sigma$ evaluated at $\sigma = 0$ is significantly different from the derivative evaluated at $|\sigma| > 0$, the coupling strength should be considered as a function of both conductivity and frequency. However, this would typically require values of $|\sigma|$ larger than $30\sigma_0$, which is much higher than the conductance of a single or few layer graphene at these frequencies. Considering that graphene practically does not change the electromagnetic fields, we may invoke the perturbation theory [108] to show that

$$\Delta k_y(\omega) \approx i\sigma(\omega)G(\omega). \tag{4.11}$$

As σ is a complex quantity i.e. $\sigma = \sigma^{\mathrm{R}} + \mathrm{i}\sigma^{\mathrm{I}}$, it becomes clear that

$$\Delta k_y^{\mathrm{R}} = -\sigma^{\mathrm{I}}(\omega)G(\omega), \quad \Delta k_y^{\mathrm{I}} = \sigma^{\mathrm{R}}(\omega)G(\omega). \tag{4.12}$$

Equation (4.12) indicates that, if graphene only weakly perturbs the waveguide

modes, the changes of the real and imaginary part of the propagation constant are directly determined as a product of $G(\omega)$, which is an inherent property of the bare waveguide, and the imaginary and real parts of $\sigma(\omega)$, respectively. Furthermore, separation of graphene and the waveguide provided by the perturbation method significantly simplifies numerical calculations. The obvious outcome of equation (4.12) is thus the well-known fact that a mode couples more strongly to graphene when the position of the graphene layer h is set to points of the in-plane electric field maxima. However, the more important outcome of equation (4.12) is that it allows a direct comparison of coupling strengths at different frequencies and waveguide geometries, simply by comparing $G(\omega)$.

To test the validity of equation (4.12), we consider the SOI waveguide from figure 4.20. We calculate $\Delta k_y = \Delta k_y^{\mathrm{R}} + \mathrm{i}\Delta k_y^{\mathrm{I}}$ by the reflection pole method ('Exact') and compare the results with the perturbative values ('Perturbation method'), for two values of E_{F}. Figure 4.22 shows the comparison of Δk_y^{R} and Δk_y^{I} for the fundamental TE, panels (a) and (b), and TM mode, panels (c) and (d). The perturbative expression appears highly accurate for a single-layer graphene.

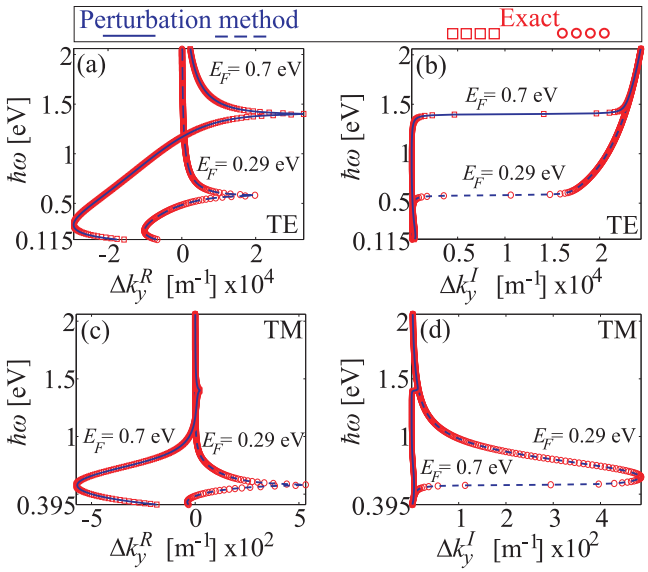

Figure 4.22: Comparison of the numerically calculated ('Exact') and the perturbative ('Perturbation method') values of the graphene-induced changes of the propagation constant Δk_y, obtained for the waveguide from figure 4.20. The top row, (a) and (b), shows the real and imaginary parts of Δk_y for the fundamental TE mode, while the bottom row, (c) and (d), shows the corresponding quantities for the TM mode.

We now attempt to quantify this accuracy and establish the limits of its validity. To this end, we introduce the relative error as $\delta = |\Delta k_y^{\mathrm{e}} - \Delta k_y^{\mathrm{p}}|/|\Delta k_y^{\mathrm{p}}|$, with 'e' and 'p' indicating the exact and perturbative value, respectively. The extent to which graphene will perturb a mode of given frequency ω is clearly determined by

how big $\sigma(\omega)$ is which, in turn, depends on E_F. In the range of telecommunication frequencies ($\lambda \approx 1.5\mu$m), the practically achievable [24] values of E_F are such that $|\sigma(\omega)|$ is few σ_0 at most. Therefore, in figure 4.23 we investigate δ by selecting a mode of a given frequency and polarization and then calculate the variation of δ as a function of the real or imaginary part of $\sigma(\omega)$. All of the relative errors shown in figure 4.23 are below 9% up to above $M = 30$ and almost independent on whether σ is real or imaginary. The reason that δ increases with M is that the field distributions of the perturbed waveguide are gradually becoming more different than those of the bare waveguide, meaning that the assumptions made in deriving the perturbative expressions [108] gradually break down. Considering that the values of $|\sigma(\omega)|$ are expected to be $\sim 3\sigma_0 - 4\sigma_0$ at most, $M = 30$ would correspond to inserting around 10 layers of graphene into the waveguide, which is much more than the technologically relevant case of one or two layers [101; 102]. Therefore, figure 4.23 asserts that the expected worst-case accuracy of the perturbative expressions for a single graphene layer is better than 1% and that it is well-behaved even for a larger number of layers.

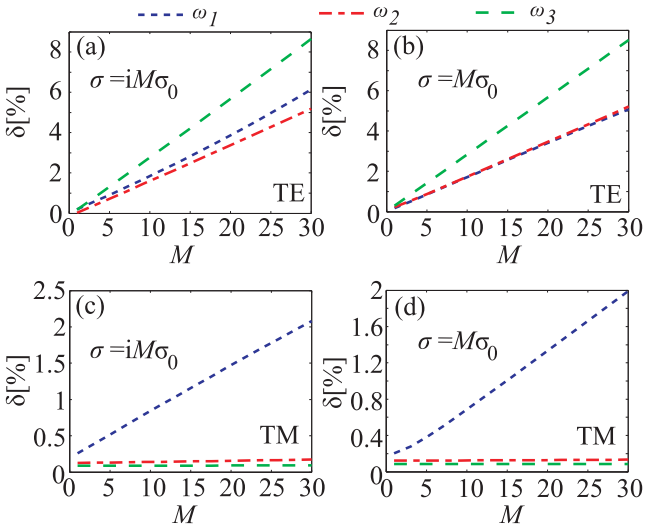

Figure 4.23: Relative errors δ as a function of σ for purely imaginary values, (a) and (c), and purely real values, (b) and (d). The top panels show δ for the fundamental TE mode of the SOI waveguide from figure 4.20 calculated at $\hbar\omega_1 = 0.35$ eV, $\hbar\omega_2 = 1.1$ eV and $\hbar\omega_3 = 1.85$ eV. The bottom panels show the corresponding δ for the fundamental TM mode, calculated at $\hbar\omega_1 = 0.55$ eV, $\hbar\omega_2 = 1.2$ eV and $\hbar\omega_3 = 1.9$ eV.

Analysis of Graphene-Waveguide Coupling Strength. Here we proceed further by analyzing the graphene-waveguide coupling strength for two types of waveguides: (i) the SOI slab waveguide and (ii) the, technically more relevant, SOI strip waveguide.

The $G(\omega, h)$ factor of the SOI slab waveguide is plotted as a function of the spatial coordinate $x = h$ and frequency $\hbar\omega$, for both TE (figure 4.24(a)) and TM (figure 4.24(b)) modes. Here, the G is divided by the vacuum impedance $z_0 = \sqrt{\mu_0/\varepsilon_0}$ and plotted in units of $[\mathrm{m}^{-1}]$.

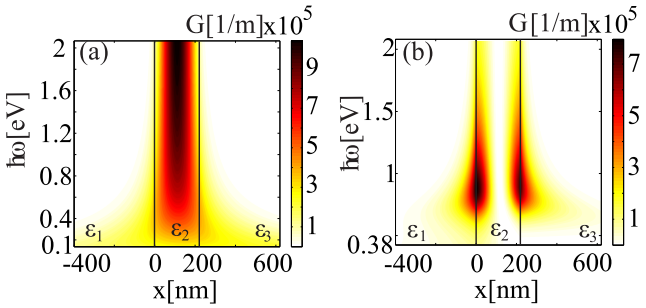

Figure 4.24: The G-factor of (a) the fundamental TE and (b) the fundamental TM mode for the SOI waveguide given in figure 4.20, plotted as a function of both the frequency ω and the position of graphene, $h = x$.

As the frequency increases, both TE and TM modes in figure 4.24 become more confined to the slab. In symmetrical waveguides, the field amplitude minima (nodes) and maxima (antinodes) have fixed positions determined by symmetry. Here, due to the substrate-superstrate asymmetry, the normalized field minima and maxima shift with ω approaching the middle of the slab with increasing ω. At lower frequencies, especially near the cut-offs, these extremal points are slightly shifted towards the substrate. Thus, by positioning graphene $h = d/2$, the coupling efficiency is nearly maximized (minimized) for the TE (TM) mode for frequencies sufficiently above the cut-off.

In case of the SOI strip waveguide, we focus on waveguides operated in the true single mode (TSM) regime, defined as the regime in which exactly one mode (qTE or qTM) is allowed to propagate at the operating frequency $\hbar\omega_{\mathrm{op}} = 0.8\,\mathrm{eV}$. The quantity denoted below by G refers to the coupling strength of the appropriate mode with graphene at $\omega \approx \omega_{\mathrm{op}}$. In contrast to TSM, the term single mode regime is used in the literature [109] for cases in which the waveguide supports either only one mode, or two modes but with orthogonal polarizations (the lowest qTE and qTM modes).

Figure 4.25 shows the grayscale (color) map of G as a function of the silicon strip height H and width W, calculated for a waveguide entirely covered by graphene (as sketched by the bottom-left inset) within a part of the $H-W$ parametric plane that belongs to the TSM regime. The later comprises two disjoint regions denoted by qTE (upper left) and qTM (lower right), representing the $H - W$ values for which the fundamental mode is qTE and qTM, respectively, while higher modes are not allowed. The qTE and qTM regions in figure 4.25 would be symmetric across the

$H = W$ curve, if it not were for the silica substrate. Since the silica refractive index ($n = 1.44$) is higher than the refractive index of air, the horizontally polarized modes are slightly redshifted relative to their vertically polarized counterparts which causes the qTM region to slightly spill over into the $W > H$ half-plane. This further implies that in the close vicinity of the $H = W$ curve in the TSM regime, the modes always belong to the qTM polarization. As the fundamental cutoff frequency increases when decreasing either H or W, the part of the $H - W$ plane below and to the left of the TSM region corresponds to waveguides in which no mode is allowed to propagate at $\omega \approx \omega_{\text{op}}$. And vice-versa, the part of the $H - W$ plane above and to the right of the TSM grayscale (color) map, represents the waveguides supporting at least two modes at $\omega \approx \omega_{\text{op}}$.

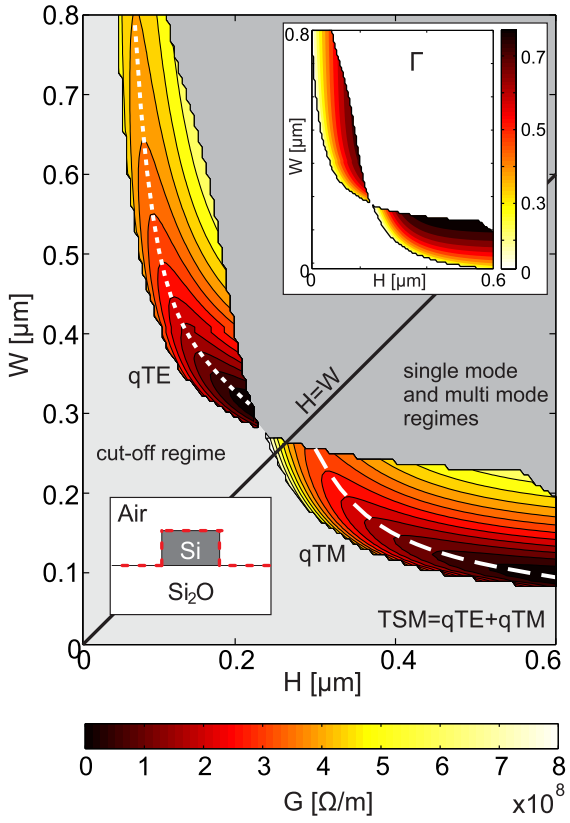

Figure 4.25: Grayscale (color) map of G calculated at $\lambda = 1.55$ μm for the structure shown in the lower inset (graphene layer is represented by the thick dotted line). The upper inset shows the corresponding mode confinement factors Γ.

We find from figure 4.25 that the qTE modes have very efficient coupling with the graphene layer for waveguide geometries near the $H = W$ curve. In case of qTM modes, high values of G are reached further away from the $H = W$ curve, increasing even further for heights beyond the range shown in figure 4.25. For any given H, there is a single value of W for which G reaches a maximum. The dotted and dashed lines in figure 4.25 connect these maxima. The existence of such extremal points within the TSM regime is a direct proof that the graphene-waveguide coupling

strength cannot simply be expressed in terms of the mode confinement factor Γ. Since the graphene layer covers the outer boundaries of the waveguide, at first it might appear that modes which are less confined will have a higher G. However, this is not what is seen in figure 4.25, which shows that G actually decreases to zero at the boundaries between TSM and the cut-off regime.

4.2.3.2 Application of Graphene-Waveguide System in Electro-Optical Modulators

There are two strategies in designing graphene-based optical modulators. In the more popular EAMs, graphene is used for tuning the absorption of the wave as it propagates along the waveguide[101; 102]. The efficiency of such a modulator is, therefore, determined from the graphene-induced variation of Δk_y^{I}. Alternatively, in ERMs [110] graphene is used to induce a phase shift meaning that the efficiency of ERMs is determined by the magnitude of Δk_y^{R}. In view of equation (4.12), we find that in both cases, the efficiency of the modulation is proportional to the $G(\omega)$ factor.

Electro-Absorptive Graphene Based Optical Modulators. In EAMs, the electrically induced change in the absorption coefficient is used in order to modulate light. Actually, by changing the absorption coefficient the modal propagation length $L_{\mathrm{e}} = 1/k_y^{\mathrm{I}}$ is changed. Obviously, the size of L should be at least several times larger than L_{e} of the mode propagating in the 'off' state of the waveguide. Figure 4.26(a) shows a schematics of a EAM based on the waveguide coupled with graphene.

The shift of the Fermi level in graphene enables switching between the intra- and inter-band transitions and allows the tunning of the absorption coefficient $\alpha = 2\Delta k_y^{\mathrm{I}}$. The dotted and dash-dotted lines in figure 4.26(b) show the real and the imaginary part of the optical conductivity obtained from the Ref. [24] data by displacing both $\sigma^{\mathrm{R}}(\omega)$ and $\sigma^{\mathrm{I}}(\omega)$ so that $2E_{\mathrm{F}}$ falls to 0.8 eV.

The points 1 and 2 ($1'$ and $2'$) shown in figure 4.26(b) illustrate how the values of the real part of the conductivity should be chosen in order to achieve a desirable difference between absorption coefficients. The 1 and $1'$ points correspond to σ^{R} closest to $2E_{\mathrm{F}}$, for which the absorption coefficient has the lowest value. Similarly, the 2 and $2'$ points correspond to σ^{R} closest to $2E_{\mathrm{F}}$, for which the absorption coefficient has the highest value. Clearly, points $1'$ and $2'$ are moved further away from $2E_{\mathrm{F}}$ than those of the calculated conductivity, since the slope of the experimental curve is wider than that of the calculated one.

The modulation is achieved by shifting the Fermi level in graphene so that the points 1 ($1'$) and 2 ($2'$) alternately match the operating frequency. Figure 4.26(c) shows the transmission coefficient versus the position of the Fermi level in graphene.

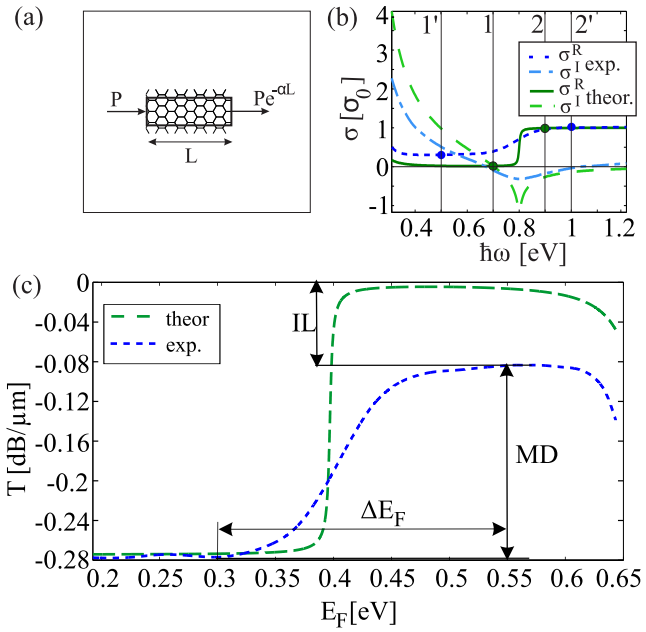

Figure 4.26: (a) Schematics of an graphene-based EAM. (b) The experimental (dotted and dash-dotted lines) and theoretical (full and dashed lines) $\sigma(\omega)$ spectra. The vertical lines show the position of 1, 1', 2 and 2' points used to explain the operational principle.(c) The waveguide transmittance in [dB/μm] as a function of E_{F}. The definition of IL, MD and ΔE_{F} is illustrated for the dotted curve.

The modulator is operated using the fundamental TE mode at $\hbar\omega = 0.8$ eV. The dashed line corresponds to the transmission coefficient of a modulator calculated for the theoretical $\sigma(\omega)$. In contrast, the dotted curve shows the transmission coefficient calculated with the experimental $\sigma(\omega)$. A comparison of the two curves, which are obtained for the same G and for two different conductivities (dashed and dotted lines in figure 4.26(c)), shows how the conductivity affects the overall optical performance of EAMs. In the idealized case, we have IL ≈ 0.005 dB/μm and MD ≈ 0.274 dB/μm. In the more realistic case, corresponding to the experimental dataset, IL ≈ 0.082 dB/μm and MD ≈ 0.196 dB/μm. Both the MD and IL are proportional to the coupling strength, G. Therefore, by optimizing the waveguide geometry one could optimize the performance of an EAM, but to a certain extent. In particular, by analyzing the transmission coefficients for various geometrical parameters and geometries, we find that the modulation depth to insertion loss ratio is, in fact, entirely independent on the waveguide geometry and given by

$$\frac{\mathrm{MD}}{\mathrm{IL}} = \frac{1-p}{p}, \tag{4.13}$$

where p represents the residual conductance at frequencies slightly below the interband threshold frequency. p is expressed in the units of universal optical conductance of graphene, σ_0. Consequently, apart from the coupling strength G, the optical con-

ductivity of graphene has an equally important role in graphene based EAMs, as p sets the lower bound on the insertion loss.

Electro-Refractive Graphene Based Optical Modulators. ERMs are commonly constructed using Mach-Zehnder interferometers [110]. Two waveguides, which are also called the arms, have different real parts of the modal index and this induces a phase lag between the two propagating waves. At the output of the device, where the waveguides are coupled, the waves can interfere constructively or destructively. Figure 4.27(a) shows a sketch of a Mach-Zehnder modulator based on waveguides coupled with graphene. The waveguides forming the arms are assumed to be the same.

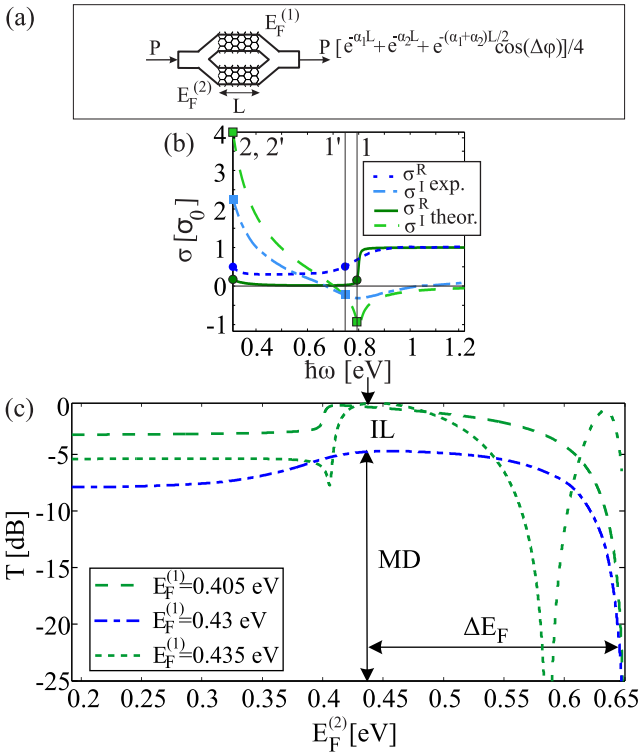

Figure 4.27: (a) Schematics of a graphene-based ERM. (b) Explanation of the ERM working principle using the experimental (dotted and dash-dotted lines) and theoretical (full and dashed lines) $\sigma(\omega)$ spectra. The vertical lines show the position of 1, 1', 2 and 2' points used to explain the operational principle. (c) Transmission coefficient versus E_F. The definition of IL, MD and ΔE_F is illustrated for the dash-dotted curve.

At a given operating frequency, the waves passing through the two arms will interfere constructively or destructively if their relative phase difference, $\Delta\phi$, is $2m\pi$ or $(1+2m)\pi$, respectively, where m is an integer. Assuming the length of both arms is set to L, $\Delta\phi = (k^{R}_{y,1} - k^{R}_{y,2})L$, where $k^{R}_{y,1}$ and $k^{R}_{y,2}$ are the real parts of the

propagation constant in the two arms. Using equation (4.12), we have

$$\Delta\phi = \left(\sigma_1^{\mathrm{I}} - \sigma_2^{\mathrm{I}}\right) GL = \Delta\sigma^{\mathrm{I}} GL. \tag{4.14}$$

Having a higher difference of σ^{I} in the two arms, obviously allows the construction of a shorter modulator. Also, by optimizing the parameters of the waveguide, i.e. by increasing G, the L can be reduced even more. The real part of the conductivity is also important since it determines the absorption of the modes in arms. The absorption should be approximately equal in both arms, in order to allow for a destructive interference (the 'off' state). In the design of an ERM, two characteristic lengths should be considered. The first is the modal propagation length L_{e}, which is given by $L_{\mathrm{e}} = 1/(\sigma^{\mathrm{R}} G)$. The second important length is the length required to achieve a phase shift of $\Delta\phi = \pi$ between the two arms. Using equation (4.14), L_π it is given by

$$L_\pi = \frac{\pi}{\Delta\sigma^{\mathrm{I}} G}. \tag{4.15}$$

The $L_{\mathrm{e}} > L_\pi$ condition ensures that the waves are not considerably absorbed before they interfere. This condition is fulfilled if $\Delta\sigma^{\mathrm{I}} > \pi\sigma^{\mathrm{R}}$. Thus, the values of σ^{I} and σ^{R} should be chosen in the region below $2E_{\mathrm{F}}$, as it is shown in figure 4.27(b) by points 1, 2, 1′ and 2′. Dotted and dash-dotted lines represent σ^{R} and σ^{I} of the experimental dataset, respectively, while the full and dashed lines are the calculated values at $E_{\mathrm{F}} = 0.4\mathrm{eV}$.

The modulation of the light is achieved by changing E_{F} in one of the arms, while it is kept fixed in the other (reference) arm. Here, E_{F} in the reference arm is denoted by $E_{\mathrm{F}}^{(1)}$ and adjusted to provide matching between the position of point 1(1′) and the mode's operational frequency. When the Fermi level in the other arm, denoted as $E_{\mathrm{F}}^{(2)}$ is at the same value as $E_{\mathrm{F}}^{(1)}$, the waves interfere constructively at the output. In contrast, when the $E_{\mathrm{F}}^{(2)}$ is shifted so the position of point 2(2′) matches the operational frequency, the waves interfere destructively at the output.

Figure 4.27(c) shows the transmission coefficient versus the position of the Fermi level in graphene in arm 2. The modulator is operating using the fundamental TE mode at $\hbar\omega = 0.8$ eV. The dashed and dotted curves correspond to the theoretical $\sigma(\omega)$ calculated for two different values of the Fermi energy in the reference arm, $E_{\mathrm{F}}^{(1)} = 0.405$ eV and $E_{\mathrm{F}}^{(1)} = 0.435$ eV with corresponding $L_\pi = 20$ μm and $L_\pi = 63$ μm, respectively. The dashed-dotted curve is obtained using the experimental dataset with $E_{\mathrm{F}}^{(1)} = 0.43$ eV and the corresponding $L_\pi = 40$ μm. For the mentioned L_π values, the $L_{\mathrm{e}} > L_\pi$ condition is fulfilled.

Since the absorption is held the same in both arms and the length of the arms is chosen to be $L = L_\pi$, the transmission coefficient is equal to $-\infty$ dB when the waves interfere destructively. Graphs in figure 4.27(c) are shown starting from

$T_r = -25$ dB. Accordingly, the modulation depth is MD $= \infty$ dB. If the absorption is not the same in the two arms, or if the π phase shift can not be achieved for a reasonable L_π, the MD would have a finite value. On the other hand, IL is determined by the real part of σ and has finite values and is smaller when the theoretical $\sigma(\omega)$ is used. The difference between the modulator properties calculated with theoretical and experimental $\sigma(\omega)$ is mainly manifested as a difference in IL and ΔE_F. It is also seen that the minimal modulator length for theoretical $\sigma(\omega)$ is around two times shorter than the one estimated with the experimental dataset.

4.3 Conclusion

To conclude, in the first part of this chapter graphene and graphene back-gate devices were studied by the AFM and KPFM techniques. From the AFM study, a conclusion that the thickness of graphene and, consequently, few layer graphene cannot be unambiguously determined by utilizing the tapping AFM in ambient conditions is reached. More importantly, we have found that the micromechanical exfoliation yields imperfect graphene/few-layer graphene samples usually covered by various adsorbates and fabrication residues. The spatial variations of the CPD within graphene, ascribed to the spatial variations of the doping levels, further revealed that these adsorbates and residues in conjunction with the substrates surface disturb the state of the intrinsic graphene. However, these seemingly small CPD variations were neglected and the reminder of the study was done by considering spatially averaged CPD values. Consequently, the influence of the substrate, adsorbates and residues on graphene was taken into account through an initial Fermi level shift unique across the entire graphene. In addition, we have demonstrated inability of graphene to completely screen the electric filed applied between the Si electrode and the KPFM tip.

In the KPFM based investigation of graphene back-gate devices, we have shown that the Au electrode used for electrical gating additionally modifies the doping state of graphene in the vicinity of the contact area. The region in which this occurs is seen to be slightly affected by the applied gate voltage. Perhaps most importantly, by comparison of the device exposed to ambient conditions and the device isolated by a thin layer of protective oxide, we have shown the superior performance of the isolated device when the gate voltage is applied, as quantified by negligible Fermi level offsets. While the Fermi level within the isolated device changes according to $\sim \sqrt{|Vg|}$ dependance, the V_G induced E_F shifts in case of the non-isolated device are found to be strongly influenced by the adsorbates supplied to graphene from the environment. In addition, we have demonstrated how these erratic shifts of the Fermi level can, possibly, deteriorate operation of an hypothetical graphene-

waveguide based device.

From another perspective, we have shown that both EFM and KPFM are able of accessing graphene below an insulator. Such way of imaging was previously demonstrated on carbon nanotubes embedded in an insulator matrix [111].

In the second part of this chapter we have investigated graphene-waveguide coupled systems and their application in electro-optical modulators. Using the planar waveguide toy model with realistic material parameters, we have demonstrated that graphene induces a slight change in the modes propagation constant, by modifying its real part and by introducing a non-zero imaginary part. More importantly, we have shown that the graphene-induced change of the propagation constant is given by the product of a factor characterizing the graphene-waveguide coupling strength (G) and the optical conductivity of graphene. This method has been shown to posses an excellent accuracy with relative errors of around 1% for the practically relevant cases. By analysing the graphene-waveguide coupling strength for the SOI slab and strip waveguides, we have shown that the maximal coupling efficiency is achieved by positioning graphene at locations where the electric filed, or rather its component parallel to the graphene's plane, has maximal value.

Finally, we have discussed how graphene-waveguide coupled system can be utilized for realization of elector-absorptive and electro-refractive optical modualtors. Considering that graphene's optical conductivity can vary significantly depending on the graphene fabrication procedure and environment, we have simultaneously investigated the predictions of the theoretical and experimental dataset. As expected, the theoretical dataset has been found to predict a considerably better modulator performance. We have also shown that, in case of electro-absorptive optical modulators, the ratio of the modulation depth to insertion losses, which is a commonly used figure of merit for electro-optical modulators, does not depend on the waveguide geometry and graphene coverage at all but that it is exclusively a function of the residual conductivity of graphene.

Chapter 5 Optical spectroscopy of two-dimensional excitons in molybdenum disulfide monolayers

Monolayers of semiconducting transition metal dichalcogenides (TMDs), such as molybdenum disulfide, exhibit encouraging light-emitting and nonlinear optical properties at visible frequencies. Consequently TMDs have a high potential for use in future ultracompact active and nonlinear optical devices [32], provided an efficient light coupling mechanism is arranged. A possible approach to enhance the light-matter interaction in TMDs is the use of noble metal nanostructures [26] which can confine light to extremely small volumes via the excitation of localized surface plasmons.

In this chapter, we use Raman and photoluminescence (PL) spectroscopy to investigate the influence of the spherical citrate capped nanoparticle (NP) clusters, on light emitted from single- and few-layer MoS_2.

5.1 Materials and Methods

5.1.1 Sample Fabrication and Experimental methods

The nanoparticles are synthetized by wet chemistry using two different methods described in Refs. [112; 113]. In both methods, the reduction of silver nitrate ($AgNO_3$) precursor, by either sodium borohydride ($NaBH_4$) or ethylene-glycol ($C_2H_6O_2$) is the basis for obtaining silver seeds from which the nanoparticles are grown. The stability of the nanoparticles and their tendency toward clustering is usually controlled by introducing stabilizing reagents. These reagents bind to the specific facets of the growing crystals and, therefore, to a certain extent, influence the final shape of the nanoparticles [114]. For achieving the desired nanoparticle shape equally important are the reducing agents and the growth parameters (such as the temperature at which these reactions are maintained) [114; 115]. The procedure described in Ref. [112], where sodium-citrate is used as stabilizing reagent yields colloidal dispersion of citrate anion-coated nearly spherical nanoparticles, whereas the procedure described in Ref. [113] yields colloidal dispersion of Poly(vinyl pyrrolidone)-coated

cubical nanoparticles. Examples of spherical and cubical nanoparticles used in this research are shown in figure 5.1. Prior to the scanning electron microscope imaging, the nanopartciles were deposited, from their colloidal dispersions, onto the surface of highly-oriented-pyrolytic-graphite. The average diameter of spherical nanoparticles is about 25 nm, whilst the average size of cubical nanoparticles is around 40 nm. Silver nanoparticles are used because silver has small losses at the 532 nm (the wavelength of the incident laser).

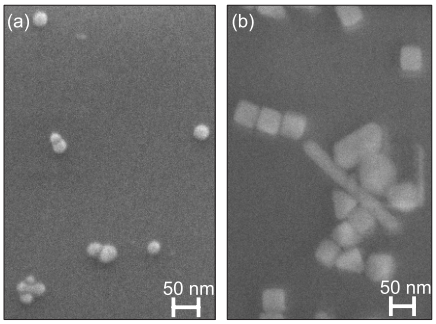

Figure 5.1: Scanning electron microscope images of the citrate anion capped spherical nanoparticles and PVP capped cubical nanoparticles.

Thin layers of MoS_2 were prepared by micromechanical exfoliation of the MoS_2 crystals. This procedure has already been utilized for fabrication of graphene flakes in Chapter 4. Briefly, thin layers of MoS_2 exfoliated by a sticky tape are transferred on the clean surface of either 90 nm or 300 nm thick SiO_2 which is supported by a thick (bulk) Si crystal. Some of the prepared MoS_2 flakes on the SiO_2/Si substrates are displayed in figure 5.2. The contrast between the thin MoS_2 layers and the substrate is enhanced due to the underlying substrate which acts as a Fabri-Perot resonator for the incident (visible) light, similarly as in the case of graphene [see Chapter 4].

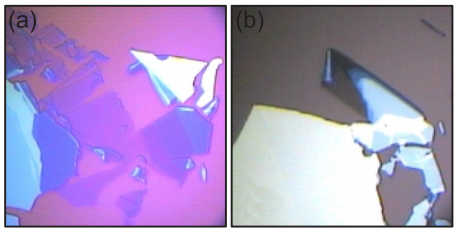

Figure 5.2: Optical microscopy images of various MoS_2 flakes on SiO_2/Si substrate, made by micromechanical exfoliation.

The MoS_2 monolayer absorbs around 5-10% of the incident (visible) light is almost 2-5 times more than the amount of visible light graphene can absorb. Therefore, MoS_2 monolayers have better contrast with respect to the substrate and are more easily observed under the optical microscope than the graphene samples.

After preparation of the $MoS_2/SiO_2/Si$ substrates the afore prepared nanoparticles are deposited from their colloid dispersions using the drop-cast method. Even though being the easiest way to deposit any kind of colloids on any kind of surface, the drop-cast method does not offer any kind of control in the final positions and the arrangement of nanoparticles at the target surface.

The experiments are performed using commercial NTegra Spectra system from NT-MDT, which allows confocal Raman spectroscopy and atomic force microscopy to be done simultaneously. In this way one is able to acquire spatially resolved chemical information of the sample along with its surface topography at the same place. The AFM is operated in tapping mode in order to minimize the lateral force between the tip and the sample induced by lateral movements of the tip across the sample. Large values of the lateral force, comparable to those occurring in the contact mode, are certain to result in unwanted movements of the nanoparticles, or their clusters, which are not bounded to the substrate. The cantilever-tip system is oscillated at the characteristic first order resonance which is usually in the 90-230 kHz range. For Raman spectroscopy, a linearly polarized semiconductor laser operating at a wavelength of 532 nm was used. The absorbed laser power was varied from 2 to 0.2 mW within the 1 x 1 μm sized focus, depending on the sensitivity of the sample.

5.1.2 Numerical Methods

To numerically solve the classical Maxwell equations we have used the finite element method implemented within the Comsol Multiphysics software package [45]. We consider clusters of spherical and cubical Ag NPs on a substrate under plane wave illumination. The silver dielectric constant is taken from Rakic et al. [116]. The substrate is assumed to be semi-infinite and isotropic with a dielectric constant of 2.25, which roughly corresponds to the dielectric constants of both mica and SiO_2 at visible frequencies. The surrounding medium is vacuum and its dielectric constant is 1. For purposes of efficient meshing, the spherical NPs are assumed to lie 1 nm above the substrate, whereas the cubical NPs lie directly on the substrate surface. The clusters are formed in the plane which is parallel to the substrate by allowing the NPs to have random position but under the following conditions: (i) the minimal allowed distance between adjacent NPs is d=1.2 nm, (ii) every NP must be at 1.2 nm distance form at least one neighbouring nanoparticle. By imposing the afore conditions we were able to achieve various cluster geometries and mimic the lack of control over the clusters morphology in the experiment.

The absorption, scattering and extinction cross sections are calculated as a function of the excitation wavelength, λ, utilizing general expressions provided

in Ref. [117]. The local electric field enhancement is quantified by the factor $f(\lambda) = |\mathbf{E}(\lambda)|^2/|\mathbf{E}_0(\lambda_{\text{inc}})|^2$. Here, λ_{inc}, $|\mathbf{E}|$, $|\mathbf{E}_0|$ are the incident laser wavelength, the total scattered field and the incident field amplitudes, respectively. The average intensity enhancement is further estimated by integrating the intensity enhancement over the NP cluster surface which is followed by normalization of the obtained result to the surface area of the NP cluster.

5.2 Results and discussions

5.2.1 Topographic and Optical Properties of Pristine MoS_2

The MoS_2 samples produced by micro-mechanical exfoliation are not perfect. Rarely is one able to isolate a large sample of a specific thickness. As shown in figure 5.2, majority of the samples consist of segments with different thicknesses. Evaluating the thickness and number of layers of a specific MoS_2 sample is necessary since the optical properties of MoS_2, which we want to study, depend on number of layers. Apart from quick identification and qualitative description of the exfoliated thin MoS_2, optical microscopy can be used for determination of the number of layers (i.e. the thickness) of the considered samples [118; 119]. This approach, however, is indirect and requires an appropriate optical model from which the thickness can be extracted. Alternatively, one can use a more direct method, the atomic force microscope, to measure the thickness and determine the number of layers while having a benefit of additional topographical information on a micro- and nano-scale, not attainable by an optical microscope.

Panel (a) in figure 5.3 shows an atomic force microscopy topograph of the selected MoS_2 flake. The flake is split into fragments consisting of segments with different thicknesses. The variation of thickness is seen as the variation of the color in the topograph. Areas having the brightest color are very high (around 50 nm) and are presumably either residues left during the fabrication process or mechanically deformed/wrinkled parts of the MoS_2 flake which are also a consequence of the fabrication process. Smaller localized features distributed within each MoS_2 fragment are presumably either residues or mechanical deformations, as well. Panel (b) in figure 5.3 shows the corresponding phase map. The apparent phase contrast between the MoS_2 and the substrate is due to the variations of the surface properties (such as elasticity and adhesion) to which the phase is sensitive. In panel (c) plotted are topography and phase profiles taken along the lines in panels (a) and (b) which are crossing the edge between the triangle shaped MoS_2 fragment and the substrate. Comparison of these profiles confirms that the afore noted phase contrast is, indeed, due to the differences in the surface properties and not due to the

variation of the height across the edges. The absence of the phase contrast within the individual fragments, on the other hand, indicates that the samples with different thickness have similar surface properties. A closer look at the topography and phase profiles in panel (d), which are taken along the edge of the triangle shaped fragment as indicated by long solid lines in panels (a) and (b), corroborates that the phase does not follow the topography profile, and that it does not experience any change when the thickness of the fragment changes. The localized areas, having the darkest color in the phase map, are measurement artifacts induced by abrupt, large changes of the phase (the amplitude also changes abruptly) occurring when the tip stumbles upon pronounced topographic features. Finally, the local variations in height initially identified as either residues or mechanical deformations cannot be differentiated from the surrounding MoS_2 in the phase map. Therefore, they are either mechanical deformations of MoS_2 or residues covered by the MoS_2. In fact, we find that the majority of the samples produced by exfoliation have the same characteristics as the sample shown in panel (a).

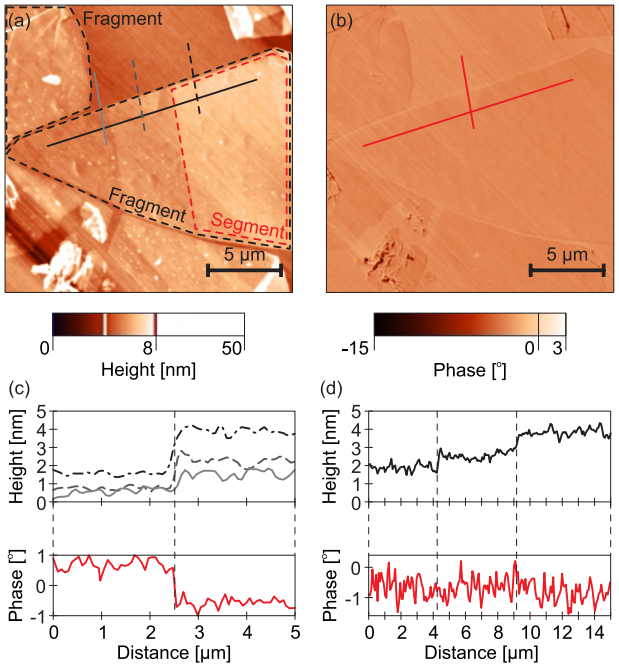

Figure 5.3: (a) Atomic force microscopy topograph of the MoS_2 sample. The areas marked by black and red dotted borders represent the fragments and the segments of the sample.(b) The corresponding phase image. (c) Topography and phase profiles taken along short (solid, dashed, dash-dotted) lines in panels (a) and (b), which are crossing the edge between the sample and the substrate. (d) Topography and phase profiles along the long solid lines in panels (a) and (b), which are stretched along the sample edge through the segments with different thicknesses.

Having examined the topography and surface properties of the exfoliated MoS_2 samples we proceed further by evaluating their thickness and number of layers. This will be done on the example of the triangle shaped MoS_2 fragment, as before.

It is commonly considered that monolayer of MoS_2 has thickness of 0.65 nm, a value which corresponds to the inter-layer spacing between the MoS_2 sheets in the bulk crystal [120]. Therefore, N number of layers would be N×0.65 nm thick. By measuring the height difference between the upper (MoS_2) and lower (substrate) levels of the topography profiles in upper part of panel (c), for example, we assess the following thicknesses: 0.86 nm, 1.71 nm and 2.3 nm. The first one is the closest to the thickness of the mono-layer, the second one is in-between the values corresponding to the thicknesses of both bi- and three-layer MoS_2, and the third one is the closest to the thickness of the four-layer MoS_2. Additional thickness evaluation across the considered MoS_2 fragment is done by comparing the levels of the topography profile in the upper part of panel (d). Here, height differences of 0.68 nm between the lowest and the middle level and of 0.7 nm between the middle and the highest level, more or less, coincide with the inter-layer spacing of 0.65 nm. Therefore the triangle shaped fragment shown in panel (a) consists of a mono-layer, bi-layer and three-layer MoS_2 segments. The overestimation of the MoS_2 segments height, when measured with respect to the substrate, is a consequence of using high tapping amplitude set points required to minimize the forces acting on the sample, and to avoid inflicting damage to the MoS_2. Similar observations were previously reported in the case of graphene [80], which is in comparison to MoS_2 more robust and mechanically stronger.

The atomic force microscopy measurements are commonly complemented by Raman spectroscopy measurements [121; 122; 123]. Here, apart from being used as a support to the atomic force measurements (for definite estimation of the number of layers), Raman spectroscopy setup is also used as a tool for characterisation of the photoluminescent (PL) properties of the thin MoS_2 samples.

In figures 5.4 (a) and 5.4 (b) the atomic force microscopy topograph and the corresponding total PL/Raman maps are shown. The color in panel (b) quantifies the average light intensity in the 530 nm - 790 nm spectral window. Each pixel in this map, therefore, represents a sum of the light intensity in the afore defined spectral window divided by the number of the wavelengths at which the signal is acquired. The segments having different number of layers exhibit different average intensities. In particular, comparisons of the topography and average intensity profiles taken: (i) across the sample and the substrate, and (ii) along the edge of the MoS_2 sample [see the cut lines in panels (a) and (b), and the profiles in panels (c) and (d)] demonstrate that thinner segments are more efficient light emitters than the thicker ones in spite of the reduced amount of material.

The spectrum acquired at the thinnest segment of the considered MoS_2 fragment is plotted in figure 5.5 (a). The total observed emission / scattering signal has the following components: (i) MoS_2 Raman (Stokes) scattering component, (ii) Si Raman (Stokes) scattering component and (iii) MoS_2 PL. The Rayleigh and

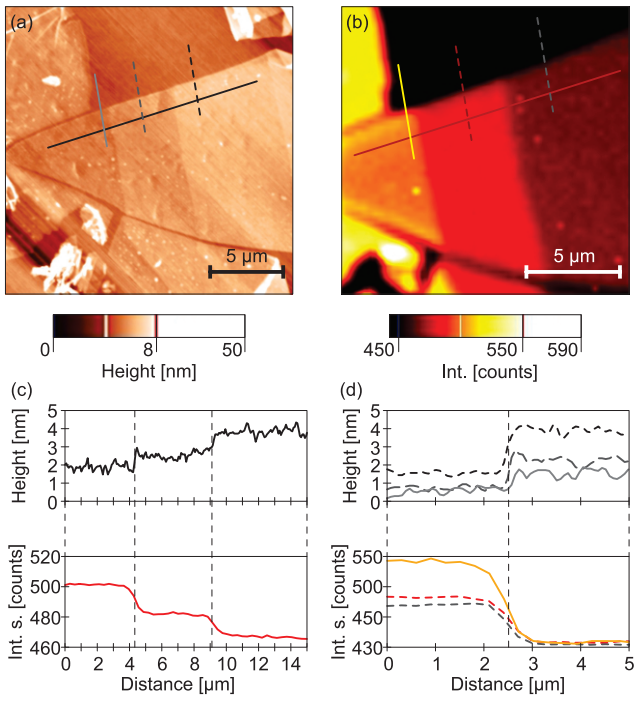

Figure 5.4: (a) Atomic force microscopy topograph of the MoS_2 sample. (b) The corresponding average PL/Raman intensity image. (c) Topography and average intensity profiles along the long solid lines in panels (a) and (b), which are stretched along the sample edge through the segments with different thicknesses.(c) Topography and average intensity profiles taken along short (solid, dashed, dash-dotted) lines in panels (a) and (b), which are crossing the edge between the sample and the substrate.

the Anti-Stokes scattering components below ∼535 nm, or below ∼100 cm^{-1}, are suppressed by an edge filter in order to protect the CCD photo-detector. The MoS_2 Stokes signal is found in the ∼543-544 nm range (380-420 cm^{-1} range), whereas the Si Raman (Stokes) signal lies in the ∼544-565 nm range (420-1100 cm^{-1} range). The narrow Si bands are left out from the upcoming discussion since their existence does not affect, in any way, the optical response of the MoS_2. Due to the spectral resolution of 1 nm (corresponding wave-number resolution is ∼35.3 cm^{-1}), the MoS_2 bands are not well resolved in figure 5.5(a). In figure 5.5(b), however, one can observe two characteristic bands assigned to the $E^1{}_{2g}$ and A_{1g} phonon modes. The spectra plotted in figure 5.5(b) are acquired at the mono-, bi- and three-layer segments as indicated by spots in the corresponding inset. The square markers represent the measured data, while the solid lines represent the fit to the measured data. Two Lorentzian functions are used for fitting and, as it can be seen, they match the measured data quite well. The distance between the bands, δ, is a good indicator of how many layers the sample has. In particular, thinner flakes have the two bands closer to each other than thicker ones. The distance between the two peaks (bands) is measured using the Lorentzian fit parameters. The three values, δ=18.69 cm^{-1},

δ=21.6 cm^{-1} and δ=23.3 cm^{-1} correspond to mono-, bi-, and three-layer MoS_2 [121; 124], respectively. Therefore the estimation of the number of layers based on the Raman band analysis concurs with the one based on the measurements by the atomic force microscope. Compared to the narrow Stokes components the PL is very spectrally wide and it spreads across the entire spectral window. The contrast seen in the map in figure 5.4 (b) is, therefore, dominantly determined by the MoS_2 PL.

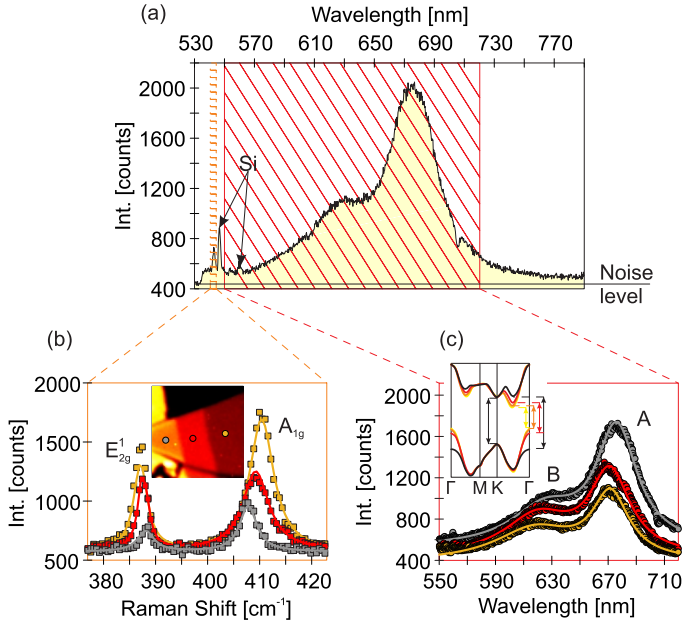

Figure 5.5: (a) The total PL/Raman spectrum. (b) MoS_2 Raman (Stokes) bands acquired at mono-, bi- and three-layer segments. Square markers represent measured data, whereas solid lines represent a fit. The inset shows the positions where the spectra is acquired. The color of the markers in the inset corresponds to the color of the Raman spectra. (c) MoS_2 photoluminescence taken at the same positions as the Raman spectra in panel (b). The inset illustrates how the topmost valence and lowermost conduction bands of MoS_2 change when the number of layers is changed (included are mono-, bi-, four-layer samples and bulk crystal). This inset is taken from Ref. [125] and slightly modified.

Figure 5.5(c) displays the PL part of the entire spectrum which is acquired at the mono-, bi- and three-layer segments. The PL exhibits two peaks, corresponding to direct excitonic transitions at the Brillouin zone K and K′ points of MoS_2. These excitations are usually denoted as A and B exctions. The energy difference of the two resonances is due to the spin-orbital splitting of the valence band. The circle markers represent the measured data, whereas the solid lines represent fit to the measured data. The A and B excitons are fitted by two Lorentzians. In comparison with the Raman band intensity dependance on the number of layers, the PL has an opposite trend with increasing the number of layers: thinner segments have larger PL. This quite peculiar behaviour is a direct consequence of the MoS_2 electronic

structure, which is also dependent on the number of layers as explained in Ref. [125]. Namely, in going from the bulk to the mono-layer the MoS_2 transitions from indirect semiconductor (with a valence band maximum at the Brillouin zone Γ point) to a direct semiconductor (with a valence band maximum and conduction band minimum at the the Brillouin zone K point). In particular, the indirect gap becomes larger as the thickness of the sample is reduced until the mono-layer is reached. In case of the mono-layer the indirect gap exceeds the gap at the K point resulting in a drastic improvement of the PL quantum efficiency. The inset in figure 5.5(c), adopted and modified form Ref. [125], shows conduction and valence bands for the bulk, four-, two- and mono-layer MoS_2 and illustrates how the lowermost conduction and the uppermost valence bands of MoS_2 change during the transition from an indirect to a direct semiconductor. The dominant contribution to the total PL has the A excitonic transition, since the intensity of the A peak is stronger and more sensitive to the MoS_2 thickness than the B peak [see the intensity maps in figures 5.6(a) and 5.7(a)].

Further analysis of the plots in figure 5.5(c) suggests that the position and the spectral width of the exciton resonances also depends on the number of layers. A more comprehensive picture on the matter can be inferred from the maps in figures 5.6 and 5.7 [see panels (b) and (c)] which show positions and spectral widths of A and B peaks at every pixel across the considered MoS_2 sample.

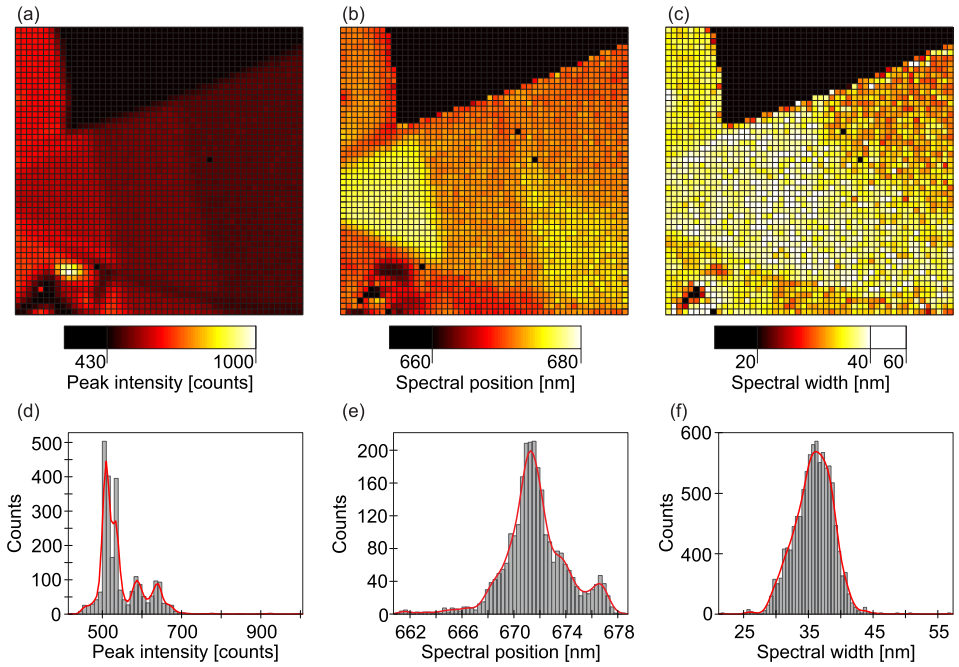

Figure 5.6: Spatially resolved (a) intensity, (b) spectral position and (c) spectral width of the A peak. (d),(e),(f) Corresponding histograms.

For the purpose of more perspicuous presentation the values between the pixels

in these maps are not interpolated. The pixel values are, in fact, parameters extracted from the best fit to the measured data. The black pixels represent either the background (substrate) which has no PL or the parameter values from the lower end of the colorbars, which are located below their corresponding maps.

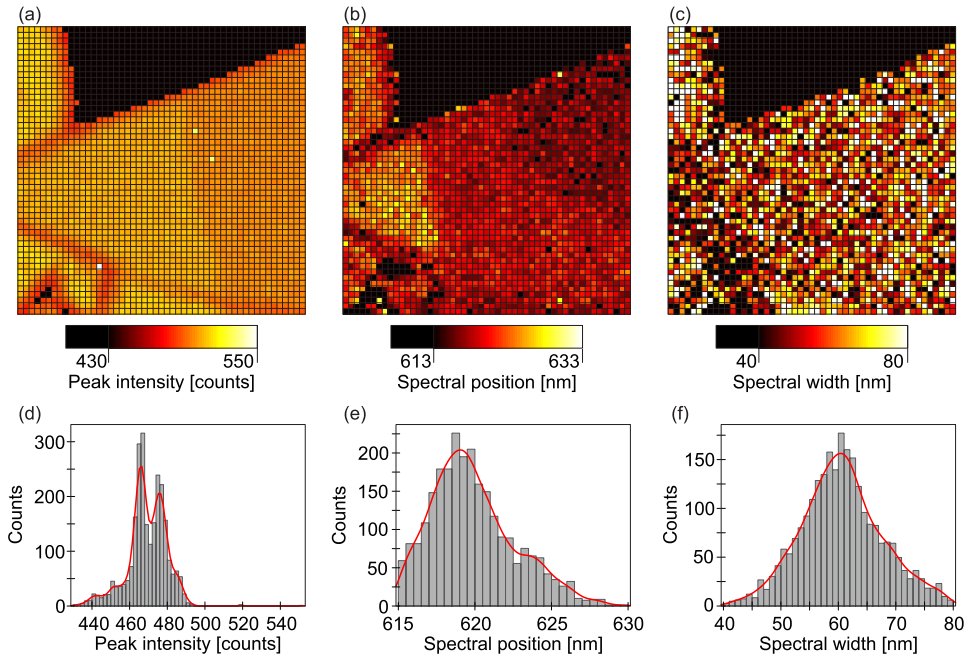

Figure 5.7: Spatially resolved (a) intensity, (b) spectral position and (c) spectral width of the B peak. (d),(e),(f) Corresponding histograms.

By analyzing maps in figures 5.6 and 5.7, we do not observe clear dependance of neither the position nor the spectral width of A and B peaks on the MoS_2 thickness. For example, the A and B peaks within the mono-layer segment seem to be redshifted in comparison to those within the bi-layer segment, whereas the positions of the two peaks in the three-layer segment change within two different areas, one with the relevant values closer to those of the bi-layer and the other with values closer to those of a mono-layer. Also, the position of the A peak in figure 5.6(b) differers even between the monolayer fragments. Similar conclusions can be reached in case of the spectral width for the A peak, with a note that the B peak changes its spectral width erratically across the entire sample. The other samples investigated in this work exhibit similar behaviour [see Appendix B.2] characterised by either random change of the relevant parameters or by having 'areas' within which these parameters do not vary more than a couple of nanometers. Although the initial assumption of thickness dependent position and spectral width of A and B peaks might not be wrong, it is more likely that the parameter variations observed in our samples are induced by contaminants, mechanical deformations or even by the interaction of the sample with the substrate. This observation strongly concurs

with the afore conclusions based on the AFM analysis. As in the case of graphene, optical properties of a few atoms thick MoS_2 are expected to be sensitive even to small perturbations. Fortunately, the intensity of the A and B exciton PL always follows the established thickness dependance, i.e. the thinnest samples have the strongest PL, regardless of small external perturbations.

Below each of the maps in figures 5.6 and 5.7 shown are the corresponding histograms. The intensity histograms are clearly indicative of different intensity areas as they have a couple of distinct peaks corresponding to these areas. The position and spectral width histograms, on the other hand, have a central peak with more or less pronounced shoulders and are, therefore, corroborative of the complex spatial variation of these parameters. Nevertheless, in case of the pristine, thin, exfoliated MoS_2 samples we can expect to find the A peak anywhere in the range between 668-678 nm, and the B peak in the 615-627 nm range with an average width of around 35 nm and 60 nm, respectively.

5.2.2 Influence of Sliver Nanoparticles on The Optical Properties of Thin MoS_2

Having established the connection between the excitons PL intensity and the MoS_2 thickness, and the spectral range within which the excitons PL varies, we proceed further by investigating samples functionalized by metallic nanoparticles. As already noted, spherical and cubical silver nanoparticles are used.

In figure 5.8 shown are are the total averaged PL/Raman intensity maps acquired at MoS_2 before and after addition of spherical citrate-capped silver NPs. The maps are obtained under same experimental conditions. The insets display corresponding optical microscopy images. Comparison of the two maps in panels (a) and (b) reveals a clear difference between the two samples: the functionalized sample has localised, very bright areas at which the collected light signal is greatly enhanced with respect to the surroundings [see the profiles in figure 5.8(c)]. These bright, localised areas correspond to the dark dots observed in the inset of figure 5.8(b), and are commonly referred to as the 'hotspots' in the literature. The dark dots are, in fact, the nanoparticle clusters within which the hotspots are formed. We find that only larger clusters, having the lateral size of around a couple of hundreds of nm (or more), exhibit significant signal enhancements.

Figure 5.9(a) shows a wider area of the MoS_2 sample in figure 5.8(b). Here, however, the values between the adjacent pixels are not interpolated. Below the map, in panel (b) of the same figure, shown are PL/Raman spectra acquired within hotspots of different intensity. Each spectrum in figure 5.9(b) has a number assigned to it, representing a pixel in figure 5.9(a) at which the spectrum is acquired. The

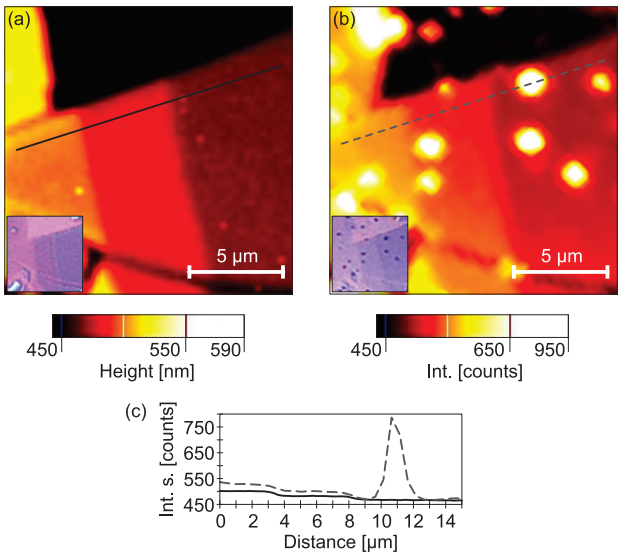

Figure 5.8: PL/Raman map of (a) pristine and (b) functionalized MoS_2. The functionalization is done by depositing citrate anion capped spherical nanoparticles on the surface of the MoS_2. The insets show corresponding optical microscopy images. (c) Profiles taken along the lines in panels (a) and (b).

circle markers are the measured data while the solid lines represent the same data but smoothed by means of SavitzkyGolay method. The seemingly sharp spectral features in 535-650 nm region originate from the citrate anion vibrational modes (the Stokes signal) boosted by means of surface-enhanced Raman scattering (SERS). This becomes evident after comparison of the spectrum obtained at the hotspot on the SiO_2/Si substrate [see curve 5 in figure 5.9(b)] and the one obtained at the hotspot on the MoS_2 sample [see curve 5 in figure 5.9(b)]. As in case of the MoS_2 vibrational bands, due to the 1 nm resolution, the citrate anion SERS bands can not be resolved appropriately. A more detailed analysis of these bands and the SERS effect are presented in Chapter 6. The MoS_2 Raman bands and the B peak are masked by the citrate anion Raman signatures, as the SERS enhancement seems to be the strongest among all the signals in the 535-650 nm region. On the other hand, the A peak is easily distinguished in 650-700 nm region [see curves 1, 2 and 3 in figure 5.9(b)], except in case of high intensity hotspots when it becomes masked by the wide background originating from the NP clusters [see curve 4 in figure 5.9(b)]. The reminder of the MoS_2 sample, i.e. the areas which are not covered by NP clusters, show no significant modification of the luminescence properties when compared to those observed initially, before deposition of the NPs. The A and B peaks can be clearly distinguished at these areas, and their position and spectral width vary within the afore assessed spectral range.

At first glance, the PL/Raman spectra in figure 5.9(b) looks as if all of the constituent signals are simply added together to form the total PL/Raman signal. In

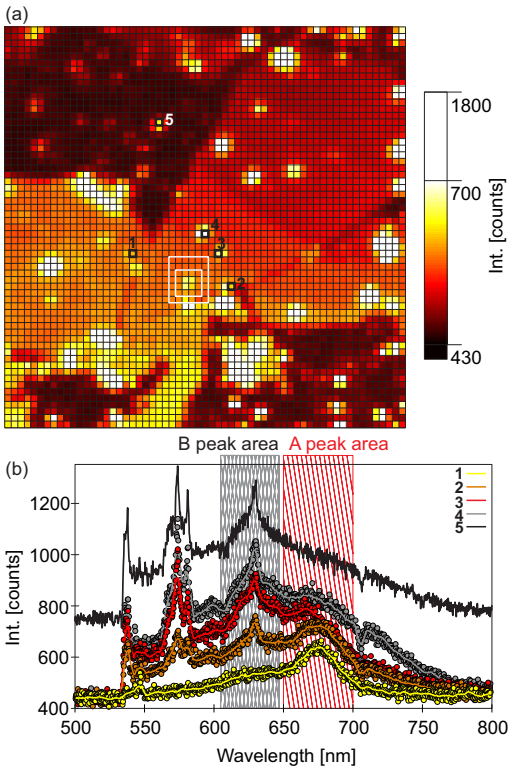

Figure 5.9: (a) PL/Raman map of functionalized MoS_2. The functionalization is done by deposition of citrate anion capped spherical nanoparticles on the surface of the MoS_2. The white squares mark the hotspot and the area around it used in figure 5.11. (b) PL/Raman spectra acquired at the numbered pixels. Circle markers represent the measured data, while solid lines represent the Savitzky–Golay filtered data. Exception is curve 5, representing a spectrum acquired at the hotspot on the SiO_2 surface, which is not filtered/smoothed. The initial level of this curve is risen for better visibility.

order to investigate whether or not the MoS_2 PL is enhanced/modified, we performed a tedious analysis of the hotspots within numerous samples. Due to the interference of citrate anion SERS bands, the enhancement / modification of the B peak is left out of the analysis and only the A peak will be further investigated. In the initial step an area around the selected hotspot is chosen. The area includes a few additional pixels around the hotspot at which the acquired luminescence signal is unperturbed by the NPs. The additional pixel having the lowest A exciton luminescence and the spectral position closest to 673 nm (which is a value in the middle of 668-678 nm range) is chosen as the referent one. The change in the spectral position of the A peak and its enhancement within the hotspot are evaluated with respect to the A peak acquired at the referent pixel. The change in the spectral position of the A peak is defined as $\Delta\lambda = \lambda_{hotspot} - \lambda_{ref}$, where $\lambda_{hotspot}$ and λ_{ref} represent wavelengths of the A peak at the hotspot and at the referent pixel, respectively [see figure 5.10]. The enhancement, F, is defined as the relative intensity ratio of the enhanced and reference A peak [see figure 5.10]. Relative intensity is the intensity evaluated with

respect to the lowest background value. The hotspots located on the border between two MoS_2 segments of different thickness are omitted from the analysis since it is practically impossible to determine the border between the two segments within the hotspots. Finally, the analysis is done for both smoothed and fitted data, where the fitting is realized by three Lorentzians, two acting as the NP background and the B peak, and the other acting as the A peak [see figure 5.10]. The SERS features do not tamper with the total background since they originate from completely different (nonlinear) scattering process. Therefore, the SERS bands, which are much more spectrally narrower than both the NPs background and the B peak, are simply added to the total signal. Furthermore, they are not relevant for the luminescence enhancement mechanism and are, consequently, excluded from the fitting procedure. It should be noted, however, that strong NPs background signal is usually, but not exclusively, followed by strong SERS signal.

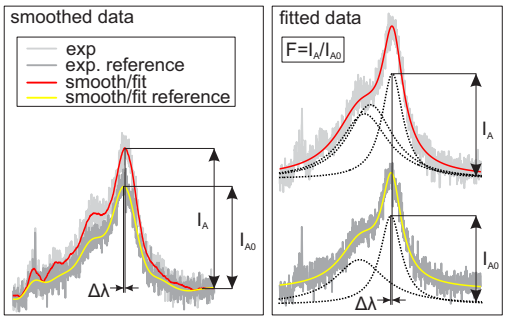

Figure 5.10: Illustration of how $\Delta\lambda$ and F are evaluated using both smoothed and fitted data.

Panels (a) and (b) in figure 5.11 show the spatial variation of the $\Delta\lambda$ and F within the area marked in figure 5.9 by a larger white square. In particular, results shown in panel (a) are based on processing smoothed curves while panel (b) shows results obtained from the fitted curves. Below the $\Delta\lambda$ and F maps, in each panel, shown are spectra collected at pixels bordered by the white square (it represents the actual hotspot area) in the corresponding maps (in figure 5.9 these pixels are bordered by a white square located within the larger white square). The spectra acquired at the bordered pixels are drawn using the light gray markers. The red curve going through these markers is either a smoothed curve [see panel (a)] or a fitted curve [see panel (b)]. The reference spectrum and its smoothed/fitted curves are plotted using dark gray markers and yellow solid lines, respectively.

The $\Delta\lambda$ maps in figure 5.11 show that the NPs do not affect the position of the A peak more than the existence of mechanical deformations, residues or the interaction with the substrate, since the NPs induced A peak's position variations fall in the afore assessed 668-678 nm spectral range. This conclusion holds for the other hotspots at the other MoS_2 segments within the same sample, as well as for

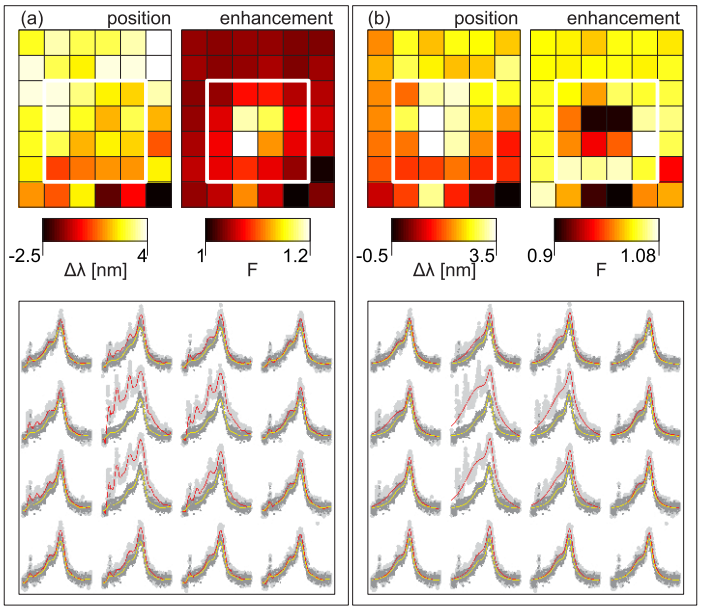

Figure 5.11: (a) The $\Delta\lambda$ and F maps of the area bordered by the white squares in figure 5.9(a). These maps are derived from the smoothed/filtered data as illustrated in the left panel in figure 5.10. Below the maps shown are the spectra (light gray markers) acquired at pixels which are bordered by the white square in the related $\Delta\lambda$ and F maps. Additionally, with each of the mentioned spectra plotted is the reference spectrum (dark gray markers). Red/yellow solid lines represent the smoothed/filttered data. (b) The $\Delta\lambda$ and F maps of the same area, but derived from the fitted data as illustrated in the left panel in figure 5.10. Below the maps shown are the spectra (light gray markers) acquired at pixels which are bordered by the white square in the related $\Delta\lambda$ and F maps. Additionally, with each of the mentioned spectra plotted is the reference spectrum (dark gray markers). Red/yellow solid lines represent fits.

all the investigated samples.

On the other hand, the enhancement map if figure 5.11(a) reveals maximal A peak enhancement of about 1.2. However, analysis based on the smoothed data neglects the existence of the NPs background which is ought to mix with the excitons luminescence. Upon inclusion of the background, in the manner explained earlier and illustrated in figure 5.10, maximal A peak enhancement of 1.08 is achievable as it can be seen from the enhancement map in figure 5.11(b). The pixel at which the maximal enhancement observed is located within the hotspot (the area bordered by the white square in the related map), but not at pixels which exhibit the highest intensity. At these pixels, the dominant contribution to the total signal have the NPs background and the SERS signals. When strong enough the NPs background signal masks the A exciton PL, as documented by enhancement values smaller than 1. In some cases, as it can be seen in the Appendix B.2 and later in figure 5.12(b), the NPs background can be so strong that the fitting procedure becomes corrupted and, therefore, not reliable.

Additionally, MoS_2 samples funcitonalized by cubical PVP-capped silver NPs behave similarly as the samples having spherical NPs on their surface: the B excitonic peak is masked by the SERS features, while the A excitonic peak is visible when the hotspots are not so intensive [see figures 5.12(a) and 5.12(b)]. In this case, however, sharp spectral features in 535-650 nm region [see the spectra in figure 5.12(b)] originate from the SERS enhanced PVP vibrational modes. In addition, the hotspots within clusters formed of cubical NPs exhibit a few times stronger intensity than hotspots within clusters formed of spherical nanoparticles.

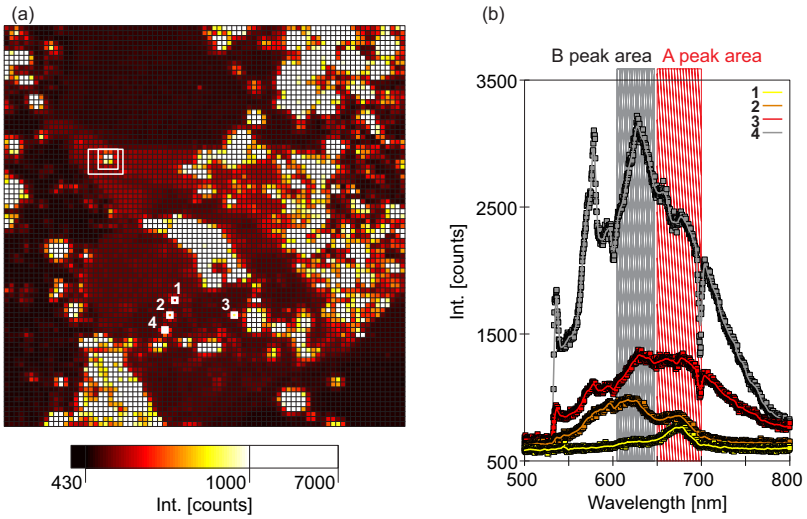

Figure 5.12: a) PL/Raman map of functionalized MoS_2. The functionalization is done by deposition of PVP capped cubical nanoparticles on the surface of the MoS_2. The white squares mark the hotspot and the area around it used in figure 5.13. (b) PL/Raman spectra acquired at the numbered pixels. Circle markers represent the measured data, while solid lines represent the Savitzky–Golay filtered data.

Examination of the individual hotspots leads to conclusions similar to those reached in case of spherical nanoparticles. Figure 5.13 shows that the position of the A peak does not change significantly upon introduction of the cubical NPs. The enhancement achievable by cubical NPs does not exceed factor of 1.4, which is a value slightly higher than the one attainable with spherical NPs.

In order to explain the fairly weak enhancement observed in the experiment a simple, qualitative model is employed. As explained earlier, this model describes NP clusters on a non-absorbing substrate. In particular, the NP clusters consisting of either eight spherical or eight cubical NPs will be investigated. The diameter of spherical NPs is set to $2a$=25 nm in order to match the average diameter assessed from SEM images. The nano-cubes have the size of about a=40 nm, corresponding to the average value extracted also from SEM images. The distance between the spherical NPs in the cluster is set to d=1.2 nm, see figure 5.14(a). In case of the nano-cubes, d is defined as the distance between the outer surface of the spheres in

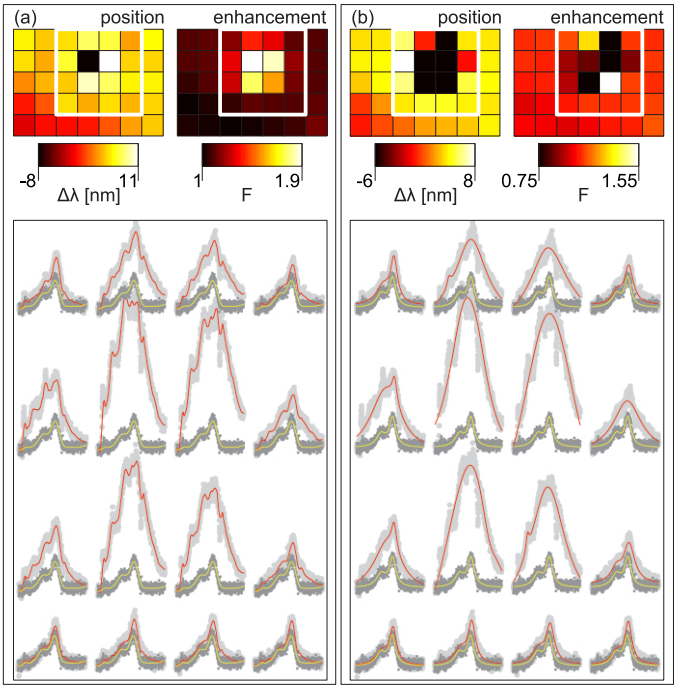

Figure 5.13: (a) The $\Delta\lambda$ and F maps of the area bordered by the white squares in figure 5.12(a). These maps are derived from the smoothed/filtered data as illustrated in the left panel in figure 5.10. Below the maps shown are the spectra (light gray markers) acquired at pixels which are bordered by the white square in the related $\Delta\lambda$ and F maps. Additionally, with each of the mentioned spectra plotted is the reference spectrum (dark gray markers). Red/yellow solid lines represent the smoothed/filttered data. (b) The $\Delta\lambda$ and F maps of the same area, but derived from the fitted data as illustrated in the left panel in figure 5.10. Below the maps shown are the spectra (light gray markers) acquired at pixels which are bordered by the white square in the related $\Delta\lambda$ and F maps. Additionally, with each of the mentioned spectra plotted is the reference spectrum (dark gray markers). Red/yellow solid lines represent fits.

which the nano-cubes are inscribed, see figure 5.14(b). Defining the d in this way enables the in-plane rotation of individual nano-cubes, as it prevents crossing of the nano-cube edges. This additional degree of freedom renders the simulations more realistic as the orientation of the cubes on the substrate is also random.

Figure 5.14 shows the extinction cross section (dotted lines) and the average intensity enhancement (solid lines) of two NP clusters, one consisting of spherical NPs and the other consisting of cubical NPs. The incident electric field is polarized in the plane of the page, as drawn in figure 5.14. The two clusters have the same topology, as it can be seen from the sketches in figure 5.14. The peaks observed in the extinction cross section correspond to the clusters LSP modes. The position of these peaks, as well as the overall shape of the extinction curves, depends on the topology of the cluster and on the number of the NPs within the cluster [see the Appendix B.2]. The average intensity enhancement peaks are located in the

vicinity of the LSP modes. Therefore the strongest enhancement is to be found close to or at the LSP resonances. Below the extinction cross section/enhancement curves in both panels in figure 5.14 displayed are the total electric field distributions calculated at the resonant and non resonant wavelengths. The electric fields at the LSP resonances are obviously stronger than the electric fields calculated for the non-resonant case. In any case, the electric fields are strongly localized in small volumes in between closely spaced NPs regardless of their shape. It is within these volumes where the maximal enhancement is expected. However, the electric fields are also distributed over the entire cluster surface and in its vicinity.

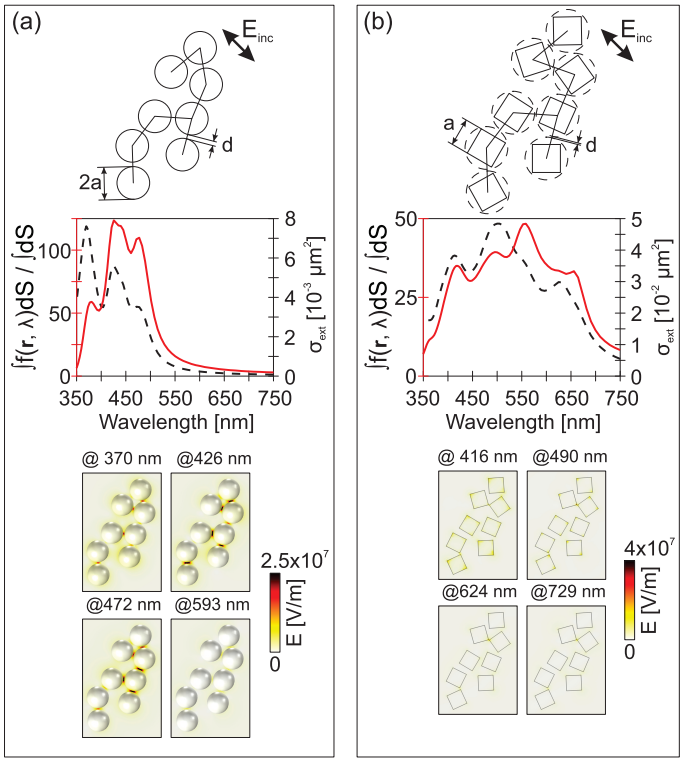

Figure 5.14: The average intensity enhancement (solid red lines) and the extinction cross section (dotted black lines), σ_{ext}, of (a) a cluster consisting of eight spherical nanoparticles and (b) of a cluster consisting of eight cubical nanoparticles. The clusters' topology is illustrated in the upper part of the respective panels. The incident field is polarized in the plane of the page. λ_{inc} =532 nm.

The fact that the NP clusters lie on top of the MoS_2 sample renders the fraction of the electric field closest to the MoS_2 sample as the main contributor to the enhancement of the MoS_2 excitons' PL. Figures 5.15(a.i) and 5.15(b.i) show the integrals of the intensity enhancement over different parts of the clusters surface. These parts are marked by S1 and S2, and textured by gray (orange and red) color in the corresponding illustrations of the clusters. S1 represents the nano-gap areas, whereas the S2 represents the cluster surface parts which are in touch with or in the vicinity of the substrate surface. Both the total electric field (solid lines) and

its normal component (dotted lines) are included in the analysis. Obviously, the smallest contribution to the total intensity enhancement has the S2 surface area, whereas, as expected, the dominant contribution comes from the S1 surface area. By analysing figures 5.15(a.iii) and 5.15(b.iii), in which the ratio of the integrals over the defined surface parts (S1, S2) and the total cluster surface is plotted, we find that the intensity enhancement originating from the S2 surface area has a contribution of around 10-20 % (depending on the nanoparticles shape) to the total intensity enhancement, in the whole spectral range. That being said, the small MoS_2 PL enhancement and strong SERS signal (form either citrate anions or PVP) observed in the experiments is certainly due to the way the electric field is distributed within the cluster. A more complete interpretation, however, is more complex given the specific properties of the MoS_2 excitons. Namely, the MoS_2 is a two dimensional system in which all kind of excitations are contained within its plane. Specifically, the considered A and B excitons are acting as the in-plane electric dipoles emitting radiation out of the MoS_2 plane [126]. Consequently, the MoS_2 responds only to the incident electric fileds parallel to its plane. Therefore, the orientation of the NP clusters' electric fields with respect to the MoS_2 sample has a more crucial role in the enhancement of the MoS_2 PL than the actual field intensity.

Upon separation of the total electric field into components, normal and tangential to the cluster surface, it becomes clear that the enhancement of the MoS_2 PL is completely governed by the tangential field component. By comparing the dotted and solid curves of the same color in figures 5.15(a.i) and 5.15(b.i), or rather by examining their ratio in figures 5.15(a.iv) and 5.15(b.iv), one can conjecture that the normal field component has the dominant contribution to the average intensity enhancement. The contribution of the normal filed component to the intensity enhancement is more significant in case of the spherical NPs, as it reaches more than 90% at longer wavelengths. This is corroborated by the electric field vector plots in figure 5.15(a.ii). Therefore, the small fraction of the intensity enhancement over the S2 surface area with an even smaller contribution of the tangential field component leads to the small enhancement [1-1.2, see the Appendix B.2] of the PL A peak. Similar conclusion can be reached for the nano-cubes [see figures 5.15(a.ii) and 5.15(a.iv)]. In this case, however, the fraction of intensity enhancement over the S2 surface area, as well as the contribution of the tangential field component to it, is slightly higher than the one observed in case of spherical NPs. Hence, the nano-cube clusters yield a slightly higher enhancement of the A peak (1-1.55) in the experiment than the nano-sphere clusters.

Obviously, the nanoclusters are not efficient for neither modification nor enhancement of the MoS_2 PL due to two important facts: (i) the electric fields are the strongest within the nano-gaps and (ii) the tangential filed components are very

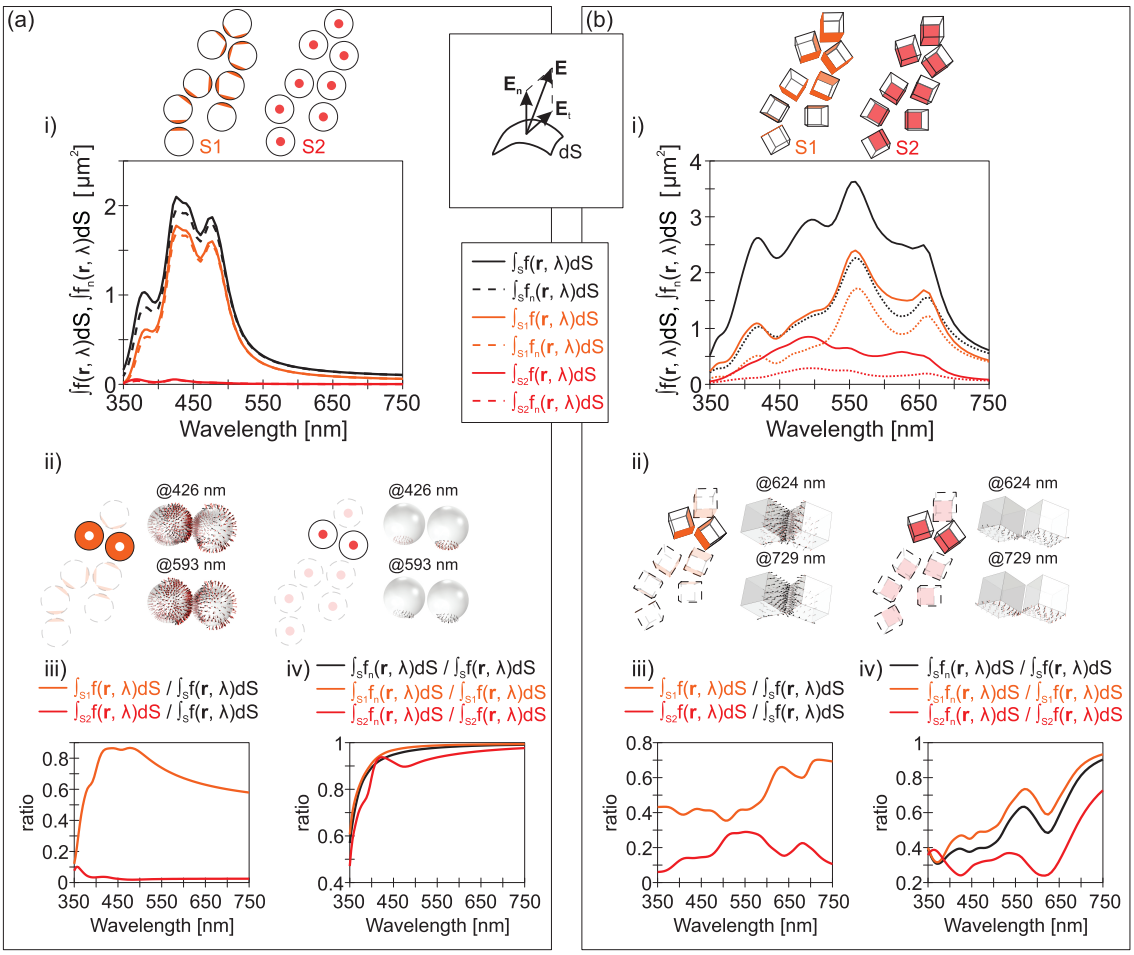

Figure 5.15: (a.i), (b.i) Wavelength dependent integrals of the intensity enhancement, f and f_{n}, taken over the entire cluster surface and its parts, S1 and S2. S1 and S2 are clearly marked in the sketches of the related clusters. f stands for the intensity enhancement calculated using the total field, while f_{n} stands for the intensity enhancement calculated using just the normal component of the total field. λ_{inc} =532 nm. (a.ii), (b.ii) Total electric field vector (black arrows) and its normal (red arrows) and tangential (gray arrows) components. Two nanoparticles are picked from the cluster (the other particles exist but are hidden), as it is illustrated in the corresponding sketches for better visibility of the fields. Two wavelengths are analysed, one representing the resonant and the other representing the non-resonant case. (a.iii), (b.iii) ratio of the integral of f taken over the S1(S2) surface and the entire cluster surface. (a.iv), (b.iv) ratio of the f_{n} and f integrals which are taken over S1, S2, and the entire cluster surface.

small in comparison with their normal counterparts. Moreover, change of the cluster topology or its size does not improve the PL enhancement factor significantly, as seen from the experiments, even though such changes are ought to redshift the LPS resonances thus improving the average SERS enhancement at longer wavelengths. This is simply corroborated by the afore presented wavelength dependent analysis of the intensity enhancement. In fact, the NP clusters are more efficient for SERS studies of analytes located exactly in the nano-gaps [see Chapter 6].

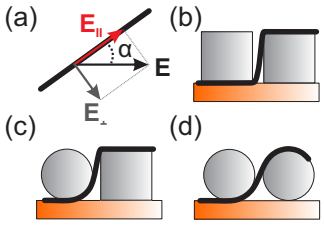

Figure 5.16: (a) Illustration of the electric field **E** projection on the MoS_2 plane. (b), (c), (d) Possible configurations for improving the enhancement of the MoS_2 photoluminescence.

Having in mind that the nano-gaps represent the regions of interest, one can utilize geometries shown in figure 5.16 or structures suggested in the literature [127] in order to improve the PL enhancement. As it can be seen in figures 5.15(a.ii) and 5.15(b.ii), the total electric field within the nano-gaps is mainly normal to the surface of the NPs (i.e. the enhancement is dominated by the normal field component). This can be inferred from figures 5.15(a.i), 5.15(a.iv), 5.15(b.i) and 5.15(a.iv) as well. Therefore, a significant enhancement improvement can be achieved by exploiting the projection of the enormous gap fields on the MoS_2 [see figure 5.16(a)], which is pinched under an angle between two closely spaced NPs. The configurations shown in figure 5.16 are experimentally achievable. The fabrication of such systems would involve the following steps: (i) deposition of single NPs on a arbitrary surface, (ii) transfer/exfoliation of the MoS_2 over the NPs, (iii) second deposition of the NPs over the MoS_2, (iv) repositioning of the secondary particles by the AFM. Additionally, the unwanted SERS signal can be easily removed by using an excitation at a shorter wavelength.

5.3 Conclusion

To summarize, in the first part of this study we have investigated pristine MoS_2 samples by combination of AFM, Raman spectroscopy and PL spectroscopy. Similarly, as in case of graphene we have found that both AFM and Raman spectroscopy techniques are necessary for the unambiguous determination of the MoS_2 number of layers. Further analysis of the AFM topographs has shown that MoS_2 samples are not perfect. These imperfections, which are presumably a consequence of the fabrication procedure, lead to the uncontrolled variations of both the spectral position and spectral width of excitonic A and B PL peaks.

In the second part of this study we have investigated MoS_2 samples covered by metallic nano-particle clusters. By analysing the PL of functionalized MoS_2 samples, we have not observed significant PL modifications. In fact, the spatial variations of the position and spectral width of the PL peaks are kept within the initial variation

range upon introduction of the spherical and cubical NP clusters. Moreover, the NP clusters turned out to be rather inefficient 'enhancers' of the MoS_2 PL, with the enhancement factors in 1-1.55 range. In principal, the size and shape of the clusters have no significant effect on the PL enhancement factors, as evidenced by slightly values observed in case of clustered cubes than in case of clustered spheres. The additional analysis based on rigorous numerical simulations of plane wave scattering on NP clusters has shown that the distribution and the orientation of the clusters' electric fields with respect to the MoS_2 are key factors which determine the coupling efficiency. The largest electric field values are observed within the nano-gaps between the NPs in a cluster, and the field becomes weaker as one approaches the bottom part of the cluster which is facing the MoS_2, thus, reducing the intensity enhancement. However, we have found that even more important factor is, in fact, the orientation of the NPs electric field with respect to the MoS_2 plane, since only the electric fields parallel to the MoS_2 surface are capable of enhancing the MoS_2 PL. Our simulations show that in middle-sized clusters, composed of either nano-spheres or nano-cubes, the total electric field has large normal and weak tangential components at and in the vicinity of the clusters' surface, thus, ultimately leading to small PL enhancement factors. In addition, we have proposed an alternative way for improving the enhancement factors, based on exploiting intensive fields within the NPs nano-gaps.

Chapter 6 Application of surface plasmons and highly localised electromagnetic fields in SERS study of metal-dye complexes

Dye coated metallic NPs exhibit interesting optical properties provided by the interaction between the metal core and dye shell. Depending on the interaction mechanism between the two, the optical properties of dye molecules and NPs can be changed separately or jointly within the adsorbate-NP complex [128]. For example, NP plasmonic frequencies can be changed due the presence of adsorbate or dye fluorescence can be quenched/enhanced by the influence of the NP [129; 130]. Ultimately, under special conditions, these complexes can exhibit unique characteristics different than those of either isolated dye molecules or NPs. Owing to the variety of mechanisms by which dyes can interact with metalic NPs, dye-NP complexes can lead to applications ranging from nanoscale sensing [131] to advanced composite materials for novel active and nonlinear optical devices [132]. A necessary condition for the two constituents to interact is that the dye molecules must be very close to the surface of the NPs, or ideally adsorbed on it. Therefore, the adsorption process plays one of the key roles in these systems.

In view of the significance of the dye-to-NP adsorption mechanism, in this chapter the mechanism of TC dye adsorption on the surface of Ag NP clusters with citrate ion stabilization is investigated by the SERS technique.

6.1 Materials and Methods

6.1.1 Sample Fabrication and Experimental Methods

Colloids were prepared by reduction of $AgNO_3$ using a procedure described in Ref. [112], which yields nearly spherical citrate capped Ag NP. Scanning electron micrograph in figure 6.1(a) provides the insight on the overall shape and the size of the NPs and how they arrange upon deposition on HOPG. The NPs have a broad size distribution, with diameters ranging from few nm to a hundred nm (the average diameter is around 10 nm), and tend to form clusters of various sizes when drop-cast on the HOPG substrate. For our study we use highly concentrated colloid

dispersion of Ag NPs, n_{Ag}=16 nM which certainly promotes formation of larger NP clusters upon deposition on a substrate. Clustered NPs are essential since they yield high, distinctive SERS signals as it will be shown latter. Plotted in figure 6.1 (b) are the absorbance spectra of two colloid dispersions having $0.2n_{Ag}$=3 nM (black dashed curve) and n_{Ag}=16 nM (black solid curve) of NPs. The colloid dispersion with lower concentration exhibits an absorbance centered at the wavelength which corresponds to the dipolar surface plasmon resonance of a spherical NP with 10 nm diameter. [112; 133]. The absorbance of the colloid dispersion with n_{Ag}=16 nM of NPs has a different shape due to the fact that the concentration of the NPs is extremely high. The absorbance broadening, in both cases can be explained in terms of the radiative losses as well as in terms of the broad distribution of size and shape of the NPs.

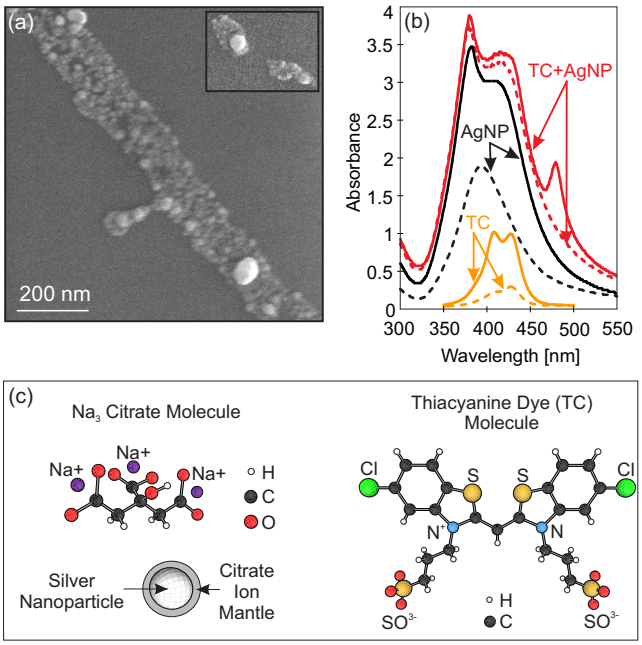

Figure 6.1: (a) Scanning electron micrograph of silver NPs drop-cast on the surface of HOPG. The inset shows an individual NP cluster. (b) Absorbances of: (i) the colloid disperstions having 3 nM (dashed black curve) and 16 nM (solid black curve) of NP, (ii) the TC dye solutions having 5 μM (dashed orange curve) and 25 μM (solid orange curve) of TC, (iii) the TC dye-NP mixtures having the same concentration of the NPs of 16 nM and different concentrations of the TC dye: 5 μM (dashed red curve) and 25 μM (solid red curve). (c) The Na_3 citrate molecule, sketch of an isolated silver NP surrounded by citrate ions and the TC dye molecule.

Thiacyanine dye (5,5' - disulfopropyl-3,3'-dichloro-thiacyanine sodium salt, TC) was purchased from Hayashibara Biochemical Laboratories, Okayama, Japan. Sketch of a TC dye molecule is shown in figure 6.1(c). Aqueous TC stock solution with n_{TC}=50 μM of TC and 1 mM of KCl was prepared by dissolving the solid TC in water and adding KCl afterwards. Water purified with a Millipore Milli-Q water system was used in all cases. The absorbance curves with $0.1n_{TC}$=5 μM

(dashed orange curve) and $0.5n_{\mathrm{TC}}$=25 μM (solid orange curve) of TC, displayed in figure 6.1(b), show two characteristic peaks, one at 428 nm and the other at 409 nm, belonging to the dye monomers and dimers, respectively [134]. Increasing the concentration of either TC or KCl, or both above a certain value would result in a TC molecular stacking, known as the J-aggregation, recognizable by appearance of a new peak at 464 nm in the absorbance [112].

The colloid and the TC dye solutions are mixed so that the afore chosen concentrations of the two ingredients are kept in the final solution. Figure 6.1(b) shows the absorbance spectra of two solutions with different concentrations of the TC dye: (i) $0.1n_{\mathrm{TC}}$=5 μM (dashed orange curve) and (ii) $0.5n_{\mathrm{TC}}$=25 μM (solid orange curve), and the same concentration of the NP: n_{Ag}=15 nM. Apart from being reminiscent of the absorbance curve belonging to the highly concentrated colloid dispersion, the $0.5n_{\mathrm{TC}}$ curve has a peak around 480 nm indicating that the TC dye molecules, or rather their J-aggregates, are adsorbed on the surface of the NPs [112; 134]. On the other hand, the absence of the 480 nm feature in the the $0.1n_{\mathrm{TC}}$ curve suggests that there are no J-aggregates adsorbed on the surface of the NPs.

The final solution, is left overnight and afterwards drop-cast on a freshly cleaved mica surface. Mica has an atomically flat, hydrophilic surface on which the NPs are easily deposited, and a well known Raman spectra. In addition to mica, we use HOPG and SiO_2 surfaces which are hydrophobic and, therefore, allow formation of large, closely spaced NP clusters as well as more efficient aggregation of the TC dye on their surface. In particular, HOPG is used for Raman characterisation of concentrated TC dye, since the dye efficiently aggregates on its surface. The SiO_2 is used for the control study of NPs having dye/borate anions conformed to their surface, since the large closely spaced NP clusters are required for fast Raman/SERS characterisation of the initially unstable borate-capped NPs.

Characterisation of the NPs in the colloid solutions is done by means of spectrophotometry. Absorption spectra of colloidal solutions were measured by Perkin Elmer UV Vis spectrophotometer using the quartz cuvette with 1 cm path length. The assessment of the NPs shape and size is done by analysing SEM measurements which were performed on TESCAN Mira 3 microscope.

Finally, the main experiments are performed in the ambient conditions at room temperature by combining the AFM and Raman techniques. These techniques are done simultaneously thus providing spatially resolved chemical information of the sample along with its surface topography at the same place. In this way one is able to identify and assert the size of the SERS active TC dye coated nanoparticle clusters while obtaining the chemical identity of the analyte adsorbed on the surface of nanoparticles. For Raman spectroscopy and SERS measurements a linearly polarized semiconductor laser operating at a wavelength of 532 nm is used. The ex-

periments are performed using commercial NTegra Spectra system from NT-MDT.

6.1.2 Numerical Methods

To numerically solve the classical Maxwell equations we have used the finite element method implemented within the Comsol Multiphysics software package [45]. We analyse clusters of Ag NPs having a diameter of 10 nm on a substrate under plane wave illumination. The silver dielectric constant is taken from Rakic et al. [116]. The substrate is assumed to be semi-infinite and isotropic with a dielectric constant of 2.25, which roughly corresponds to the dielectric constants of both mica and SiO_2 at visible frequencies. The surrounding medium is vacuum and its dielectric constant is 1. For purposes of efficient meshing, the NPs are assumed to lie 1 nm above the substrate. The clusters are formed in the plane which is parallel to the substrate by allowing the NPs to have random position but under the following conditions: (i) the minimal allowed distance between adjacent NPs is d=0.8 nm, (ii) every NP must be at 0.8 nm distance form at least one neighbouring nanoparticle. By imposing the afore conditions we were able to achieve various cluster geometries and mimic the lack of control over the clusters morphology in the experiment.

The absorption, scattering and extinction cross sections are calculated as a function of the excitation wavelength, λ, utilizing general expressions provided in Ref. [117]. The intensity enhancement and the enhancement of the Raman signal are assessed using $f(\lambda) = |\mathbf{E}(\lambda)|^2/|\mathbf{E}_0(\lambda)|^2$ and $F(\lambda_{inc}, \lambda) = f(\lambda_{inc}) \times f(\lambda)$ [135], respectively. Here, λ_{inc}, $|\mathbf{E}|$, $|\mathbf{E}_0|$ are the incident laser wavelength, the total scattered field and the incident field amplitudes, respectively. The average Raman enhancement is further estimated by integration of the Raman enhancement over the NP cluster surface which is followed by normalization of the obtained result to the surface area of the NP cluster.

6.2 Results and discussion

6.2.1 Raman spectroscopy of TC dye, mica and Si

Figure 6.2 shows Raman spectra of the dye powder, highly concentrated dye solution which is drop-cast on freshly cleaved HOPG. Three distinct frequency regions, I, II and III, containing the TC dye Raman bands are highlighted by gray (yellow) markers. Dividing the entire spectral region into parts, hereinafter, allows for a more systematic comparison of the TC dye Raman spectra with the other relevant Raman spectra.

The TC powder and the drop-cast TC dye have very similar Raman signatures, with a few subtle diversities. Namely, in region I at around 600 cm^{-1} the TC powder

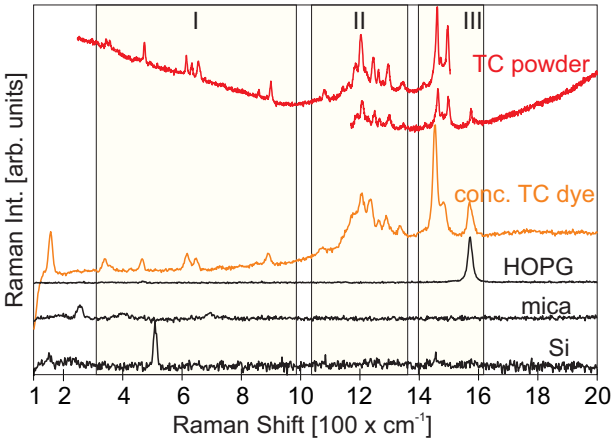

Figure 6.2: Raman spectra of: (i) TC dye powder, (ii) TC dye which is drop-cast on HOPG, (iii) HOPG and (iv) mica, (v) Si having a 300 nm thick layer of thermally grown SiO_2. The excitation laser wavelength is 532 nm.

has three Raman bands whereas the drop-cast concentrated TC dye has two. On the other hand, the Raman bands of the concentrated dye are Comparison of the Raman bands located between 1400 cm^{-1} and 1500 cm^{-1} in region III reveals yet another mismatch. Lastly, the two dye variants have a different background under the same excitation wavelength - this suggest that the TC dye powder may have a slightly different molecular stacking than the drop-cast one [136].

Nevertheless, the Raman spectra of the two TC dye variants can be easily distinguished from the Raman spectra belonging to either mica or SiO_2/Si, whereas the HOPG has only one strong band, located in region III around 1577 cm^{-1}, overlapping a relevant dye mode. In case of the highly concentrated TC dye the overlapping of the two bands does not represent an issue, since the formed dye layers are large and thick enough to diminish the contribution of the HOPG band. Oppositely, in the case of the SERS measurements the strong HOPG band can be easily mistaken for the dye band when the dye spectra is weakly enhanced. The Raman spectra of the SiO_2/Si substrate has two characteristic Si Raman bands in the considered spectral region. However only one, at 523 cm^{-1}, is visible under the measurement conditions (532 nm laser with power density of 200 $\mu W/\mu m^2$) which are used for the SERS measurements. The visible Si band does not overlap any of the relevant dye bands.

6.2.2 Surface enhanced Raman spectroscopy of pristine Ag nanoparticles

Figure 6.3 (a) shows an AFM topograph of the pristine Ag NP clusters on mica surface. The corresponding Raman map is shown in figure 6.3 (b). The intensity of every pixel in the Raman map is obtained by dividing the sum of Raman intensities

across the entire spectral range (100 - 2000 cm^{-1}) with the number of spectral points. The colorbar in panel (b) is, thus, in counts. Bright areas in figure 6.3(b) represent the regions of enhanced signal, i.e. the 'hotspots'. These regions are located within the clusters consisting of a large number of NP (with diameters in the 10-50 nm range), as it can be seen by comparing the Raman map with the AFM topography image. In fact, we find that the hot spots are dominantly formed within larger clusters, such as those in figure 6.3(a), regardless of the substrate which is used (mica or HOPG).

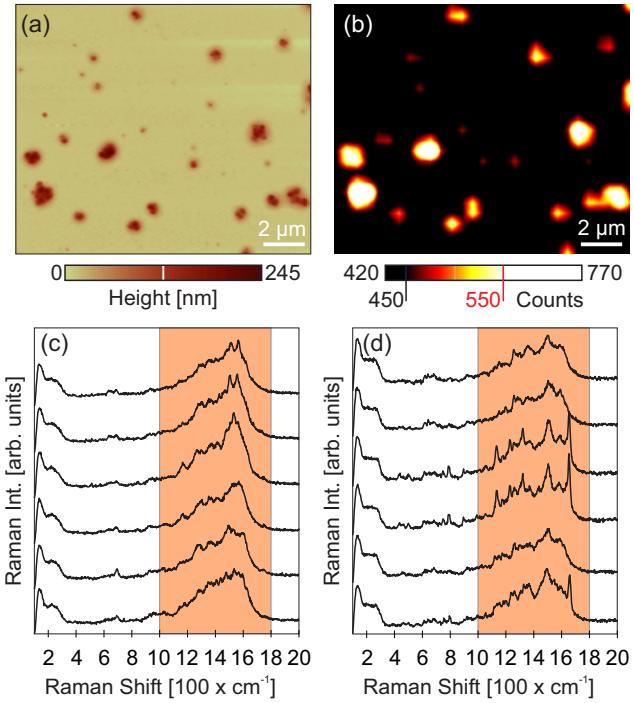

Figure 6.3: (a) AFM topograph of pristine Ag NP clusters which are drop-cast of mica. (b) Corresponding Raman map. (c), (d) Typical SERS spectra acquired within two hot spots in panel (b). The spectra were measured consecutively with 40 s time step. The excitation laser wavelength is 532 nm.

Figures 6.3(d) and 6.3(e) show consecutively acquired spectra with 40 s time step at two hot spots from figure 6.3(b) using 532 nm laser with power density of ≈200 $\mu W/\mu m^2$. As it can be noted, the spectra in panel (c) and (d) seem to be similar, but can not be quantitatively compared. Ironically, beside the wide background which spreads over the entire spectral range, the other common property: pronounced band blinking in the 1000 cm^{-1}-1800 cm^{-1} range (orange region), hinders any kind of quantitative analysis. However, the NP clusters have citrate anions conformed to their surface. Therefore, we assume that the blinking spectra is in fact the SERS signal from the citrate anion mantle, whereas the wide background exists due to the luminescence of the NP clusters.

In order to examine the origin of the hotspots and to assess the signal enhance-

ment, we will analyse a cluster consisting of 20 Ag NPs which is shown in figure 6.4 (a). NPs which are at 0.8 nm distance from their nearest neighbours are connected by a solid (red) lines. The extinction cross-section of the NP cluster in panel (a) is plotted in figure 6.4 (b), as a function of the incident wavelength. For the considered cluster, the scattering cross-section is negligible with respect to the absorption cross-section and therefore the extinction cross-section is approximately equal to the absorption cross-section. The two peaks observed at 365 nm and 435 nm, are the cluster's surface plasmon resonances (SPRs). At these resonances the electric field is highly localized in the nanogaps between the closest NPs, a fact, inter alia, shown previously [137; 138].

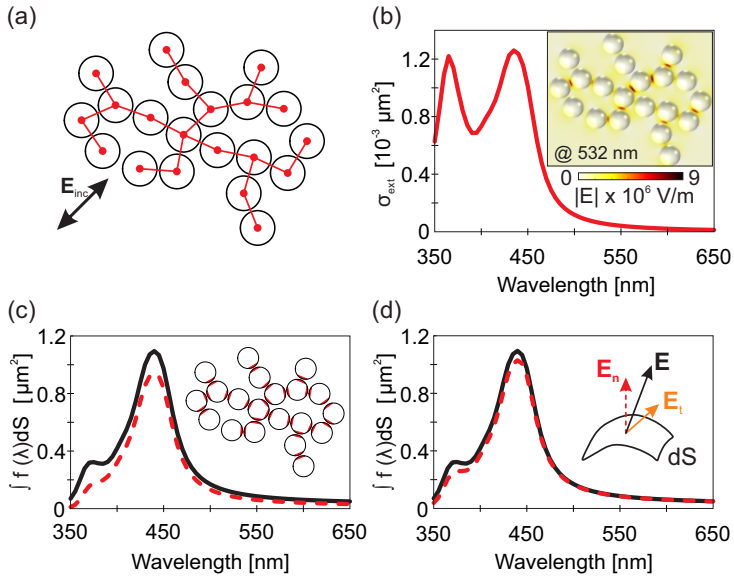

Figure 6.4: (a) Sketch of the geomerty of the cluster. Spheres at a minimal distance of 0.8 nm from each other are connected by (red) lines. The electric filed vector lies in the paper plane, and oriented with respect to the cluster as shown. Normal incidence is assumed. (b) Extinction spectra of the cluster in panel (a) as a function of the wavelength. The inset shows the electric field distribution at 532 nm. (c) Integrals of the intensity enhancement over the entire cluster surface (solid black line) and over the areas of the highly localized field (dashed red line) plotted as the function of the wavelength. The areas of the highly localized field are shaded (colored by red) in the inset. (d) Wavelength dependance of the intensity enhancement integrals of the total filed (solid black line) and it's normal component (dashed red line) which are taken over the entire cluster surface.

On the other hand, the inset in figure 6.4 (a) clearly shows that the electric field remains highly localized in the nanogaps between the closest NPs even for excitation at 532 nm (the wavelength of the laser used in the experiments). In fact, we find this to be the case for all the other wavelengths away from the SPRs. Comparison of the intensity enhancements [see Sec. 6.1.2] integrated over the entire cluster surface and over the areas of highly localized electric field [see figure 6.4 (c) and it's inset], re-

veals that the majority of the enhancement originates exactly from these areas, even for non-resonant excitations. Furthermore, the relevant contribution to the intensity enhancement has the electric field component normal to the cluster surface, as illustrated in figure 6.4 (d). Therefore, the scattered Raman signal would be significantly enhanced when the analyte is located in the nanogaps between closely spaced NPs within a cluster, and consequently these nanogaps represent the hotspots.

For an excitation having a wavelength lower or around the cluster SPRs a large values of the Raman enhancement, on the order of $\sim 10^{11}$, could be achieved. In the case of a moderate sized cluster, such as the one in figure 6.4 (a), we observe the opposite, the SPRs are below the excitation wavelength. However, we also find that increasing the cluster size, simply by addition of new NPs, leads to the overall enlargement of the average Raman enhancement as summarized in figure 6.5 (a). For example, a cluster having 5 NPs exhibits an average Raman enhancements of the order of 10 in the 532-600 nm, whereas a cluster having 20 NPs yields 10 times higher values in the same range. Figure 6.5 (b) illustrates, on the example of an 8 NP cluster, that the average Raman enhancement can be further augmented by decreasing the minimal distance between neighbouring NPs. The lowest considered minimal distance of 0.5 nm yields Raman enhancements as high as 10^4 in the 532-600 nm range. Lastly, by evaluating the average Raman enhancement at the excitation and emission wavelengths of 532 nm and 550 nm, respectively, for a 150 randomly generated 8 NP clusters [see the right side of figure 6.5 (c)] we find that the cluster morphology significantly influences the non-resonant enhancement value. This is corroborated by a wide distribution of the average Raman enhancement shown on the left side of figure 6.5 (c), which vary from 50 to 600. The highest enhancements are observed in chain shaped clusters having the chain axis aligned with the incident electric field, such as the one illustrated in figure 6.5 (c) by filled circles.

The possibility of the resonant enhancement cannot be excluded, since the surface plasmon resonances are seen to redshift in elongated clusters with a larger number of particles that the ones investigated here [137; 138]. However, beside the well elaborated enormous Raman enhancements having a resonant origin [137], we have shown that even in the non-resonant case enhancement factors in the range of $10^2 - 10^3$ can be expected.

6.2.3 Surface enhanced Raman spectroscopy of TC coated Ag nanoparticles

The NPs in the final solution, consisting of the TC dye and Ag NP, may have the J-aggregates or dye monomers or dimers adsorbed on their surface, or even remain pristine. Therefore, it is expected that NP clusters drop-cast from the mixture would

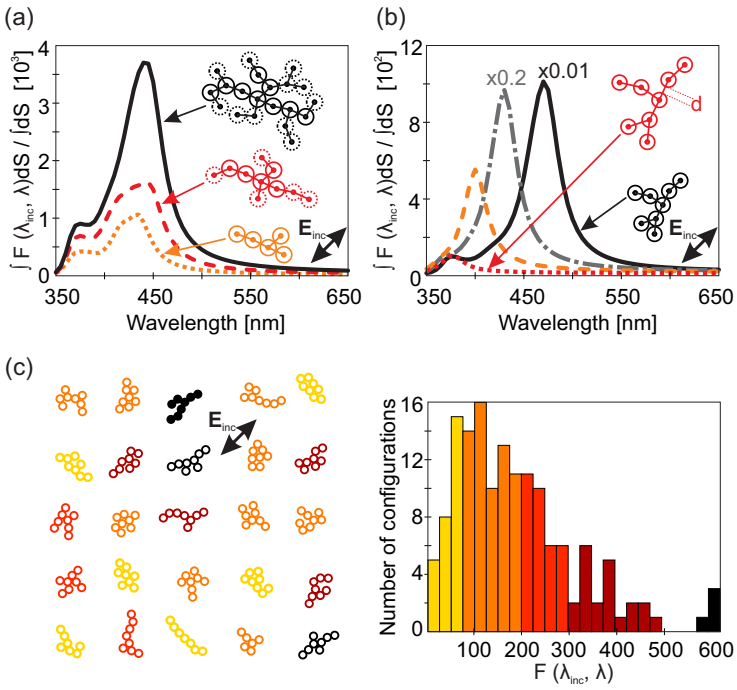

Figure 6.5: (a) The average Raman enhancement calculated as a function of the emission wavelength for clusters having 5 particles (dotted orange line), 10 particles (dashed red line) and 20 particles (solid black line). The clusters are formed starting from the smallest one, with 5 particles, by adding new particles at random positions. Clusters geometry is shown in the inset. Particles connected by lines are at the minimal distance of 0.8 nm from each other. (b) The average Raman enhancement calculated as a function of the emission wavelength for a cluster with 8 particles when the minimal distance between the particles is varied. Particles connected by lines, in the inset, are at the minimal distance d from each other. Solid (black) line corresponds to d=0.5 nm, whereas dash-dotted (gray) line, dashed (orange) line and dotted (red) line correspond to d=1 nm, d=2 nm and d=5 nm, respectively. (c) The right part shows some of the 150 considered cluster variants. All the clusters have 8 particles, with a minimal distance of 0.8 nm. The left part shows a histogram of the average Raman enhancement calculated at the emission wavelength 550 nm for all 150 cluster variants. In all calculations normal incidence at a wavelength 532 nm is assumed. The electric field is polarized in the plane of the paper. Orientation of the electric field with respect to the clusters is shown in all the panels.

have a variety of SERS spectra corresponding to those of different dye conformations, citrate anions and even their combinations. To make a clear distinction between the non-aggregated and aggregated molecules one must have an excitation resonant with the absorption of either aggregated or non-aggregated dye molecules [139; 140]. Here we use a non-resonant laser line at 532 nm which does not allow identification of different dye conformations. However, Ag NP clusters are very efficient enhancers at this wavelength, as it is shown in Sec. 6.2.2 and thus through the SERS effect alone we are able to determine if the TC dye molecules are adsorbed on the NPs or not.

Comparison of the AFM topograph and the corresponding Raman map in figure 6.6(a) and 6.6(b) reveals that the hot spots are located within the larger NP clusters, as in the case of pristine NPs in section 6.2.2. The SERS spectra acquired at these hot spots can be unambiguously categorized in two groups: one featuring stable Raman bands during successive measurements and the other having blinking Raman bands. The wide background from the NP clusters exists in this case as well. Figures 6.6(c), 6.6(d) show the two distinct spectra types. The recording time step is 40 s time step and the laser power density is ≈200 μW/μm^2.

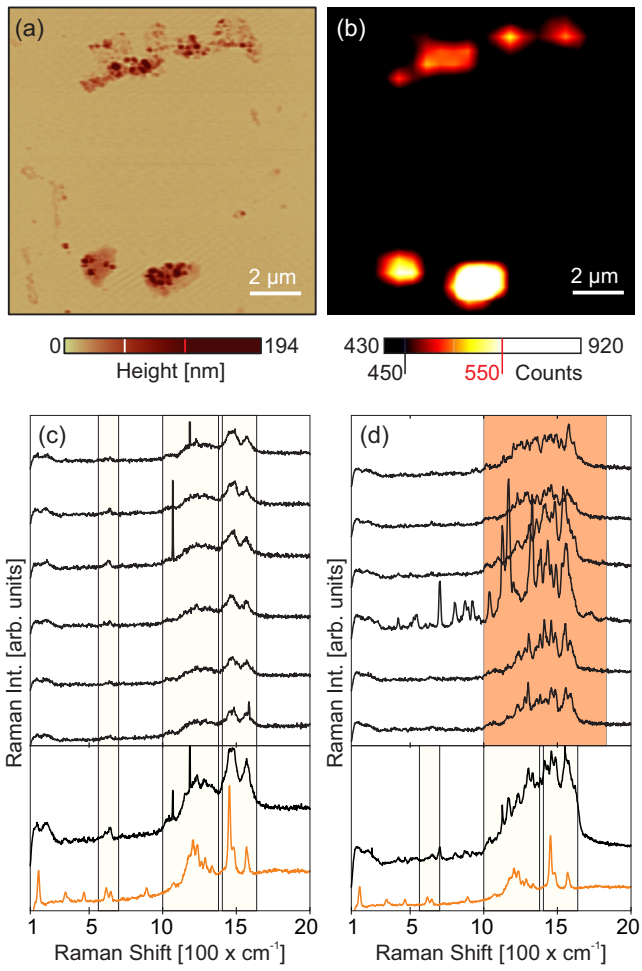

Figure 6.6: (a) AFM topograph of TC dye coated Ag NP clusters which are drop-cast of mica. (b) Corresponding Raman map. (c), (d) Typical SERS spectra acquired within the hot spots, by consecutive measurements with 40 s time step. The excitation laser wavelength is 532 nm. In the lower parts of panels (c) and (d) shown are the SERS spectra obtained by summation of the corresponding consecutively acquired spectra, and the Raman spectra of the drop-cast TC dye.

The consecutively measured SERS spectra having stable Raman bands are reminiscent of the drop-cast TC dye Raman spectrum. The similarity between the two becomes even more convincing after summation of ten consecutively measured spectra, six of which are displayed in figure 6.6(c). By applying markers to the three

wave-number regions, I, II, III, as it was done in figure 6.2, we find that in region I around (600 cm^{-1}) the summed SERS spectrum has two bands matching those of a drop-cast TC dye, which is plotted again, for clarity, below the summed spectrum. The modes around 400 cm^{-1} and 900 cm^{-1} are, however, absent in the related TC dye SERS. In the remaining regions II and III the two spectra have, more or less, the same Raman bands and even similar backgrounds. Hence, our experiments corroborate the fact that the dye molecules are adsorbed on the surface of the NPs, and point out another interesting possibility - the dye molecules drop-cast on the surface of HOPG may be similarly organized as the dye molecules on the surface of the NPs.

Panel (d) in figure 6.6 displays SERS spectra characterized by a pronounced band blinking in the 1000 cm^{-1}-1800 cm^{-1} range, as indicated by gray (orange) region. The resemblance of the spectra in figure 6.6(d) and those of pristine NPs in Figs. 6.3(c) and 6.3(d) suggests that the TC dye molecules are not adsorbed on the surface of the NPs. However, summation of the consecutive recordings, shown in the lower part of figure 6.6(d), reveals certain SERS bands in region II and III which are overlapping the drop-cast TC dye bands. Occasional emergence of Raman bands which could belong to the TC dye bands in regions I, II and III, however, is a common event even for the SERS spectra of pristine NPs. Having in mind that practically the entire enhanced Raman signal originates form the analyte located in the nanogaps, the blinking SERS signal can interpreted as a consequence of mixing of the pristine Ag NPs blinking SERS and the TC dye SERS collected at different nanogaps where the former has the dominant contribution. Consequently, we are unable to conclude whether the NP clusters exhibiting blinking SERS bands have the dye molecules adsorbed on their surface or not. However, the existence of the two distinct SERS spectra clearly points out that the Ag NPs are partially covered by the TC dye molecules. This further indicates that during the adsorption process, the TC dye molecules are either competing with citrate anions in order to replace them on the surface of the NPs or that the TC dye molecules have a difficulty conforming over the citrate anion mantle. Hence, we proceed further by changing the concentration of TC dye in the mixture while maintaining the concentration of Ag NPs constant at n_{Ag}=16 nM.

Blinking and TC dye SERS spectra observed for $0.01n_{TC}$=0.5 μM, $0.1n_{TC}$=5 μM, and $0.5n_{TC}$=25 μM of TC, are shown in Figs. 6.7(a), 6.7(b), 6.7(c), respectively.

By analyzing spectra at the hotspots within various Raman maps, we find that the NP clusters deposited from the solution with the lowest dye concentration yield no clear dye SERS spectra, whereas the NP clusters deposited from the solution with the two higher dye concentration provide a number of distinct TC dye SERS spectra at the hotspots, shown in figure 6.7. Comparison of the summed SERS spectra,

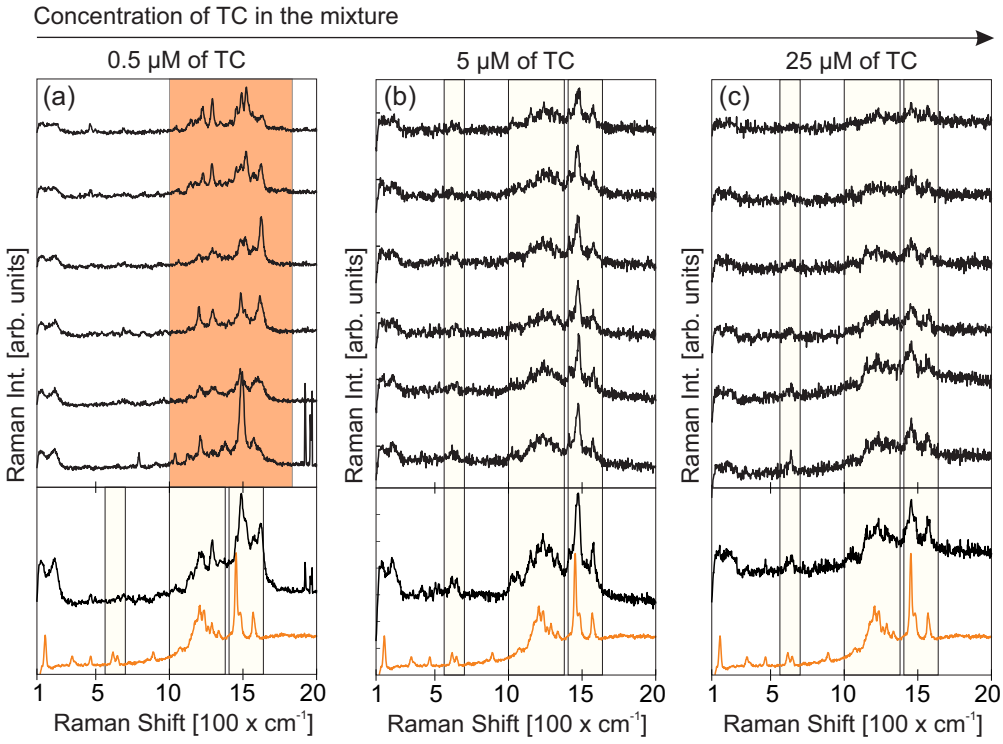

Figure 6.7: Blinking and TC dye SERS spectra (acquired by consecutive measurements with 40 s time step) at hotspots on the samples made by varying the TC concentration in TC-Ag NP mixture: (a)0.5 μM, (b)5 μM and (c)25 μM. All shown spectra were taken under the same conditions using 532 nm laser with power density of 200 μW/μm^2.

in the lower parts of panels (a), (b) and (c) in figure 6.7, and the concentrated TC dye Raman spectra corroborates that the SERS spectra in panels (b) and (c) correspond to the one of the TC dye. Interestingly, even though the absorbance curve corresponding to the Ag NP-TC dye mixture with $0.1n_{\mathrm{TC}}$=5 μM of TC [see figure 6.1(b)] shows no indication that the adsorption of TC dye molecules is taking place, our Raman experiments clearly show the opposite. This is due to the fact that confocal Raman probe is far more sensitive to the individual dye covered NP clusters than the spectrophotometry. As expected, using TC dye concentrations of $0.01n_{\mathrm{TC}}$=0.5 μM, $0.1n_{\mathrm{TC}}$=5 μM in the final solution yields either pristine or partially covered NP clusters, a fact that concurs with the results in Ref. [112]. However, observation of the blinking type SERS within the NP clusters derived from the mixture with the highest TC dye concentration of $0.5n_{\mathrm{TC}}$=25 μM, for which all of the NPs in the solution should be covered by the dye molecules [112], further indicates that the citrate anion mantle impedes the adsorption of the TC dye molecules. In order to examine this possibility we have performed an additional set of measurements on a control sample - a borate anion capped Ag NPs mixed with the TC dye and deposited on the surface of 300 nm thick SiO_2, which is thermally

grown on the Si wafer. Meanwhile, the borate anion capped NPs are unstable with the average lifetimes of the order of couple of hours in the colloid dispersion and are usually stabilized by sodium citrate (or rather by the citrate anions which replace the borate anions while conforming to the surface of the NPs), as explained in Ref. [112]. The related lifetimes are much shorter upon deposition of these NPs on a substrate. The SiO_2 surface is hydrophobic, and, therefore, promotes formation of closely spaced clusters larger than those observed on mica, since the droplet drop-cast of the former dries over a certain area rather than spreading all over the surface. Such an arrangement, along with the enhanced contrast between the SiO_2 surface and the clusters, is absolutely necessary given the instability of borate anion capped NPs.

In Figs. 6.8 (a), 6.8 (b) and 6.8 (c) displayed are three Raman maps corresponding to: (i) NP clusters deposited on mica from a solution having a (citrate capped) NP to the TC dye concentration ratio of 22 nM / 17 μM$\approx 1.3\times10^{-3}$, (ii) NP clusters deposited on mica from a solution having a (citrate capped) NP to the TC dye concentration ratio of 16 nM / 25 μM$\approx 1.3\times10^{-3}$ (iii) NP clusters deposited on SiO_2/Si from a solution having a (borate capped) NP to the TC dye concentration ratio of 10 nM / 16 μM$\approx 1.3\times10^{-3}$, respectively. The (red) diamonds mark the spatial positions within the hotspots where the blinking type of Raman spectra is observed, whereas the (green) squares mark the pixels having the TC dye type of Raman spectra. These maps share the colorbar which is located below them. Panels (d), (e) and (f) of figure 6.8 display examples of the spectra collected at the hotspots within the corresponding maps in panels (a), (b) and (c), respectively. For comparison, the concentrated TC dye Raman spectra is plotted in each panel, below all the other spectra.

The dye/borate capped NPs deposited on the SiO_2/Si, form a higher number of larger clusters than the dye/citrate capped NPs on mica, as seen by comparing the Raman maps in panels (a), (b) and (c), as expected. The SERS spectra acquired at these clusters is exclusively of the TC dye type, as seen in panel (c). In fact, we find this to be the case for every recorded Raman map. Oppositely, the dye/citrate capped NP clusters exhibit both the blinking and the TC dye SERS, even when the ratio of the citrate capped NPs and the TC dye concentrations in solution is approximately the same as the one of the borate capped NPs and the TC dye [compare panels (b) and (c) in figure 6.8]. The adsorption of the TC dye seems to be more efficient if the Ag NPs have borate anions initially conformed to their surface and, therefore, we conjecture that the citrate anions indeed interfere with the adsorption process of the TC dye molecules.

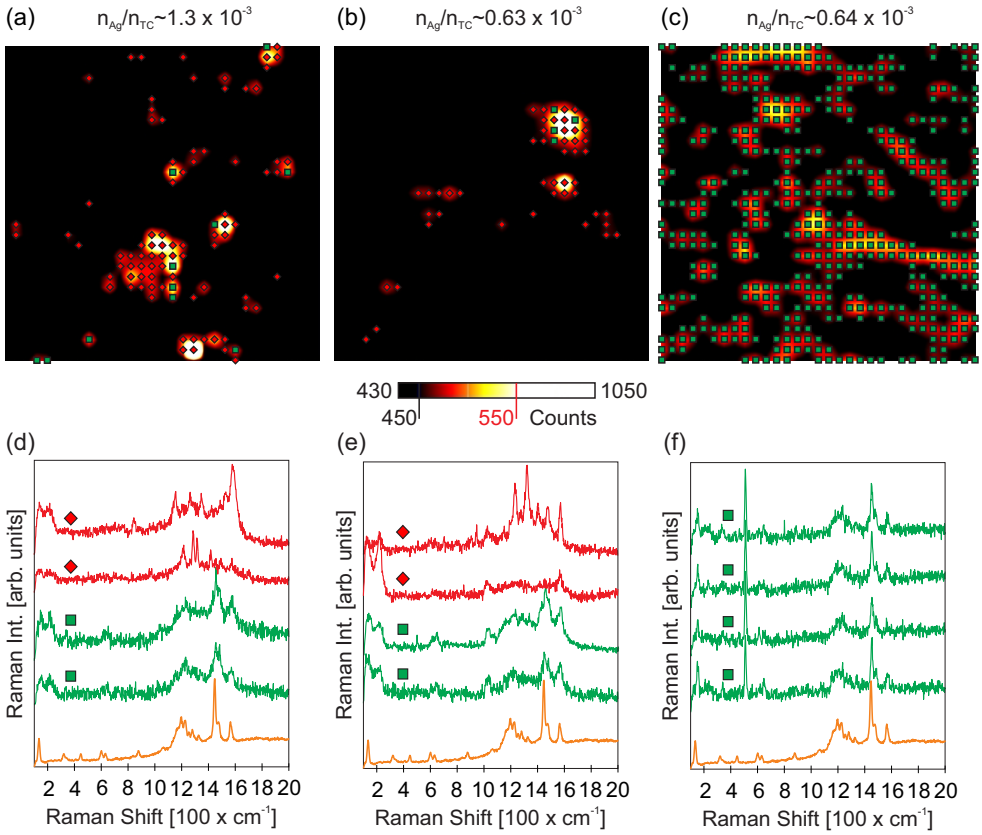

Figure 6.8: Raman maps of (a) clusters deposited on mica from a solution having a (citrate capped) NP to the TC dye concentration ratio of 22 nM / 17 μM$\approx 1.3\times10^{-3}$, (b) clusters deposited on mica from a solution having a (citrate capped) NP to the TC dye concentration ratio of 16 nM / 25 μM$\approx 1.3\times10^{-3}$ (c) clusters deposited on SiO_2/Si from a solution having a (borate capped) NP to the TC dye concentration ratio of 10 nM / 16 μM$\approx 1.3\times10^{-3}$. (d), (e), (f) Examples of the blinking and dye SERS spectra observed in the Raman maps, displayed below the corresponding Raman maps.

6.3 Conclusion

In conclusion, the analysis of SERS enhancement based on rigorous simulations of Maxwell equations for the case of plane wave scattering on random silver nanoparticle clusters on various substrates has shown that, for the investigated nanoparticles and the 532 nm excitation laser, typical enhancement factors in the range of $10^2 - 10^3$ can be expected. The highest field enhancement factors are reached at collective nanoparticle plasmon resonances, which lie in the 400-500 nm range for medium sized clusters (around 20 nanoparticles), and become redshifted in elongated clusters with an increasing number of particles. From an inspection of electromagnetic field distribution on nanoparticle surfaces, a conclusion is reached that at least 90 % of the SERS total enhancement originates from nanogaps between adjacent nanoparticles, implying that the experiments are sensitive only to adsorbates located

in these gaps.

Combined AFM and PL mapping of citrate-capped Ag NP clusters with dye molecules adsorbed from solutions of variable TC concentration have shown that, even at highest TC concentrations, not all hotspots exhibit Raman signatures characteristic of TC dye molecules, indicating that the clusters are only partially covered by dye molecules. In contrast, the control experiment carried out with borate-capped Ag NP clusters, with similar nanoparticle and dye concentrations, has shown a complete dye-coverage of Ag NP clusters.

These results are a direct demonstration that the citrate anions, while useful for stabilizing the colloid, impede the efficient TC dye adsorption.

Chapter 7 Summary

In summary, a number of two-dimensional systems including charge density modulations of the quasi-two-dimensional electron system in $CeTe_3$, two-dimensional electron system in graphene, two-dimensional excitons in MoS_2, and surface plasmons in metallic nanoparticle clusters were probed by a number of scanning probe microscopy and optical spectroscopy techniques. Additionally, the optical properties, spectroscopic data and some potential applications of these systems were investigated numerically.

In particular, STM, STS and Raman spectroscopy were used for analysis of the CDW state in $CeTe_3$ at room temperature. The analysis based on retrieval of characteristic CDW parameters shows that the CDW is formed only in two-dimensional layers of Te atoms with negligible interference of the underlying crystal. The dominant CDW modulation wave vector and the CDW gap were found to have values of $|\mathbf{q}| = 10.26\,\mathrm{nm}^{-1}$ and $\sim 0.37\,\mathrm{eV}$, respectively. The most important result of this study, however, is the fact that the charge density modulation is followed by modulation of the underlying Te sheet atoms, which was not observed in previous STM studies. The rare-earth tellurides, being a part of a larger family of metallic layered compounds, are commonly considered as the CDW 'model' systems. Therefore, the conclusions reached within this work, in general, may contribute to better understanding of the fundamental mechanism behind the formation of CDWs in metallic compounds.

A combined EFM/KPFM analysis was used for investigation of graphene back-gate devices. Our analysis shows that such devices have superior performance when isolated from the environment, which induces instabilities in doping levels of graphene even upon application of the gate voltage. Having in mind that various graphene-based electronic and optoelectronic devices are constructed by exploiting this configuration, this result shows a possible way of improving the performance of future graphene based devices. From another perspective, we have demonstrated the possibility of imaging graphene below an insulator (the protective layer) by utilizing the EFM and KPFM techniques. In addition, by means of numerical simulations of Maxwell'e equations we have studied graphene-waveguide coupled system. We have shown that the graphene-induced change of the propagation constant is given by the product of a factor characterizing the graphene-waveguide coupling strength

and the optical conductivity of graphene. Finally, we have discussed how graphene-waveguide coupled system can be utilized for realization of electro-absorptive and electro-refractive optical modualtors. Considering that graphene's optical conductivity can vary significantly depending on the graphene fabrication procedure and environment, we have simultaneously investigated the predictions of the theoretical and experimental dataset. As expected, the theoretical dataset has been found to predict a considerably better modulator performance. We have also shown that, in case of electro-absorptive optical modulators, the ratio of the modulation depth to insertion losses, which is a commonly used figure of merit for electro-optical modulators, does not depend on the waveguide geometry and graphene coverage at all but that it is exclusively a function of the residual conductivity of graphene.

The two-dimensional excitons in pristine and nanoparticle functionalized MoS_2 were studied by combination of AFM and PL spectroscopy techniques. In this study, the combined AFM/PL analysis has shown uncontrolled variations of both the spectral position and spectral width of excitonic A and B PL peaks. These variations are found to be a consequence of either fabrication residues, adsorbates or mechanical deformations of the MoS_2. By analysing the PL of functionalized MoS_2 samples, we have not observed significant PL modifications. In fact, the spatial variations of the position and spectral width of the PL peaks are kept within the initial variation range upon introduction of the spherical and cubical NP clusters. Moreover, the NP clusters turned out to be rather inefficient 'enhancers' of the MoS_2 PL, with the enhancement factors in 1-1.55 range. In principal, the size and shape of the clusters have no significant effect on the PL enhancement factors, as evidenced by a slightly higher values observed in case of clustered cubes than in case of clustered spheres. The additional analysis based on rigorous numerical simulations of plane wave scattering on NP clusters has shown that the distribution and the orientation of the clusters' electric fields with respect to the MoS_2 are key factors which determine the coupling efficiency. The largest electric field values are observed within the nano-gaps between the NPs in a cluster, and the field becomes weaker as one approaches the bottom part of the cluster which is facing the MoS_2, thus, reducing the intensity enhancement. However, we have found that even more important factor is, in fact, the orientation of the NPs electric field with respect to the MoS_2 plane, since only the electric fields parallel to the MoS_2 surface are capable of enhancing the MoS_2 PL. Our simulations show that in middle-sized clusters, composed of either nano-spheres or nano-cubes, the total electric field has large normal and weak tangential components at and in the vicinity of the clusters' surface, thus, ultimately leading to small PL enhancement factors. In addition, we have proposed an alternative way for improving the enhancement factors, based on exploiting intensive fields within the NPs nano-gaps.

Finally, AFM and SERS techniques were used for the study of the adsorption of thin aggregated TC dye layers on citrate-capped Ag NP clusters. From this study we have found that, even at highest TC concentrations, not all hotspots exhibit Raman signatures characteristic of TC dye molecules, indicating that the clusters are only partially covered by dye molecules. In contrast, the control experiment carried out with borate-capped Ag NP clusters, with similar nanoparticle and dye concentrations, has shown a complete dye-coverage of Ag NP clusters. These results are a direct demonstration that the citrate anions, while useful for stabilizing the colloid, impede the efficient TC dye adsorption.

Appendix

A.1 Addition to Chapter 4

Figure 1 shows the time dependance of the relative EFM phase shift in graphene measured with respect to the Au electrode. The gate voltage in this case is equal to zero. As it can be seen from panel (a), the bare sample experiences larger $\Delta\phi$ variations than the isolated sample. The differential $\Delta\phi$, in panel (b), emphasises larger $\Delta\phi$ variations within the bare sample.

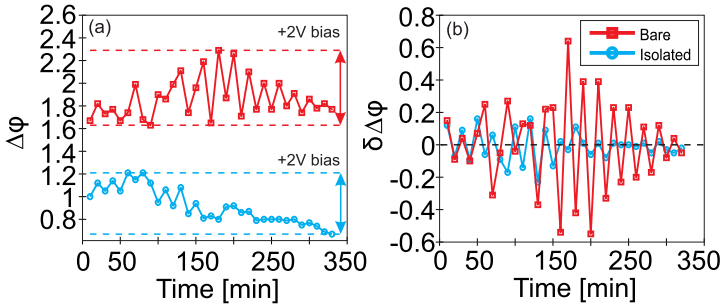

Figure 1: (a) Time dependance of the relative EFM phase shift in graphene measured with respect to the Au electrode. The tip was biased by +2 V for both bare and isolated sample. (b) differential relative phase shift in graphene.

B.2 Addition to Chapter 5

B.2.1 Additional measurements

The maps in figure 2 show variations of the A and B peaks intensity, spectral position and width on another, pristine MoS_2 sample.

The data in figures 3 and 4 is collected at the same fragment of the MoS_2 sample as the data shown in figure 5.11. However, figures 3 and 4 represent the hotspots on the bi- and three-layer segments, whereas figure 5.11 represent the hotspots on the mono-layer segment.

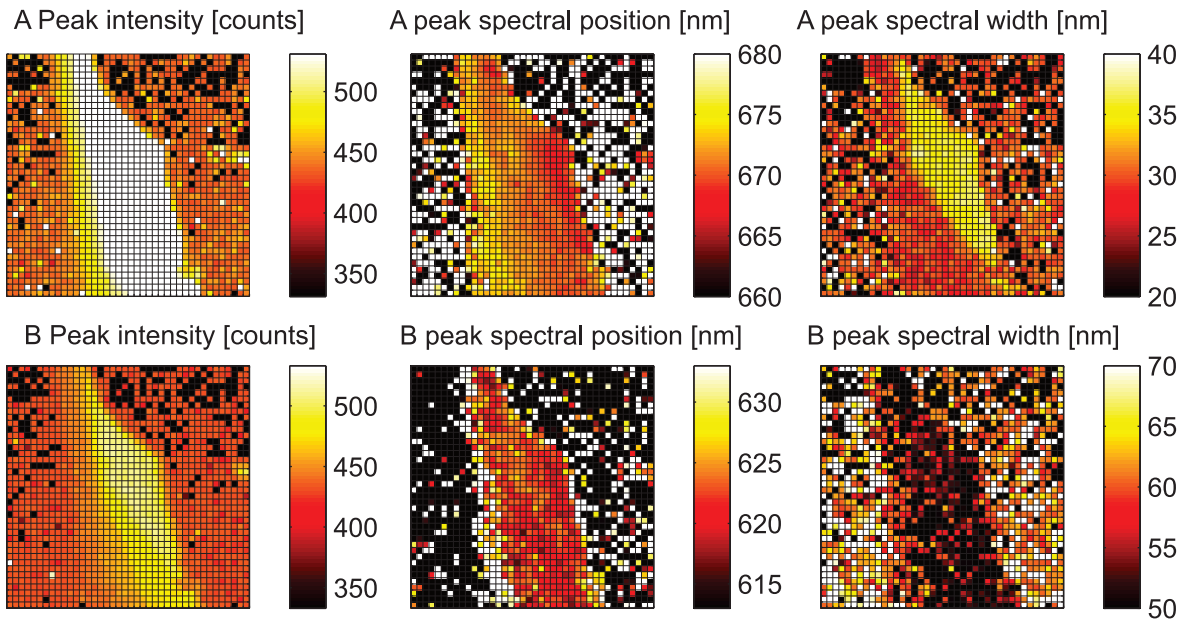

Figure 2: Intensity, spectral position and width of A and B peaks assessed from Lorenzian fits

B.2.2 Verification of the numerical model

Figure 5 illustrates that the numerical model is very accurate, since the numerically calculated curves fit perfectly the curves which are calculated using analytical expressions provided by the Mie theory.

B.2.3 Influence of the number of nanoparticles and the distance between them on the optical properties of the clusters

Figure 6 shows how the distance between the nanoparticles and their number within the cluster influence the optical properties of the cluster.

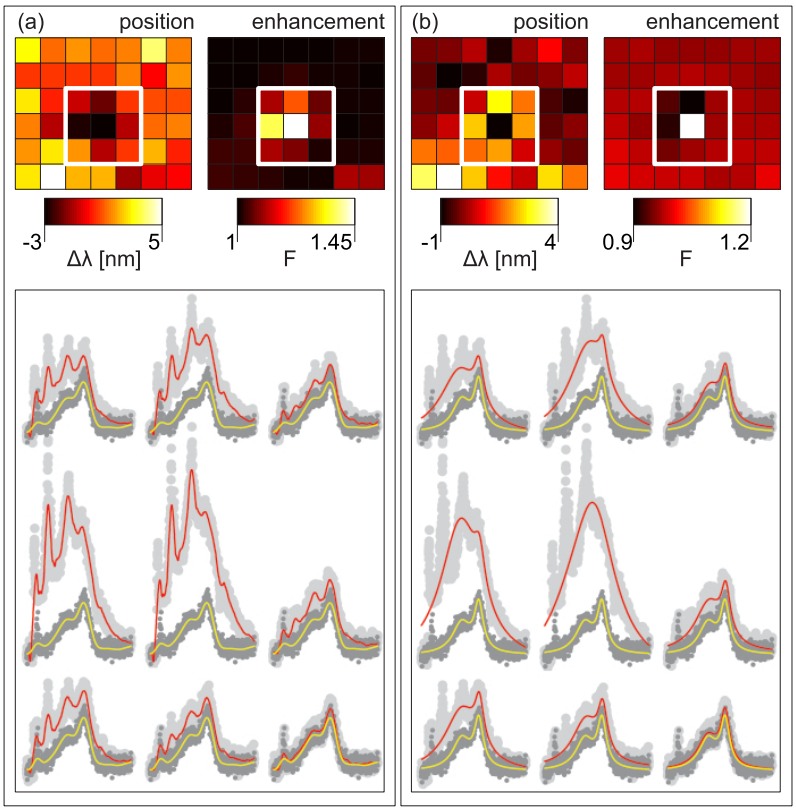

Figure 3: (a) The $\Delta\lambda$ and F maps of the area around the hotspot on the bi-layer segment. These maps are derived from the smoothed/filtered data as illustrated in the left panel in figure 5.10. Below the maps shown are the spectra (light gray markers) acquired at pixels which are bordered by the white square in the related $\Delta\lambda$ and F maps. Additionally, with each of the mentioned spectra plotted is the reference spectrum (dark gray markers). Red/yellow solid lines represent the smoothed/filttered data. (b) The $\Delta\lambda$ and F maps of the same area, but derived from the fitted data as illustrated in the left panel in figure 5.10. Below the maps shown are the spectra (light gray markers) acquired at pixels which are bordered by the white square in the related $\Delta\lambda$ and F maps. Additionally, with each of the mentioned spectra plotted is the reference spectrum (dark gray markers). Red/yellow solid lines represent fits.

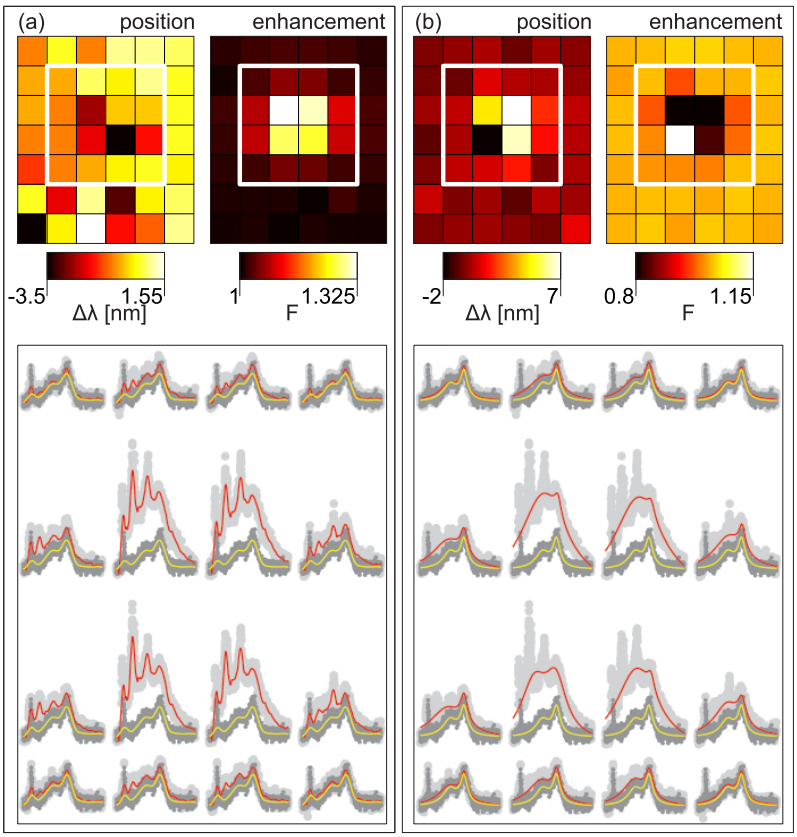

Figure 4: (a) The $\Delta\lambda$ and F maps of the area around the hotspot on the three-layer segment. These maps are derived from the smoothed/filtered data as illustrated in the left panel in figure 5.10. Below the maps shown are the spectra (light gray markers) acquired at pixels which are bordered by the white square in the related $\Delta\lambda$ and F maps. Additionally, with each of the mentioned spectra plotted is the reference spectrum (dark gray markers). Red/yellow solid lines represent the smoothed/filttered data. (b) The $\Delta\lambda$ and F maps of the same area, but derived from the fitted data as illustrated in the left panel in figure 5.10. Below the maps shown are the spectra (light gray markers) acquired at pixels which are bordered by the white square in the related $\Delta\lambda$ and F maps. Additionally, with each of the mentioned spectra plotted is the reference spectrum (dark gray markers). Red/yellow solid lines represent fits.

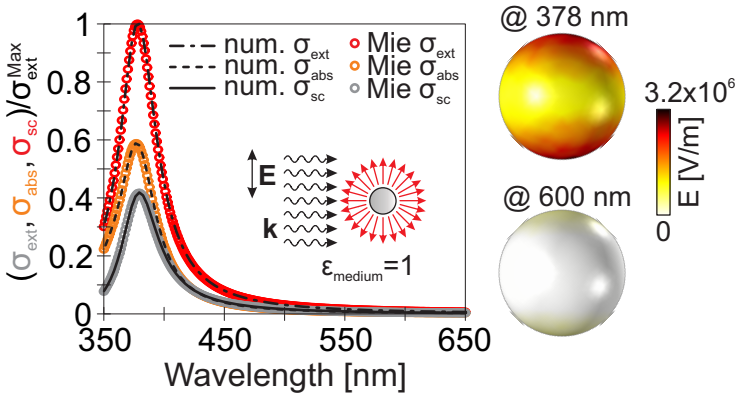

Figure 5: Extinction, absorption and scattering cross sections of a spherical nanoparticle calculated numerically (solid, dashed, dotted-dashed lines) and analytically by using Mie theory. The diameter of the nanoparticle is 60 nm and the surrounding medium is vacuum. The inset to the right shows the electric field distribution at the dipole-like localised surface plasmon resonance and off the resonance.

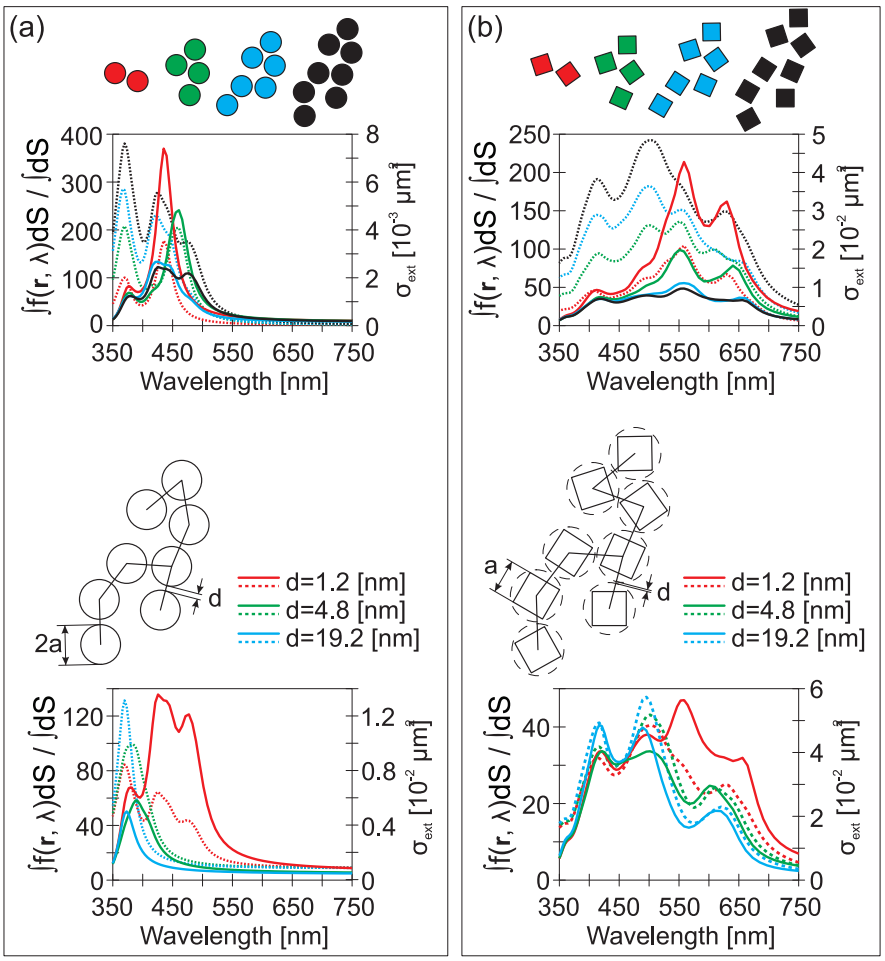

Figure 6: Upper part of panels (a) and (b) show how the extinction cross section (dotted curves) and the average intensity enhancement (solid curves) change when the number of nanoparticles in the cluster is changed. Lower parts of panels (a) and (b) show how the extinction cross section (dotted curves) and the average intensity enhancement (solid curves) change when the distance, d, between the nanoparticles is changed.

References

[1] T. Ando, A. B. Fowler, and F. Stern. Electronic properties of two-dimensional systems. *Rev. Mod. Phys.*, 54:437–672, 1982. 5, 6, 7

[2] C. C. Grimes and G. Adams. Observation of two-dimensional plasmons and electron-ripplon scattering in a sheet of electrons on liquid helium. *Phys. Rev. Lett.*, 36:145–148, 1976. 5, 9

[3] A. Ohtomo and H. Y. Hwang. A high-mobility electron gas at the $LaAlO_3/SrTiO_3$ heterointerface. *Nature*, 427:423–426, 2004. 6

[4] U. H. Grote and H. H. Soonpaa. Field effects in extremely thin crystals of $Bi_8Te_7S_5$. *J. Vac. Sci. Technol.*, 10(5):723–724, 1973. 6, 15

[5] W. Shockley. On the surface states associated with a periodic potential. *Phys. Rev.*, 56:317–323, 1939. 7

[6] R. H. Ritchie. Plasma losses by fast electrons in thin films. *Phys. Rev.*, 106:874–881, 1957. 8

[7] P. Monçeau, N. P. Ong, A. M. Portis, A. Meerschaut, and J. Rouxel. Electric field breakdown of charge-density-wave induced anomalies in $NbSe_3$. *Phys. Rev. Lett.*, 37:602–606, 1976. 9

[8] G. Grüner. *Density Waves in Solids*. Addison-Wesley, Reading, MA, 1994. 10, 12, 34

[9] R. H. Dalitz, R. E. Peierls, and J. Peifer. *Selected scientific papers of Sir Rudolf Peierls: with commentary*. World Scientific Series in 20th Century Physics. World Scientific, Singapore, 1997. 11

[10] W. Kohn. Image of the Fermi Surface in the Vibration Spectrum of a Metal. *Phys. Rev. Lett.*, 2(9):393, 1959. 12

[11] U. Ralević, N. Lazarević, A. Baum, H.-M. Eiter, R. Hackl, P. Giraldo-Gallo, I. R. Fisher, C. Petrovic, R. Gajić, and Z. V. Popović. Charge density wave modulation and gap measurements in $CeTe_3$. *Phys. Rev. B*, 94:165132, 2016. 12

[12] M. D. Johannes and I. I. Mazin. Fermi surface nesting and the origin of charge density waves in metals. *Phys. Rev. B*, 77:165135, 2008. 13, 37

[13] H.-M. Eiter, M. Lavagnini, R. Hackl, E. A. Nowadnick, A. F. Kemper, T. P. Devereaux, J.-H. Chu, J. G. Analytis, I. R. Fisher, and L. Degiorgi. Alternative route to charge density wave formation in multiband systems. *PNAS*, 110(1):64–69, 2013. 13, 34, 37, 45, 46

[14] K. Barnham, editor. *Low-dimensional semiconductor structures : fundamentals and device applications*. Cambridge University Press, Cambridge, 2001. 14

[15] P. Dawson, K. J. Moore, G. Duggan, H. I. Ralph, and C. T. B. Foxon. Unambiguous observation of the 2*s* state of the light- and heavy-hole excitons in GaAs – (AlGa)As multiple-quantum-well structures. *Phys. Rev. B*, 34:6007–6010, 1986. 15

[16] K. S. Novoselov, A. Mishchenko, A. Carvalho, and A. H. Castro Neto. 2d materials and van der waals heterostructures. *Science*, 353(6298), 2016. 15, 16

[17] K. F. Mak and J. Shan. Photonics and optoelectronics of 2D semiconductor transition metal dichalcogenides. *Nat. Photon.*, 10:216–226, 2016. 15, 16

[18] A. N. Grigorenko, M. Polini, and K. S. Novoselov. Graphene plasmonics. *Nat. Photon.*, 6:749–758, 2012. 15, 16

[19] T. Low, A. Chaves, Kumar A. Caldwell, J. D., N. X. Fang, P. Avouris, T. F. Heinz, F. Guinea, L. Martin-Moreno, and F. Koppens. Polaritons in layered two-dimensional materials. *Nat. Mater.*, 16(2):184–194, 2017. 15

[20] K. S. Novoselov, A. K. Geim, S. V. Morozov, D. Jiang, Y. Zhang, S. V. Dubonos, I. V. Grigorieva, and A. A. Firsov. Electric field effect in atomically thin carbon films. *Science*, 306(5696):666–669, 2004. 15, 47, 52, 64

[21] P. Joensen, R. F. Frindt, and S. R. Morrison. Single–layer MoS_2. *Mater. Res. Bull.*, 21(4):457 – 461, 1986. 15

[22] A. K. Geim and K. S. Novoselov. The rise of graphene. *Nat. Mater.*, 6(3):183–191, 2007. 16, 47, 66

[23] F. Bonaccorso, Z. Sun, T. Hasan, and A. C. Ferrari. Graphene photonics and optoelectronics. *Nat. Photon.*, 4(9):611–622, 2010. 16, 66

[24] Z. Q. Li, E. A. Henriksen, Z. Jiang, Z. Hao, M. C. Martin, P. Kim, H. L. Stormer, and D. N. Basov. Dirac charge dynamics in graphene by infrared spectroscopy. *Nat. Phys.*, 4(7):532–535, 2008. 16, 47, 66, 70, 73

[25] Q. H. Wang, K. Kalantar-Zadeh, A. Kis, J. N. Coleman, and M. S. Strano. Electronics and optoelectronics of two-dimensional transition metal dichalcogenides. *Nat. Nano.*, 7(11):699–712, 2012. 16

[26] G. Eda and S. A. Maier. Two-dimensional crystals: Managing light for optoelectronics. *ACS Nano*, 7:5660–5665, 2013. 16, 79

[27] M. Kratzer, S. Klima, C. Teichert, B. Vasić, A. Matković, U. Ralević, and R. Gajić. Temperature dependent growth morphologies of parahexaphenyl on sio2 supported exfoliated graphene. *J. Vac. Sci. Technol. B*, 31(4):04D114, 2013. 16

[28] M.-Y. Li, Y. Shi, C.-C. Cheng, L.-S. Lu, Y.-C. Lin, H.-L. Tang, M.-L. Tsai, C.-W. Chu, K.-H. Wei, J.-H. He, W.-H. Chang, K. Suenaga, and L.-J. Li. Epitaxial growth of a monolayer $WSe_2 - MoS_2$ lateral p-n junction with an atomically sharp interface. *Science*, 349(6247):524–528, 2015. 16

[29] A. Zurutuza and C. Marinelli. Challenges and opportunities in graphene commercialization. *Nat. Nano.*, 9(10):730–734, 2014. 16, 18, 47

[30] Q. Bao and K. P. Loh. Graphene photonics, plasmonics, and broadband optoelectronic devices. *ACS Nano*, 6(5):3677–3694, 2012. 16, 47, 66

[31] K. Kim, J.-Y. Choi, T. Kim, S.-H. Cho, and H.-J. Chung. A role for graphene in silicon-based semiconductor devices. *Nature*, 479(7373):338–344, 2011. 16, 47

[32] F. Xia, H. Wang, D. Xiao, M. Dubey, and A. Ramasubramaniam. Two-dimensional material nanophotonics. *Nat. Photon.*, 8:899–907, 2014. 16, 17, 66, 79

[33] X. Duan, C. Wang, A. Pan, R. Yu, and X. Duan. Two-dimensional transition metal dichalcogenides as atomically thin semiconductors: opportunities and challenges. *Chem. Soc. Rev.*, 44:8859–8876, 2015. 16

[34] R. Wiesendanger. *Scanning Probe Microscopy and Spectroscopy Methods and Applications*. Cambridge University Press, Cambridge, 1 edition, 1994. 21, 22

[35] C.H. Lei, A. Das, M. Elliott, and J. E. Macdonald. Quantitative electrostatic force microscopy-phase measurements. *Nanotechnology*, 15(5):627, 2004. 26

[36] A. Smekal. Zur quantentheorie der dispersion. *Naturwissenschaften*, 11(43):873–875, 1923. 27

[37] R. Singh. C. v. raman and the discovery of the raman effect. *Phys. Perspect.*, 4(4):399–420, 2002. 27

[38] C. V. Raman and K.S. Khrishnan. A New Type of Secondary Radiation. *Nature*, 121:501–502, 1928. 27

[39] R. Singh and F. Riess. The 1930 nobel prize for physics: A close decision? *Notes Rec. R. Soc. Lond.*, 55(2):267–283, 2001. 27

[40] M. Fleischmann, P.J. Hendra, and A.J. McQuillan. Raman spectra of pyridine adsorbed at a silver electrode. *Chem. Phys. Lett.*, 26(2):163–166, 1974. 29

[41] D. L. Jeanmaire and R. P. Van Duyne. Surface raman spectroelectrochemistry. *J. Eelecrtoanal. Chem.*, 84(1):1 – 20, 1977. 29

[42] M. G. Albrecht and J. A. Creighton. Anomalously intense raman spectra of pyridine at a silver electrode. *J. Am. Chem. Soc.*, 99(15):5215–5217, 1977. 29

[43] M. Kerker, O. Siiman, L. A. Bumm, and D.-S. Wang. Surface enhanced raman scattering SERS of citrate ion adsorbed on colloidal silver. *Appl. Opt.*, 19(19):3253–3255, 1980. 29

[44] E. Anemogiannis, E. N. Glytsis, and T. K. Gaylord. Determination of guided and leaky modes in lossless and lossy planar multilayer optical waveguides: reflection pole method and wavevector density method. *J. Lightwave Technol.*, 17(5):929–941, 1999. 30

[45] *COMSOL MULTIPHYSICS v5.2, COMSOL, Inc.* 31, 81, 104

[46] G. Ghiringhelli, M. Le Tacon, M. Minola, S. Blanco-Canosa, C. Mazzoli, N. B. Brookes, G. M. De Luca, A. Frano, D. G. Hawthorn, F. He, T. Loew, M. Moretti Sala, D. C. Peets, M. Salluzzo, E. Schierle, R. Sutarto, G. A. Sawatzky, E. Weschke, B. Keimer, and L. Braicovich. Long-Range Incommensurate Charge Fluctuations in (Y,Nd)$Ba_2Cu_3O_{6+x}$. *Science*, 337(6096):821–825, 2012. 34

[47] M. B. Maple, J. J. Hamlin, D. A. Zocco, M. Janoschek, R. E. Baumbach, B. D. White, I. R. Fisher, and J.-H. Chu. Superconductivity, spin and charge order, and quantum criticality in correlated electron materials. *EPJ Web of Conferences*, 23:00012, 2012. 34

[48] E. DiMasi, M. C. Aronson, J. F. Mansfield, B. Foran, and S. Lee. Chemical pressure and charge-density waves in rare-earth tritellurides. *Phys. Rev. B*, 52:14516–14525, 1995. 34

[49] H. Yao, J. A. Robertson, E.-A. Kim, and S. A. Kivelson. Theory of stripes in quasi-two-dimensional rare-earth tellurides. *Phys. Rev. B*, 74(24):245126, 2006. 34, 36, 37

[50] N. Ru and I. R. Fisher. Thermodynamic and transport properties of YTe_3, $LaTe_3$, and $CeTe_3$. *Phys. Rev. B*, 73(3):033101, 2006. 34

[51] A. Sacchetti, C. L. Condron, S. N. Gvasaliya, F. Pfuner, M. Lavagnini, M. Baldini, M. F. Toney, M. Merlini, M. Hanfland, J. Mesot, J.-H. Chu, I. R. Fisher, P. Postorino, and L. Degiorgi. Pressure-induced quenching of the charge-density-wave state in rare-earth tritellurides observed by x-ray diffraction. *Phys. Rev. B*, 79:201101, 2009. 34

[52] A. Sacchetti, E. Arcangeletti, A. Perucchi, L. Baldassarre, P. Postorino, S. Lupi, N. Ru, I. R. Fisher, and L. Degiorgi. Pressure dependence of the charge-density-wave gap in rare-earth tritellurides. *Phys. Rev. Lett.*, 98:026401, 2007. 34

[53] C. D. Malliakas, S. J. L. Billinge, H. J. Kim, and Kanatzidis M. G. Square nets of tellurium: Rare-earth dependent variation in the charge-density wave of $RETe_3$ (RE =rare-earth element). *J. Am. Chem. Soc.*, 127(18):6510–6511, 2005. 34, 39, 40

[54] C. D. Malliakas and M. G. Kanatzidis. Divergence in the behavior of the charge density wave in $RETe_3$ (RE =rare-earth element) with temperature and RE element. *J. Am. Chem. Soc.*, 128(39):12612–12613, 2006. 34

[55] N. Ru, C. L. Condron, G. Y. Margulis, K. Y. Shin, J. Laverock, S. B. Dugdale, M. F. Toney, and I. R. Fisher. Effect of chemical pressure on the charge density wave transition in rare-earth tritellurides RTe_3. *Phys. Rev. B*, 77(3):035114, 2008. 34

[56] D. Necas and P. Klapetek. Gwyddion: an open-source software for SPM data analysis. *Cent. Eur. J. Phys.*, 10:181–188, 2012. 34

[57] T. P. Devereaux and R. Hackl. Inelastic light scattering from correlated electrons. *Rev. Mod. Phys.*, 79(1):175, 2007. 35

[58] B. Muschler, W. Prestel, L. Tassini, R. Hackl, M. Lambacher, A. Erb, Seiki Komiya, Yoichi Ando, D.C. Peets, W.N. Hardy, R. Liang, and D.A. Bonn.

Electron interactions and charge ordering in CuO_2 compounds. *Eur. Phys. J. Special Topics*, 188:131, 2010. 35

[59] B. K. Norling and H. Steinfink. The crystal structure of neodymium tritelluride. *Inorg. Chem.*, 5(9):1488 – 1491, 1966. 35

[60] A. Kikuchi. Electronic Structure of Lanthan Ditellurides. *J. Phys. Soc. Japan*, 67(4):1308–1312, 1998. 36

[61] H.-M. Eiter. *Carrier and Lattice Dynamics in Systems with Charge and Spin Order*. PhD thesis, PhD thesis, Technische Universität München, 2014. 37

[62] A. Tomic, Zs. Rak, J. P. Veazey, C. D. Malliakas, S. D. Mahanti, M. G. Kanatzidis, and S. H. Tessmer. Scanning tunneling microscopy study of the $CeTe_3$ charge density wave. *Phys. Rev. B*, 79:085422, 2009. 37, 43

[63] A. Fang, N. Ru, I. R. Fisher, and A. Kapitulnik. STM studies of $TbTe_3$: Evidence for a fully incommensurate charge density wave. *Phys. Rev. Lett.*, 99:046401, 2007. 39, 42, 43

[64] T. Machida, Y. Fujisawa, K. Igarashi, A. Kaneko, S. Ooi, T. Mochiku, M. Tachiki, K. Komori, K. Hirata, and H. Sakata. Visualizing the effect of structural supermodulation on electronic structure of $IrTe_2$ by scanning tunneling spectroscopy. *Phys. Rev. B*, 88:245125, 2013. 43

[65] A. Soumyanarayanan, M. M. Yee, Y. He, J. van Wezel, D. J. Rahn, K. Rossnagel, E. W. Hudson, M. R. Norman, and J. E. Hoffman. Quantum phase transition from triangular to stripe charge order in $NbSe_2$. *PNAS*, 110(5):1623–1627, 2013. 43

[66] F. Flicker and J. van Wezel. Charge order from orbital-dependent coupling evidenced by $NbSe_2$. *Nat. Commun.*, 6:1, 2015. 43

[67] C. Wang, B. Giambattista, C. G. Slough, R. V. Coleman, and M. A. Subramanian. Energy gaps measured by scanning tunneling microscopy. *Phys. Rev. B*, 42:8890–8906, 1990. 43, 44

[68] V. Brouet, W. L. Yang, X. J. Zhou, Z. Hussain, N. Ru, K. Y. Shin, I. R. Fisher, and Z. X. Shen. Fermi surface reconstruction in the CDW state of $CeTe_3$ observed by photoemission. *Phys. Rev. Lett.*, 93:126405, 2004. 43

[69] M. Lavagnini, M. Baldini, A. Sacchetti, D. Di Castro, B. Delley, R. Monnier, J.-H. Chu, N. Ru, I. R. Fisher, P. Postorino, and L. Degiorgi. Evidence for coupling between charge density waves and phonons in two-dimensional rare-earth tritellurides. *Phys. Rev. B*, 78:201101, 2008. 44

[70] T. P. Devereaux. Theory for the effects of impurities on the Raman spectra of superconductors. *Phys. Rev. B*, 45:12965, 1992. 45

[71] V. Brouet, W. L. Yang, X. J. Zhou, Z. Hussain, R. G. Moore, R. He, D. H. Lu, Z. X. Shen, J. Laverock, S. B. Dugdale, N. Ru, and I. R. Fisher. Angle-resolved photoemission study of the evolution of band structure and charge density wave properties in $R\mathrm{Te}_3$ ($R = \mathrm{Y}$, La, Ce, Sm, Gd, Tb, and Dy). *Phys. Rev. B*, 77(23):235104, 2008. 45, 46

[72] M. Lavagnini, H.-M. Eiter, L. Tassini, B. Muschler, R. Hackl, R. Monnier, J.-H. Chu, I. R. Fisher, and L. Degiorgi. Raman scattering evidence for a cascade evolution of the charge-density-wave collective amplitude mode. *Phys. Rev. B*, 81:081101, 2010. 46

[73] W.Z. Hu, Q.M. Zhang, and N.L. Wang. Optical and Raman spectroscopy studies on Fe-based superconductors. *Physica C*, 469(9-12):545, 2009. 46

[74] A. Matković, U. Ralević, G. Isić, M. M. Jakovljević, B. Vasić, I. Milošević, D. Marković, and R. Gajić. Spectroscopic ellipsometry and the fano resonance modeling of graphene optical parameters. *Phys. Scripta*, 2012(T149):014069, 2012. 48

[75] Y.-F. Chen, D. Liu, Z.-G. Wang, P.-J. Li, X. Hao, K. Cheng, Y. Fu, L.-X. Huang, X.-Z. Liu, W.-L. Zhang, and Y.-R. Li. Rapid determination of the thickness of graphene using the ratio of color difference. *J. Phys. Chem. C*, 115(14):6690–6693, 2011. 48

[76] G. W. Hanson. Dyadic greens functions and guided surface waves for a surface conductivity model of graphene. *J. Appl. Phys.*, 103(6):064302, 2008. 49

[77] D. N. Basov, M. M. Fogler, A. Lanzara, Feng Wang, and Yuanbo Zhang. Graphene spectroscopy. *Rev. Mod. Phys.*, 86:959–994, 2014. 49

[78] S. H. Mousavi, I. Kholmanov, K. B. Alici, D. Purtseladze, N. Arju, K. Tatar, D. Y. Fozdar, J. W. Suk, Y. Hao, A. B. Khanikaev, R. S. Ruoff, and G. Shvets. Inductive tuning of fano-resonant metasurfaces using plasmonic response of graphene in the mid-infrared. *Nano Lett.*, 13(3):1111–1117, 2013. 50

[79] J. T. Robinson, C. Manolatou, L. Chen, and M. Lipson. Ultrasmall mode volumes in dielectric optical microcavities. *Phys. Rev. Lett.*, 95:143901, 2005. 50

[80] P. Nemes-Incze, Z. Osvath, K. Kamars, and Biro L.P. Anomalies in thickness measurements of graphene and few layer graphite crystals by tapping mode atomic force microscopy. *Carbon*, 46:1435 – 1442, 2008. 52, 84

[81] A. Nakayama, S. Hoshino, Y. Yamada, A. Ohmura, and F. Ishikawa. Counting graphene layers based on the light-shielding effect of raman scattering from a substrate. *Appl. Phys. Lett.*, 107(23):231604, 2015. 53

[82] Y. Hao, Y. Wang, L. Wang, Z. Ni, Z. Wang, R. Wang, C. K. Koo, Z. Shen, and J. T. L. Thong. Probing layer number and stacking order of few-layer graphene by raman spectroscopy. *Small*, 6(2):195–200, 2010. 53

[83] D. Stojanović, A. Matković, S. Aškrabić, A. Beltaos, U. Ralević, Dj. Jovanovicć, D. Bajuk-Bogdanović, I. Holclajtner-Antunović, and R. Gajić. Raman spectroscopy of graphene: doping and mapping. *Phys. Scripta*, 2013(T157):014010, 2013. 54

[84] M. Gilić, M. Petrović, R. Kostić, D. Stojanović, T. Barudzija, M. Mitrić, N. Romčević, U. Ralević, J. Trajić, M. Romčević, and I.S. Yahia. Structural and optical properties of $cuse_2$ nanocrystals formed in thin solid Cu – Se film. *Infrared Phys. Technol.*, 76:276 – 284, 2016. 54

[85] A. Beltaos, A. G. Kovačević, A. Matković, U. Ralević, Dj. Jovanović, and B. Jelenković. Damage effects on multi-layer graphene from femtosecond laser interaction. *Phys. Scripta*, 2014(T162):014015, 2014. 54

[86] A. Beltaos, A. G. Kovačević, A. Matković, U. Ralević, S. Savić–Šević, Jovanović Dj., B. M. Jelenković, and R. Gajić. Femtosecond laser induced periodic surface structures on multi-layer graphene. *J. Appl. Phys.*, 116(20):204306, 2014. 54

[87] L. Zitzler, S. Herminghaus, and F. Mugele. Capillary forces in tapping mode atomic force microscopy. *Phys. Rev. B*, 66(15):155436, 2002. 55

[88] A. Matković, A. Beltaos, M. Milićević, U. Ralević, B. Vasić, Dj. Jovanović, and Gajić R. Spectroscopic imaging ellipsometry and fano resonance modeling of graphene. *J. Appl. Phys.*, 112(12):123523, 2012. 55, 57

[89] A. Matković, U. Ralević, Chhikara M., M. M. Jakovljević, Dj. Jovanović, G. Bratina, and R. Gajić. Influence of transfer residue on the optical properties of chemical vapor deposited graphene investigated through spectroscopic ellipsometry. *J. Appl. Phys.*, 114(9):093505, 2013. 55, 57

[90] B. Vasić, M. Kratzer, A. Matković, A. Nevosad, U. Ralević, Dj. Jovanović, C. Ganser, C. Teichert, and R. Gajić. Atomic force microscopy based manipulation of graphene using dynamic plowing lithography. *Nanotechnology*, 24(1):015303, 2013. 55

[91] Y. Shen, D. M. Barnett, and Pinsky P. M. Simulating and interpreting Kelvin probe force microscopy images on dielectrics with boundary integral equations. *Rev. Sci. Instrum.*, 79(2):023711, 2008. 57

[92] D. Ziegler, P. Gava, J. Güttinger, F. Molitor, L. Wirtz, M. Lazzeri, A. M. Saitta, A. Stemmer, F. Mauri, and C. Stampfer. Variations in the work function of doped single- and few-layer graphene assessed by Kelvin probe force microscopy and density functional theory. *Phys. Rev. B*, 83:235434, 2011. 57

[93] A. Matković, M. Chhikara, M. Milievć, U. Ralević, B. Vasić, Dj. Jovanović, M. R. Belić, G. Bratina, and R. Gajić. Influence of a gold substrate on the optical properties of graphene. *J. Appl. Phys.*, 117(1):015305, 2015. 57

[94] G. Lujan, T. Schram, L. Pantisano, J. Hooker, S. Kubicek, E. Rohr, J. Schuhmacher, O. Kilpela, H. Sprey, S. De Gendt, and K. De Meyer. Impact of ALCVD and PVD titanium nitride deposition on metal gate capacitors. In *32nd European Solid-State Device Research Conference*, pages 583–586, 2002. 60

[95] Y.-J. Yu, Y. Zhao, S. Ryu, L. E. Brus, K. S. Kim, and P. Kim. Tuning the graphene work function by electric field effect. *Nano. Lett.*, 9(10):3430–3434, 2009. 60

[96] N. J. Lee, J. W. Yoo, Y. J. Choi, C. J. Kang, D. Y. Jeon, D. C. Kim, S. Seo, and H. J. Chung. The interlayer screening effect of graphene sheets investigated by Kelvin probe force microscopy. *Appl. Phys. Lett.*, 95(22):222107, 2009. 60

[97] K. Choi, P. Lysaght, H. Alshareef, C. Huffman, H.-C. Wen, R. Harris, H. Luan, P.-Y. Hung, C. Sparks, M. Cruz, K. Matthews, P. Majhi, and B. H. Lee. Growth mechanism of TiN film on dielectric films and the effects on the work function. *Thin Solid Films*, 486(12):141 – 144, 2005. 61

[98] H. Hornauer, J. Vancea, G. Reiss, and H. Hoffmann. Thickness dependence of the work function in double-layer metallic films. *Z. Phys., B, Condens. Matter*, 77(3):399–407, 1989. 64

[99] I. Heller, S. Chatoor, J. Mnnik, M. A. G. Zevenbergen, C. Dekker, and S. G. Lemay. Comparing the weak and strong gate-coupling regimes for nanotube and graphene transistors. *Phys. Stat. Sol. (RRL)*, 3(6):190–192, 2009. 64

[100] P. Joshi, H. E. Romero, A. T. Neal, V. K. Toutam, and S. A. Tadigadapa. Intrinsic doping and gate hysteresis in graphene field effect devices fabricated on sio 2 substrates. *J. Phys.: Condens. Matter*, 22(33):334214, 2010. 65

[101] M. Liu, X. Yin, E. Ulin-Avila, B. Geng, T. Zentgraf, L. Ju, F. Wang, and X. Zhang. A graphene-based broadband optical modulator. *Nature*, 474(7349):64–67, 2011. 66, 70, 73

[102] M. Liu, X. Yin, and X. Zhang. Double-layer graphene optical modulator. *Nano Lett.*, 12(3):1482–1485, 2012. 66, 70, 73

[103] Q. Bao, H. Zhang, Z. Wang, B. Ni, C. H. Y. X. Lim, Y. Wang, D. Y. Tang, and K. P. Loh. Broadband graphene polarizer. *Nat. Photon.*, 5(7):411–415, 2011. 66

[104] B. Vasić, G. Isić, and R. Gajić. Localized surface plasmon resonances in graphene ribbon arrays for sensing of dielectric environment at infrared frequencies. *J. Appl. Phys.*, 113(1):013110, 2013. 66

[105] Z. Sun, T. Hasan, F. Torrisi, D. Popa, G. Privitera, F. Wang, F. Bonaccorso, D. M. Basko, and A. C. Ferrari. Graphene mode-locked ultrafast laser. *ACS Nano*, 4(2):803–810, 2010. 66

[106] U. Ralević, G. Isić, B. Vasić, and R. Gajić. Modulating light with graphene embedded into an optical waveguide. *J. Phys. D: Appl. Phys.*, 47(33):335101, 2014. 66

[107] U. Ralević, B. Isić, G.and Vasić, D. Gvozdić, and R. Gajić. Role of waveguide geometry in graphene-based electro-absorptive optical modulators. *J. Phys. D: Appl. Phys.*, 48(35):355102, 2015. 66

[108] G. Isić, R. Gajić, and S. Vuković. Plasmonic lifetimes and propagation lengths in metallodielectric superlattices. *Phys. Rev. B*, 89:165427, 2014. 68, 70

[109] G. T. Reed. *Silicon Photonics: The State of the Art*. Wiley-Interscience, New York, NY, USA, 2008. 71

[110] R. Hao, W. Du, H. Chen, X. Jin, L Yang, and E. Li. Ultra-compact optical modulator by graphene induced electro-refraction effect. *Appl. Phys. Lett.*, 103(6):061116, 2013. 73, 75

[111] H. T. Thompson, F. Barroso-Bujans, J. G. Herrero, R. Reifenberger, and A. Raman. Subsurface imaging of carbon nanotube networks in polymers with dc-biased multifrequency dynamic atomic force microscopy. *Nanotechnology*, 24(13):135701, 2013. 78

[112] B. Laban, V. Vodnik, and V Vasić. Spectrophotometric observations of thiacyanine dye J-aggregation on citrate capped silver nanoparticles. *Nanospectroscopy*, 1:5460, 2015. 79, 101, 102, 103, 112, 113

[113] Y. Sun and Y. Xia. Shape-controlled synthesis of gold and silver nanoparticles. *Science*, 298(5601):2176–2179, 2002. 79

[114] C. M. Cobley, S. E. Skrabalak, D. J. Campbell, and Y. Xia. Shape-controlled synthesis of silver nanoparticles for plasmonic and sensing applications. *Plasmonics*, 4(2):171–179, 2009. 79

[115] Y. Xia, X. Xia, and H.-C. Peng. Shape-controlled synthesis of colloidal metal nanocrystals: Thermodynamic versus kinetic products. *J. Am. Chem. Soc.*, 137(25):7947–7966, 2015. 79

[116] A. D. Rakić, A. B. Djurišić, J. M. Elazar, and M. L. Majewski. Optical properties of metallic films for vertical-cavity optoelectronic devices. *Appl. Opt.*, 37(22):5271–5283, 1998. 81, 104

[117] C. F. Bohren and D. R. Huffman. *Absorption and Scattering by an Arbitrary Particle*, pages 57–81. Wiley-VCH Verlag GmbH, 2007. 82, 104

[118] A. Castellanos-Gomez, N. Agrait, and G. Rubio-Bollinger. Optical identification of atomically thin dichalcogenide crystals. *Appl. Phys. Lett.*, 96(21), 2010. 82

[119] H. Li, J. Wu, X. Huang, G. Lu, J. Yang, X. Lu, Q. Xiong, and H. Zhang. Rapid and reliable thickness identification of two-dimensional nanosheets using optical microscopy. *ACS Nano*, 7(11):10344–10353, 2013. 82

[120] M. M. Benameur, B. Radisavljevic, J. S. Heron, S. Sahoo, H. Berger, and A. Kis. Visibility of dichalcogenide nanolayers. *Nanotechnology*, 22(12):125706, 2011. 84

[121] C. Lee, H. Yan, L. E. Brus, T. F. Heinz, J. Hone, and S. Ryu. Anomalous lattice vibrations of Single- and Few-layer MoS_2. *ACS Nano*, 4(5):2695–2700, 2010. 84, 86

[122] J. Kang, J.-W. T. Seo, D. Alducin, A. Ponce, M. J. Yacaman, and M. C. Hersam. Thickness sorting of two-dimensional transition metal dichalcogenides via copolymer-assisted density gradient ultracentrifugation. *Nat. Commun.*, 5:5478, 2014. 84

[123] C.J. Shearer, A.D. Slattery, A.J. Stapleton, J.G. Shapter, and C.T. Gibson. Accurate thickness measurement of graphene. *Nanotechnology*, 27(12):125704, 2016. 84

[124] X. Zhang, X.-F. Qiao, W. Shi, J.-B. Wu, D.-S. Jiang, and P.-H. Tan. Phonon and raman scattering of two-dimensional transition metal dichalcogenides from monolayer, multilayer to bulk material. *Chem. Soc. Rev.*, 44:2757–2785, 2015. 86

[125] A. Splendiani, L. Sun, Y. Zhang, T. Li, J. Kim, C.-Y. Chim, G. Galli, and F. Wang. Emerging photoluminescence in monolayer MoS_2. *Nano Lett.*, 10(4):1271–1275, 2010. 86, 87

[126] J. A. Schuller, S. Karaveli, T. Schiros, K. He, S. Yang, I. Kymissis, J. Shan, and R. Zia. Orientation of luminescent excitons in layered nanomaterials. *Nat. Nano.*, 8:271–276, 2013. 97

[127] G. M. Akselrod, T. Ming, C. Argyropoulos, T. B. Hoang, Y. Lin, X. Ling, D. R. Smith, J. Kong, and M. H. Mikkelsen. Leveraging nanocavity harmonics for control of optical processes in 2D semiconductors. *Nano Lett.*, 15(5):3578–3584, 2015. 99

[128] A. Manjavacas, F. J. Garca de Abajo, and P. Nordlander. Quantum plexcitonics: Strongly interacting plasmons and excitons. *Nano Lett.*, 11(6):2318–2323, 2011. 101

[129] N. T. Fofang, T.-H. Park, O. Neumann, N. A. Mirin, P. Nordlander, and N. J. Halas. Plexcitonic nanoparticles: Plasmon-exciton coupling in nanoshell-J–aggregate complexes. *Nano Lett.*, 8(10):3481–3487, 2008. 101

[130] E. Dulkeith, A. C. Morteani, T. Niedereichholz, T. A. Klar, J. Feldmann, S. A. Levi, F. C. J. M. van Veggel, D. N. Reinhoudt, M. Möller, and D. I. Gittins. Fluorescence quenching of dye molecules near gold nanoparticles: Radiative and nonradiative effects. *Phys. Rev. Lett.*, 89:203002–203006, 2002. 101

[131] J. Zhao, X. Zhang, Y. C. Ranjit, A. J. Haes, and R. P. Van Duyne. Localized surface plasmon resonance biosensors. *Nanomedicine*, 1:219–228, 2006. 101

[132] M. A. Noginov, G. Zhu, A. M. Belgrave, R. Bakker, V. M. Shalaev, E. E. Narimanov, S. Stout, E. Herz, T. Suteewong, and U. Wiesner. Demonstration of a spaser-based nanolaser. *Nature*, 460:1110–1112, 2009. 101

[133] N. G. Basts, J. Piella, and V. Puntes. Quantifying the sensitivity of multipolar (dipolar, quadrupolar, and octapolar) surface plasmon resonances in silver

nanoparticles: The effect of size, composition, and surface coating. *Langmuir*, 32(1):290–300, 2016. 102

[134] B. Laban, V. Vodnik, M. Dramićanin, M. Novaković, N. Bibić, S. P. Sovilj, and V. M. Vasić. Mechanism and kinetics of J-aggregation of thiacyanine dye in the presence of silver nanoparticles. *J. Phys. Chem. C*, 118(40):23393–23401, 2014. 103

[135] M. Kerker, D.-S. Wang, and H. Chew. Surface enhanced raman scattering (sers) by molecules adsorbed at spherical particles. *Appl. Opt.*, 19(19):3373–3388, Oct 1980. 104

[136] H. Yao, Y. Kagoshima, S. Kitamura, T. Isohashi, Y. Ozawa, and K. Kimura. Superstructures of mesoscopic monomolecular sheets of thiacyanine J aggregates in solution. *Langmuir*, 19(21):8882–8887, 2003. 105

[137] C. Tserkezis, R. W. Taylor, J. Beitner, R. Esteban, J. J. Baumberg, and J. Aizpurua. Optical response of metallic nanoparticle heteroaggregates with subnanometric gaps. *Part. Part. Syst. Char.*, 31(1):152–160, 2014. 107, 108

[138] R. Esteban, R. W. Taylor, J. J. Baumberg, and J. Aizpurua. How chain plasmons govern the optical response in strongly interacting self-assembled metallic clusters of nanoparticles. *Langmuir*, 28(24):8881–8890, 2012. 107, 108

[139] Y. Kitahama, Y. Tanaka, T. Itoh, M. Ishikawa, and Y. Ozaki. Identification of thiacyanine J–aggregates adsorbed on single silver nanoaggregates by surface–enhanced raman scattering and emission spectroscopy. *Bull. Chem. Soc. Jpn.*, 82(9):1126–1132, 2009. 109

[140] D. L. Akins. Theory of Raman scattering by aggregated molecules. *J. Phys. Chem.*, 90(8):1530–1534, 1986. 109

List of Publications

[1] Ralević U., Lazarević N., Baum A., Eiter H.-M., Hackl R., Giraldo-Gallo P., Fisher I. R., Petrovic C., Gajić R., Popović Z. V.: Charge density wave modulation and gap measurements in $CeTe_3$, *Phys. Rev. B*, Vol 94, No 16, 2016, pp. 165132-1-165132-9

[2] Ralević U., Isić G., Vasić B., Gvozdić D., Gajić R.: Role of waveguide geometry in graphene-based electro-absorptive optical modulators, *J. Phys. D: Appl. Phys.*, Vol 48, No 35, 2015, pp. 355102-1 - 355102-9

[3] Matković A., Chhikara M., Milićević M., Ralević U., Vasić B., Jovanović Dj., Belić M. R., Bratina G., Gajić R.: Influence of a gold substrate on the optical properties of graphene, *J. Appl. Phys.*, Vol 117, No 1, 2015, pp. 015305-1 - 015305-9

[4] Ralević U., Isić G., Vasić B., Gajić R.: Modulating light with graphene embedded into an optical waveguide, *J. Phys. D: Appl. Phys.*, Vol 47, No 33, 2014, pp. 335101-1 335101-9

[5] Beltaos A., Kovaević A. G., Matković A., Ralević U., Savić-Šević S., Jovanović Dj., Jelenković B. M., Gajić R.: Femtosecond laser induced periodic surface structures on multi-layer graphene, *J. Appl. Phys.*, Vol 116, No 20, 2014, pp. 204306-1 204306-6

[6] Vasić B., Kratzer M., Matković A., Nevosad A., Ralević U., Jovanović Dj., Ganser C., Teichert C., Gajić R.: Atomic force microscopy based manipulation of graphene using dynamic plowing lithography, *Nanotechnology*, Vol 24, No 1, 2013, pp. 015303-1 015303-9

[7] Matković A., Ralević U., Chhikara M., Jakovljević M. M., Jovanović Dj., Bratina G., Gajić R.: Influence of transfer residue on the optical properties of chemical vapor deposited graphene investigated through spectroscopic ellipsometry, *J. Appl. Phys.*, Vol 114, No 9, 2013, pp. 093505-1 093505-5

[8] Matković A., Beltaos A., Milićević M., Ralević U., Vasić B., Jovanovi Dj., Gajić R., Spectroscopic imaging ellipsometry and Fano resonance modeling of graphene,: *J. Appl. Phys.*, Vol 112, No 12, 2012, pp. 123523-1 123523-6

[9] Kilanski L., Górska M., Ślawska-Waniewska A., Lewińska S., Szymczak R., Dynowska E., Podgórni A., Dobrowolski W., Ralević U., Gajić R.: High temperature magnetic order in Zn1x Mn x SnSb2+MnSb nanocomposite ferromagnetic semiconductors *J. Phys. Condens. Matter*, Vol 28, No. 33, 2016, pp. 336004 -1-336004 -10

[10] Gilić M., Petrović M., Kostić R., Stojanović D., Barudija T., Mitrić M., Romčević N., Ralević U., Trajić J., Romčević M., Yahia I. S.: Structural and optical properties of CuSe2 nanocrystals formed in thin solid Cu-Se film, *Infrared Phys. Technol.*, Vol 76, No-, 2016, 276284

[11] Kratzer M., Klima S., Teichert C., Vasić B., Matković A., Ralević U., Gajić R.: Temperature dependent growth morphologies of parahexaphenyl on SiO2 supported exfoliated graphene, *J. Vac. Sci. Technol. B*, Vol 31, No 4, 2013, pp. 04D114-1 04D114-7

[12] Beltaos A., Kovaević A. G., Matković A., Ralević U., Jovanović Dj., Jelenković B., Gajić R.: Damage effects on multi-layer graphene from femtosecond laser interaction, *Phys. Scripta*, Vol 2014, No T162, 2014, pp. 014015-1 014015-5

[13] Stojanović D., Matković A., Aškrabić S., Beltaos A., Ralević U., Jovanović Dj., Bajuk-Bogdanović D., Holclajtner-Antunović I., Gajić R.: Raman spectroscopy of graphene: doping and mapping, *Phys. Scripta*, Vol 2013, No T157, 2013, pp. 014010-1 014010-4

[14] Matković A., Ralević U., Isić G., Jakovljević M. M., Vasić B., Milošević I., Marković D., Gajić R.: Spectroscopic ellipsometry and the Fano resonance modeling of graphene optical parameters, *Phys. Scripta*, Vol 2012, No T149, 2012, pp. 014069-1 014069-3

Biography

Uroš Ralević was born in Majdanpek on May 26th 1986. After finishing Gymnasium in Majdanpek in 2005, he enroled the School of Electrical Engineering, University of Belgrade. He received B.Sc. degree in electrical enginnering at the School of Electrical Engineering, module of Nanoelectronics, Optoelectronics and Laser Techniques, in 2009, with grade point average of 8,24. Next year, he received his M.Sc. degree at the same module, with grade point average of 10,00. He started his PhD studies at the School of Electrical Engineering, module of Nanoelectronics and Photonics, in 2010. Uroš Ralević has started his research at the Center for solid state physics and new materials, Institute of physics, University of Belgrade, within national research project No. OI171005. During his research career he has authored/coauthored 14 peer reviewed papers. Additionally, he has participated in 5 bilateral projects, 3 COST actions and an European FP7 project.

Изјава о ауторству

Име и презиме аутора Урош Ралевић

Број индекса 5007/2010

Изјављујем

да је докторска дисертација под насловом

Наноскопија и примене дводимензионалних и квази дводимензионалних система

- резултат сопственог истраживачког рада;
- да дисертација у целини ни у деловима није била предложена за стицање друге дипломе према студијским програмима других високошколских установа;
- да су резултати коректно наведени и
- да нисам кршио/ла ауторска права и користио/ла интелектуалну својину других лица.

Потпис аутора

У Београду, 02. 02. 2017

Изјава о истоветности штампане и електронске верзије докторског рада

Име и презиме аутора Урош Ралевић

Број индекса 5007/2010

Студијски програм Наноелектроника и фотоника

Наслов рада Наноскопија и примене дводимензионалних и квази дводимензионалних система

Ментор проф. др. Јелена Радовановић

Изјављујем да је штампана верзија мог докторског рада истоветна електронској верзији коју сам предао/ла ради похрањена у **Дигиталном репозиторијуму Универзитета у Београду.**

Дозвољавам да се објаве моји лични подаци везани за добијање академског назива доктора наука, као што су име и презиме, година и место рођења и датум одбране рада.

Ови лични подаци могу се објавити на мрежним страницама дигиталне библиотеке, у електронском каталогу и у публикацијама Универзитета у Београду.

Потпис аутора

У Београду, 02.02.2017.

Изјава о коришћењу

Овлашћујем Универзитетску библиотеку „Светозар Марковић“ да у Дигитални репозиторијум Универзитета у Београду унесе моју докторску дисертацију под насловом:

Наноскопија и примене дводимензионалних и квази дводимензионалних система

која је моје ауторско дело.

Дисертацију са свим прилозима предао/ла сам у електронском формату погодном за трајно архивирање.

Моју докторску дисертацију похрањену у Дигиталном репозиторијуму Универзитета у Београду и доступну у отвореном приступу могу да користе сви који поштују одредбе садржане у одабраном типу лиценце Креативне заједнице (Creative Commons) за коју сам се одлучио/ла.

1. Ауторство (CC BY)

2. Ауторство – некомерцијално (CC BY-NC)

3. Ауторство – некомерцијално – без прерада (CC BY-NC-ND)

4. Ауторство – некомерцијално – делити под истим условима (CC BY-NC-SA)

5. Ауторство – без прерада (CC BY-ND)

6. Ауторство – делити под истим условима (CC BY-SA)

(Молимо да заокружите само једну од шест понуђених лиценци.
Кратак опис лиценци је саставни део ове изјаве).

Потпис аутора

У Београду, 02.02.2017.

1. **Ауторство**. Дозвољавате умножавање, дистрибуцију и јавно саопштавање дела, и прераде, ако се наведе име аутора на начин одређен од стране аутора или даваоца лиценце, чак и у комерцијалне сврхе. Ово је најслободнија од свих лиценци.

2. **Ауторство – некомерцијално**. Дозвољавате умножавање, дистрибуцију и јавно саопштавање дела, и прераде, ако се наведе име аутора на начин одређен од стране аутора или даваоца лиценце. Ова лиценца не дозвољава комерцијалну употребу дела.

3. **Ауторство – некомерцијално – без прерада**. Дозвољавате умножавање, дистрибуцију и јавно саопштавање дела, без промена, преобликовања или употребе дела у свом делу, ако се наведе име аутора на начин одређен од стране аутора или даваоца лиценце. Ова лиценца не дозвољава комерцијалну употребу дела. У односу на све остале лиценце, овом лиценцом се ограничава највећи обим права коришћења дела.

4. **Ауторство – некомерцијално – делити под истим условима**. Дозвољавате умножавање, дистрибуцију и јавно саопштавање дела, и прераде, ако се наведе име аутора на начин одређен од стране аутора или даваоца лиценце и ако се прерада дистрибуира под истом или сличном лиценцом. Ова лиценца не дозвољава комерцијалну употребу дела и прерада.

5. **Ауторство – без прерада**. Дозвољавате умножавање, дистрибуцију и јавно саопштавање дела, без промена, преобликовања или употребе дела у свом делу, ако се наведе име аутора на начин одређен од стране аутора или даваоца лиценце. Ова лиценца дозвољава комерцијалну употребу дела.

6. **Ауторство – делити под истим условима**. Дозвољавате умножавање, дистрибуцију и јавно саопштавање дела, и прераде, ако се наведе име аутора на начин одређен од стране аутора или даваоца лиценце и ако се прерада дистрибуира под истом или сличном лиценцом. Ова лиценца дозвољава комерцијалну употребу дела и прерада. Слична је софтверским лиценцама, односно лиценцама отвореног кода.